EXPERIMENTAL INVESTIGATION OF THE EFFECT OF INITIAL CONDITIONS ON RAYLEIGH-TAYLOR INSTABILITY

A Thesis

by

SARAT CHANDRA KUCHIBHATLA

Submitted to the Office of Graduate Studies of
Texas A&M University
in partial fulfillment of the requirements for the degree of

MASTER OF SCIENCE

August 2010

Major Subject: Mechanical Engineering

Experimental Investigation of the Effect of Initial Conditions on

Rayleigh-Taylor Instability

EXPERIMENTAL INVESTIGATION OF THE EFFECT OF INITIAL CONDITIONS ON RAYLEIGH-TAYLOR INSTABILITY

A Thesis

by

SARAT CHANDRA KUCHIBHATLA

Submitted to the Office of Graduate Studies of
Texas A&M University
in partial fulfillment of the requirements for the degree of

MASTER OF SCIENCE

Approved by:

Chair of Committee, Devesh Ranjan
Committee Members, Karen Vierow
Bing Guo
Head of Department, Dennis O'Neal

August 2010

Major Subject: Mechanical Engineering

ABSTRACT

Experimental Investigation of the Effect of Initial Conditions on

Rayleigh-Taylor Instability. (August 2010)

Sarat chandra Kuchibhatla, B.Tech., IIT Guwahati, India

Chair of Advisory Committee: Dr. Devesh Ranjan

An experimental study of the effect of initial conditions on the development of Rayleigh Taylor Instabilities (RTI) at low Atwood numbers (order of 10^{-4}) was performed in the water channel facility at TAMU. Initial conditions of the flow were generated using a controllable, highly reliable Servo motor. The uniqueness of the study is the system's capability of generating the required initial conditions precisely as compared to the previous endeavors. Backlit photography was used for imaging and ensemble averaging of the images was performed to study mixing width characteristics in different regimes of evolution of Rayleigh-Taylor Instability (RTI). High-speed imaging of the flows was performed to provide insights into the growth of bubble and spikes in the linear and non-linear regime of instability development.

RTI are observed in astrophysics, geophysics and in many instances in nature. The vital role of RTI in the feasibility and efficiency of the Inertial Confinement Fusion (ICF) experiment warrants a comprehensive study of the effect of mixing characteristics of RTI and its dependence on defining parameters. With this broader objective in perspective, the objectives of this present investigation were mainly threefold: First was the validation of the novel setup of the Water channel system. Towards this objective,

validation of Servo motor, splitter plate thickness effects, density and temperature measurements and single-mode experiments were performed. The second objective was to study the mixing and growth characteristics of binary and multi-mode initial perturbations seeking an explanation of behavior of the resultant flow structures by performing the first ever set of such highly controlled experiments. The first-ever set of experiments with highly controlled multi-mode initial conditions was performed. The final objective of this study was to measure and compare the bubble and spike velocities with single-mode initial conditions with existing analytical models. The data derived from these experiments would qualitatively and quantitatively enhance the understanding of dependence of mixing width on parametric initial conditions. The knowledge would contribute towards a generalized theory for RTI mixing with specified dependence on various parameters, which has a wide range of applications.

The system setup was validated to provide a reliable platform for the novel multi-modal experiments to be performed in the future. It was observed that the ensemble averaged mixing width of the binary system does not vary significantly with the phase-difference between the modes of a binary mode initial condition experiment, whereas it varies with the amplitudes of the component modes. In the exponential and non-linear regimes of evolution, growth rates of multi-mode perturbations were found to be higher than the component modes, whereas saturation growth rates correspond to the dominant wavelength. Quadratic saturation growth rate constants, α were found to be about 0.07 ± 0.01 for binary and multi modes whereas single-mode data measured α about 0.06 ± 0.01. High-speed imaging was performed to measure bubble and spike amplitudes to

obtain velocities and growth rates. It was concluded that higher temporal and spatial resolution was required for accurate measurement. The knowledge gained from the above study will facilitate a better understanding of the physics underlying Rayleigh-Taylor instability. The results of this study will also help validating numerical models for simulation of this instability, thereby providing predictive capability for more complex configurations.

DEDICATION

To my family

ACKNOWLEDGEMENTS

First and foremost, I would like to thank my family for their encouragement and constant support through all these years away from home. I would also like to thank my research advisor, Dr. Ranjan, for his guidance during the past one and half years. I am glad to be his first student to graduate, and I wish him great success in the years to come. My gratitude goes to Dr. Andrews for his advice during the course of the project, especially at the initial stages and also for the resources provided for performing these studies. I also thank the Department of Mechanical Engineering of TAMU for hiring me as a Teaching Assistant (TA) during the year 2009. It was an immense learning experience to work as a TA for two graduate level courses. A special mention of thanks to Dr. Duggleby and Yuval Doron who also helped me with setting up and running experiments in the earlier stages of the project. The *Matlab* code used for image analysis was modified to a large extent by them.

I am grateful to my thesis committee members, Dr. Karen Vierow and Dr. Bing Guo, for their valuable input on improving the thesis. Last but not the least, I thank Adam, Bhanesh, Jacob, Peter Kyle, Srini and Thomas for so many rides to the Riverside lab, and for other help in performing experiments, without which I could not have completed this assignment. The discussions I had with Bhanesh and Jacob were very useful and improved my understanding of the subject. The interactions I had with the STL group were fun and enriched my overall experience here at TAMU. This research was funded by the LANL grant # LDRD-DR20090058DR.

NOMENCLATURE

RTI	Rayleigh-Taylor Instability
KHI	Kelvin-Helmholtz Instability
ICF	Inertial Confinement Fusion
α	Saturation growth constant
RMI	Richtmyer Meshkov Instability
KHI	Kelvin-Helmholtz Instability
P	Local fluid pressure
ρ	Local fluid density
$\boldsymbol{U}$	Velocity vector
$\boldsymbol{\omega}$	Vorticity vector
v	Kinematic viscosity
LST	Linear Stability Theory
η_m	Dominant mode growth rate
g	Acceleration due to gravity
ρ_1	Density of heavier fluid
ρ_2	Density of lighter fluid
l_m	Dominant wavelength
h_{nl}	Height of perturbation (in non-linear regime)
$\underline{\lambda}$	Wavelength of perturbation

v_∞	Terminal velocity of bubble or spike
C_∞	Proportionality constant for terminal velocity
R_b	Bubble radius
At	Atwood number
t	Time
ΔT	Temperature difference
h_h	Mixing layer half-width
h_b	Height of bubble
h_s	Height of spike
f	Normalized density gradient (or mixture fraction)
DNS	Direct Numerical Simulation
τ	Non-dimensionalized time
PLIF	Planar Laser Induced Fluorescence
PIV	Particle Induced Velocimetry
σ	Grid solidity ratio
d_g	Width of grid member
M	Spacing between members of a square grid
1D	One-dimensional
2D	Two-dimensional
3D	Three-dimensional
η	Bubble or spike growth rate
ζ	Bubble curvature

Fr	Parameter dependent on bubble shape and fluid environment
Fi	Froude number
U_a	Velocity of bubble or spike
N	Characteristic buoyancy frequency
d	Diameter of bubble or spike
k	Wavenumber
k_p	Peak/ dominant wavenumber
ζ_p	Peak/ dominant bubble curvature
λ_p	Peak wavelength
t_0	Onset-time of scale invariant regime
u_0	Average initial velocity
LEM	Linear Electric Motor
T	Temperature
ρ_h	Density of hot fluid
ρ_c	Density of cold fluid
x, y,z	Streamwise, crosswise and spanwise coordinates
u,v,w	Streamwise, crosswise and spanwise velocity components
U_∞	Free-stream velocity
Re	Reynolds number
I_0	Intensity of incident light
I	Transmitted intensity
ε	Molar absorptivity

c	Concentration of the species
L	Length of flapper
A	Amplitude of flapper tip
H	Total height of the water channel
θ	Phase-difference (angle)
ω	Angular frequency
T_p	Time-period
h	Total mixing-width

TABLE OF CONTENTS

Page

Page

Page

LIST OF FIGURES

FIGURE Page

FIGURE Page

FIGURE Page

LIST OF TABLES

1.INTRODUCTION

1.1. Motivation

The numerical and experimental study of Rayleigh-Taylor Instabilities (RTI) is essential for understanding the physics of fluid mixing in natural phenomenon like fluid mixing in river beds, in astrophysics and geophysics. Rayleigh-Taylor Instability is one of the fundamental mechanisms for mixing. As Andrews and Dalziel (2010) have explained (paraphrasing): RTI plays an important role in the mixing that results from other natural mixing processes where density surfaces are overturned, e.g. Kelvin-Helmholtz Instability (KHI) and breaking gravity waves. Indeed, not only is the mixing efficiency of RTI higher than that of any other known mechanism, but it has been suggested as an explanation for the much lower mixing efficiencies due to shear or mechanical agitation. These flows are characterized by buoyancy, viscosity and diffusion effects, and exhibit a large range of length and time scales. Therefore, experimental investigation of such flows must be conducted in order to provide comprehensive information for understanding their behavior. The knowledge gained from these experiments will lead us into developing better methodologies for applications like Inertial Confinement Fusion (ICF), spray combustion in engines etc. The significance of RTI in the feasibility and productivity of the ICF experiment (Lindl & Mead 1975; Lindl 1999) warrants a detailed investigation of the underlying physics of RTI. Scientific outcomes of the studies will have a direct impact on the energy efficiency

---

This thesis follows the style of *Journal of Fluid Mechanics*.

of the ICF, which could be employed as a standard process of power generation in the future. Inertial confinement fusion at the Lawrence Livermore National Laboratories is attempted using the ablation of a micrometer scale Deuterium-Tritium (DT) fuel spherical pellet encased in a Beryllium capsule. Implosion of the capsule using high-energy LASERs deposits a large amount of energy on the resulting plasma, producing shock-waves of high strength. These shock waves act upon the surface imperfections of the capsule resulting in Richtmyer-Meshkov Instability (RMI). Thus, at the initial stages of the fusion process, RMI due to impulsive acceleration dominates the flow physics. It was shown using simulations (Schmitt *et al.* 2001) that the acceleration profiles of the plasma reach sustenance, and Rayleigh-Taylor instability dictates flow physics henceforth. RM and RT induced mixing of the Beryllium capsule with the DT fuel results in degradation of fuel quality and affect the yield of the experiment. Thus, RTI has a significant role in feasibility and power yield of the experiment, thus warranting an in-depth analysis of the instability. Of special interest is the effect of initial condition on the evolution of RTI and resultant mixing behavior. Although RTI in the ICF experiment is characterized by small time and length scales, high temperatures and high density gradients (Atwood number, At), the effect of initial conditions must be studied carefully such that mixing of the fuel with other materials in the ICF experiment can be optimized. Here At is the Atwood number defined by

Equation 1: $$At = \frac{(\rho_1 - \rho_2)}{(\rho_1 + \rho_2)}$$

Shown in Figure 1 is a 2D schematic of the National Ignition Facility (NIF) scale ignition double shell using HYDRA simulation. A pie-shaped cross section of the area of

interest is depicted, certain duration after pellet is impinged upon by LASERs. Details of this simulation can be found in (Robey 2008). The schematic shows various material interfaces between the outer Beryllium (Be) capsule and the inner DT fuel, and the resulting finger-shaped structures characteristics of RT instabilities.

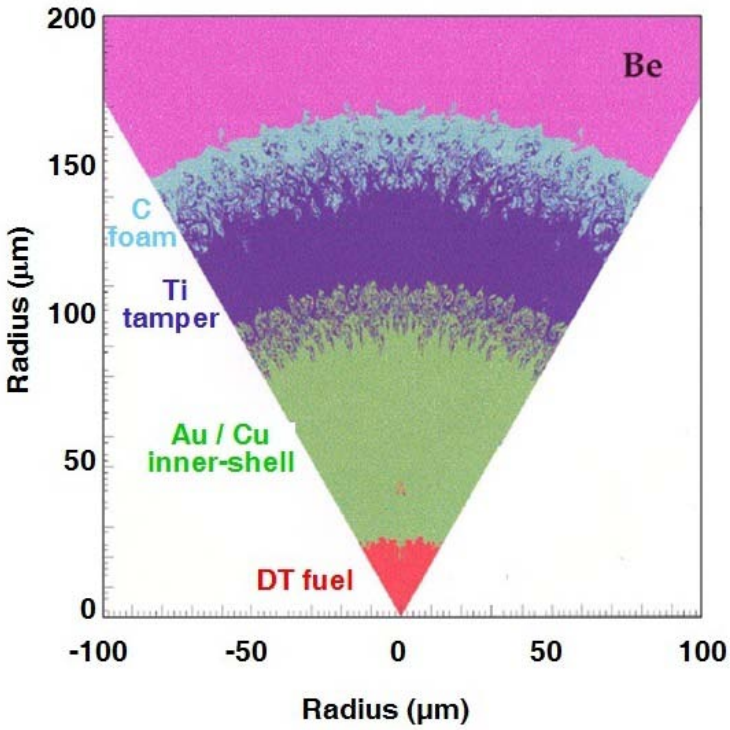

Figure 1: 2D cross section of the beryllium encased DT fuel pellet.

Motivated by the significance of RTI in the ICF application, studies are being performed to study RTI in detail so as to consolidate the scientific community's understanding and develop a generalized theory that explains and quantifies the

underlying physical phenomenon. Earlier theory by Youngs (1984), and experiments (Snider & Andrews 1994; Dimonte & Schneider 2000; Waddell, Niederhaus & Jacobs 2001; Huang *et al.* 2007) establish a self-similar behavior of the fluid at late-times of the evolution of a Rayleigh-Taylor interface. Recent studies by Dimonte (2004), Olson & Jacobs (2009) and Ramaprabhu, Dimonte and Andrews (2005) have suggested that the memory of initial condition persists in the flow even at late times. This thesis aims at experimentally investigating the effects of initial conditions on the development of RTI in a two-fluid scenario using the water channel facility at TAMU.

1.2. Theoretical background

This section gives a working background of RTI. Rayleigh-Taylor Instability (RTI) occurs when a heavier fluid is placed over a lighter fluid. This acceleration could be due driven by gravity, but if the acceleration is impulsive and external such as due to shocks, it is called Richtmyer-Meshkov instability (RMI). If the fluids acceleration is caused by applied shear, such instability is called Kelvin-Helmholtz instability. In RTI, at a fluid interface with a density gradient, vorticity is deposited due to (misalignment of the density and pressure gradients ($\nabla P . \nabla \rho < 0$) where P is the local pressure and ρ is the density of the fluid (Chandrasekhar 1961). This can be witnessed in the vorticity Equation 2 given below, where vorticity generation due to density stratification can be treated as a source term on the right hand side. Here, $\boldsymbol{U}$ is the velocity vector and $\boldsymbol{\omega}$ is the vorticity vector.

Equation 2: $$\frac{D\omega}{Dt} = \vartheta \nabla^2 \omega + \omega . \nabla U - \nabla \times \left(\frac{\nabla P}{\rho}\right)$$

This additional term $-\nabla \times \left(\frac{\nabla P}{\rho}\right) = \nabla P \times \frac{\nabla \rho}{\rho^2}$ is called the Baroclinic vorticity term and is non-zero for a density stratified fluid configuration. At time *t*=0, as viscous effects are negligible, this term drives the velocity field. Figure 2 demonstrates Baroclinic vorticity generation due to misalignment of the Pressure and density gradients. The image was taken from Doron (2009).

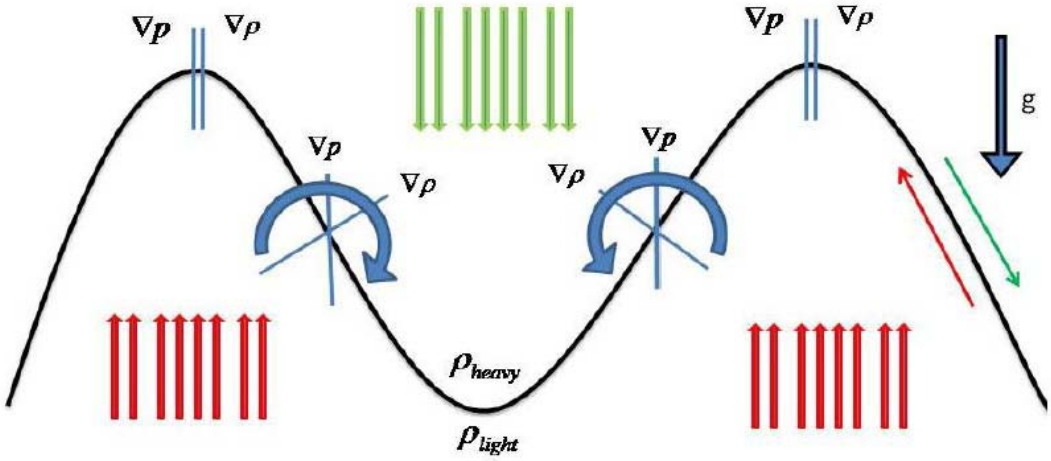

Figure 2: Baroclinic vorticity deposition at a two-fluid interface.

The schematic shows a sinusoidal interface with heavy fluid at the supported by the lighter fluid. Baroclinic vorticity deposition due to this density gradient at the interface is also shown.

Any infinitesimally small perturbation at the interface at the interface starts to grow under the acceleration due to gravity. Perturbations are classified based on the number of modes involved, which are basically the number of wavelengths that compose the perturbation, and the phase-difference between the modes. At larger wave numbers, microscopic processes such as molecular diffusion and viscosity become significant in

the system. Thus, a range of length scales and time-scales define the initial conditions of RTI, and a theory is sought to explain the resultant instability for the range of initial conditions. Each perturbation that is input at the interface at time t=0 initially grows exponentially according to Linear Stability Analysis (LST) (Chandrasekhar 1961) and eventually the growth rate of the perturbation saturates to a terminal velocity. An extensive analysis of various phases of perturbation growth was given by Youngs in 1984. The perturbation evolves through four different phases by Youngs (1984), namely (1) Exponential regime, where the instability grows exponentially in time, where Linear stability analysis is valid (2) Linear regime, where the acceleration of the interface slows down to a constant, and (3) Mode coupling or bubble competition, where the adjacent structures compete for evolving dominant wavelengths. In the linear regime, assuming negligible viscous forces, growth rate of the most dominant mode is given by Chandrasekhar as:

Equation 3: $$n_m = \left\{\frac{\pi g}{l_m}\frac{(\rho_1-\rho_2)}{(\rho_1+\rho_2)}\right\}$$

Transition to the non-linear regime is taken to be when the linear velocity of a bubble or spike equals the saturation/ terminal velocity of the structure. This is when the height of the structure h_{nl} equals the wavelength of the perturbation, λ. As the dominant mode evolves into the non-linear regime, terminal velocity for a dominant wavelength is given by Daly (1967):

Equation 4: $$v_\infty \propto C_\infty \sqrt{\frac{(\rho_1-\rho_2)}{\rho_1} g R_b}$$

where R_b is the bubble radius and C_∞ is a constant. Bubbles are defined as the typical cylindrical interfacial projections of the lighter fluid into heavier fluid, while spikes are projections of the heavier fluid into the lighter fluid. These bubbles and spikes have characteristic mushroom shapes with rounded tips. At low Atwood numbers, bubble and spike growth are symmetric, with C_∞ to be ~0.7. Thus, Atwood number is of the order of 10^{-4} for the water channel experiments at TAMU using cold and hot water with a temperature difference, ΔT of about 5°C. After the non-linear regime, due to mode coupling, the wavelengths eventually saturate and a self-similar behavior of the mixing-layer is observed, i.e. the mixing is described by a similarity solution as given in Equation 5. Mode coupling is defined as the non-linear interaction of component modes so that resultant dominant modes are produced. At this stage, since the memory of initial conditions is lost, a quadratic growth of the mixing layer half width, h_h was proposed by Youngs based on dimensional analysis as given:

Equation 5: $$h_h = \alpha . At . g . t^2$$

Here α is the quadratic/ saturation growth rate constant, At is the Atwood number, g is the acceleration due to gravity and t is time. Based on many numerical and experimental studies (Snider & Andrews 1994; Dimonte & Schneider 2000; Waddell, Niederhaus & Jacobs 2001; Huang *et al.* 2007) researchers have come up with different values of α, within a generally accepted range of 0.07 to 0.01. Details of the different values of α obtained by various studies are given in the literature review section §1.3. The mixing half-width h_h is defined as

Equation 6: $$h_h = \left(\frac{h_b - h_s}{2}\right)$$

where h_b is defined as height of the bubble specified at each location where

Equation 7: $$f = \frac{(\rho - \rho_2)}{(\rho_1 - \rho_2)} = 0$$

and h_s is defined as the height of the spike given by f = 0.05. In the later stage, viscosity becomes predominant and the flow is turbulent at late-times. Various stages of the interface are shown in Figure 3 displaying mushroom shaped 'bubble' and 'spike' structures characteristic of RTI flows. Secondary structures arising because of KHI, which is a secondary phenomenon, can also be observed.

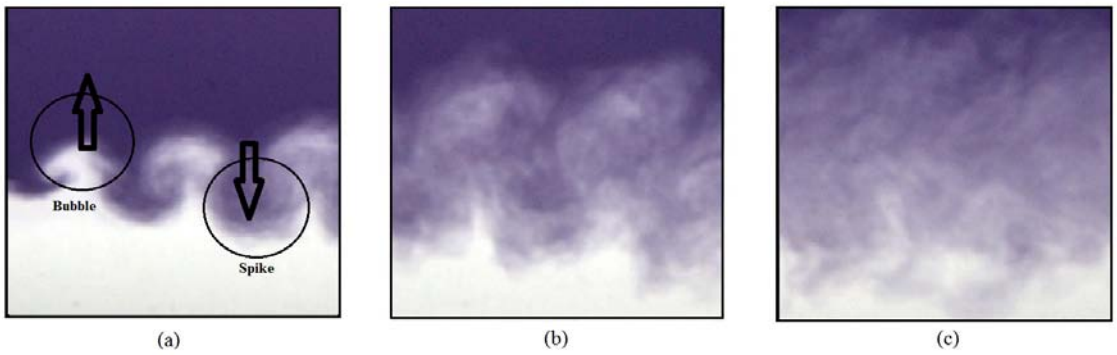

Figure 3: Regimes of RTI: (a) Exponential (b) Saturation and (c) Turbulent.

These images of RTI with single-mode initial conditions were captured at the Water channel facility of TAMU.

The effect of initial condition and memory effect on the above described stages of evolution of RTI is widely debated in the literature. Most experiments studied the effect of single-mode initial perturbations at the interface imposed on the flow. It was observed that at the initial stages, the instability is characterized by the imposed single wavelengths, which then interact with each other because of mode-coupling and newer,

dominant wavelengths emerge, which evolve to a larger range of wavelengths as the flow becomes turbulent. Also debated is the nature of the growth constant in the self-similar regime, α which various theories, experiments and simulations have reported differently. It was observed that values of α obtained from experiments were smaller than that calculated from numerical simulations. These differences were attributed to the difficulties in properly quantifying the experimental initial condition. Few researches have even contended the existence of one universal α for all initial conditions on the basis that it is solely based on dimensional-analysis Doron (2009).

1.3. Literature review

This section provides the literature review of the research previously performed at TAMU and various other facilities around the world. Since a large number of experiments were performed at TAMU over the past years, the next section §1.3.1 details those experiments using the water channel to give a complete overview of the past, present and future of research using the facility with an additional discussion of the errors in the experiments. This is essential as it is suggested to construct a new water channel with better capabilities in the section §4.4 and Section §1.3.2 details the relevant research work performed at all other locations.

1.3.1. Literature review of TAMU water channel experiments

Studies of Rayleigh-Taylor instabilities have been performed since 1960. To recount all the previous experiments on this topic and exclusively list all the attempts is beyond the scope of this thesis. However, a list of significant experimental studies is listed here. This present section describes the previous studies performed at TAMU

water channel facility and the observations corresponding to the present thesis. This will provide an estimate of the improvements of the present thesis over the previous studies, and provide a basis for comparison. One of the main advantages of performing experiments using the water channel is the large collection time, and the statistically steady nature of the flow. The size of the facility is also comparatively larger than many RTI facilities. This means that there is sufficient spatial and temporal resolution so that statistical data analysis can be performed. The drawback is that larger flow rates are required, which means that higher temperature gradients and therefore, higher Atwood numbers are difficult to achieve.

Leicht (1997) has observed the effect of binary-mode initial conditions on RTI by studying ensemble averaged mixing characteristics. The binary initial conditions were generated using two variable speed electrical motors which were coupled eccentrically to produce the required phase-shift between the modes. Varying the speed of the motor produces required wavelengths, and changing the eccentricity produced the desired phase-shift. The difficulty with this setup was that the phase-shift was found to vary during an experiment, which is rectified in the present work because of the usage of a highly-controllable servo motor. Therefore, a set of experiments similar to Leicht (1997) have been chosen for comparison, which is presented in section §3.1. Mueschke (2004) experimentally measured the initial density and velocity perturbations at the two-fluid interface and parametrized those for numerical simulations using Direct Numerical Simulation (DNS) approach. They have observed that the splitter plate and the edge mesh combination introduced larger wave numbers into the flow as compared to smaller

initial wave numbers at the interface. Span wise velocity fluctuations at the interface were found to be negligible. Molecular mixing fraction was measured at the center plane and it was found to decrease corresponding to τ = 0.3, smaller compared to earlier findings. τ is defined as the non-dimensionalized time given by

Equation 8: $$\tau = t\sqrt{\left(\frac{At.g}{h}\right)}$$

Kraft (2004) has studied the effect of a buoyant wake off a cylinder placed aligned with the centerline of the water channel. Planar Laser Induced Fluorescence (PLIF) and Particle Image Velocimetry (PIV) were employed to measured density and velocity fluctuations at various locations to study wake interaction with buoyancy driven mixing layer. A mathematical model to describe the decay of vertical velocity fluctuations in the wake region of the RTI was also formulated. Peart (2008) has performed experiments to study the effect of grid generated initial conditions on RTI in the water channel facility. Fine, medium and coarse grids with high solidity ratio were chosen and it was observed that the self-similar growth constant α decreased with increasing grid size. Grid Solidity ratio σ is defined as

Equation 9: $$\sigma = \frac{d_g}{M}\left(2 - \frac{d_g}{M}\right)$$

where d_g is the width of each grid member and M is the spacing between adjacent members of a square grid. PIV was used to measure statistical velocity data and the same initial conditions from experiment were input into a numerical model that uses the Besnard, Harlow, Rauenzahn (BHR) model of turbulent transport. The experiments and numerical simulations were found to be in good agreement in the self-similar region of the flow.

1.3.2. Literature review of other studies

As listed in the previous section, §1.3, this section provides the review of the research previously performed at various other facilities around the world. The following survey explains the analytical, numerical and experimental advancements and their outcomes such that it serves to provide a basis for the understanding of RTI and comparison of the present mixing width characteristics and bubble and spike behavior with literature.

1.3.2.1. Analytical theories

This section deals with the chronological survey of analytical theories on RTI. Historically, RTI growth due to gravity was first studied by Lord Rayleigh (1883), and RTI due to other acceleration was studied by Taylor (1950). Taylor proposed a linear theory for the equation of the interface of two-fluids acted upon by acceleration in a direction perpendicular to the interface. This is called the Linear Stability theory (LST). Based on the experiments conducted by Taylor in Part II of his work (Lewis 1950), the linear stability theory is deemed valid until the amplitude of the modes reaches 0.4 times the wavelength of the mode. The experiments were conducted for a wide variety of density ratios and varying accelerations of the fluid interfaces. Taylor also observed a terminal velocity proportional to the difference in acceleration of the fluid interface and the acceleration due to gravity. However, much of the analysis assumes a potential flow condition, neglecting the effects of vorticity and viscosity in the earlier times.

Since the seminal papers of Lord Rayleigh and Taylor, many theories have been proposed to lay a foundation for understanding of RTI. Analytical theories were the

beginning point of RTI studies and have provided an idealized simplified understanding of the problem and pointed the shortcomings that need to be further investigated. Layzer's work (1955a) proposed a theory for shape of the fluid interface using a 2D, inviscid, incompressible analytical model. He formulated a stream function for fluid flow within a cylindrical tube due to a sudden removal of an initially perturbed diaphragm at zero-time. The fluid velocity at the tip of the diaphragm was calculated and a stream function was formulated corresponding to this velocity. This velocity was found to saturate as a function of radius of the cylinder. Effect of the wall on the flow on a periodic array of cylinders is then calculated and the solution was still found to be valid. He therefore surmised that the shape of a typical fluid interface in RTI can be considered as an array of cylinders, and that viscosity and surface tension stabilize the interface. He had also observed that the interfaces with initially larger amplitudes grow faster but the interfaces with initially smaller amplitudes last longer. As periodic flows do not exist in practice, the number of bubbles will continually diminish and only the largest wavelengths remain. However, this approach assumed a stream function formulation and a cylindrical shape for the bubbles and spikes, which is found to have a large deviation from the mushroom shaped bubbles and spikes in reality.

Goncharov (2002) proposed an analytical model for RTI for bubble and spike velocities for the different regimes by using a velocity potential formulation. This model provided a continuous bubble evolution theory from linear to non-linear regime whereas the Buoyancy-drag models calculated only asymptotic behavior. An idealized analytical model proposed by Mikaelian (2003) predicted bubble amplitudes for arbitrary Atwood

numbers by improving upon Layzer's work (1955a). Growth rate in the non-linear regime was analytically integrated using 2D and 3D approaches and a linear variation of growth rate η (defined as time rate of change of bubble or spike amplitude, $\frac{dy}{dt}$) was reported in the linear regime and an asymptotic growth rate reported for large times. This model was in some agreement with Fermi's (Layzer 1955b), Oron *et al.*'s (2001) and Goncharov's (2002) models. Abarzhi et al. (2003) proposed multiple harmonic non-linear theoretical solutions to account for vorticity generation and secondary instabilities (e.g. KHI). They observed that for smaller initial perturbations, most of the energy is contained in large scale structures and vice-versa by correlating bubble curvature ζ (defined as $\frac{d^2y}{dt^2}$) to Atwood number. Their solution matched well with asymptotic bubble curvatures by Alon *et al.* (1995) and Layzer (1955a). For low Atwood number, bubble curvature flattens out, and saturated bubble and spike velocities are reduced. This theory placed importance on bubble curvature and experimental data might corroborate their conclusions.

Another analytical theory by Dimonte (2004) proposed a general theory for bubble and spike growth for all Atwood number as dependant on a parameter [Fr (defined as $\sqrt{Froude\#}$), where Froude# is defined as $Fi = U_a/Nd$ where U_a is the velocity of bubble or spike, N is the characteristic buoyancy frequency and d is the diameter of bubble or spike] which depends on the shape of the bubble and its environment. Non-linear mode coupling of modes was found to have non-significant effect on broadband initial perturbations. Wavenumbers $k>k_p$ (k_p is the peak wave number corresponding to peak growth rate ζ_p) dominate eventually, and growth rate was

found to vary as $\sqrt{(At.g.k)}$. Terminal velocity calculations were found to be a dependent on Atwood number, whereas theories by Sohn (2003; 2009) proposed them to be independent of Atwood number. This is because Atwood number affects the shape of the mushrooms, which in turn affect *Fr*. Also larger wave numbers were found to grow faster than smaller wave numbers whereas larger wave numbers saturate faster. Modes closest to the peak/dominant wave number grow fastest. Saturation velocities were also computed by setting the growth rates to zero.

1.3.2.2. Numerical simulations

To account for the shortcomings of analytical theories and improve the predictive capability, numerical simulations were extensively performed and benchmarked with experimental data. Two major theories have been proposed to explain observed bubble and spike interactions, namely Competition models and Buoyancy-Drag models. Whereas competition models or merger models attribute adjacent bubble and spike interactions to explain growth, drag-buoyancy models predict growth rates based on the resultant drag on the mushroom shaped structures at different regimes of flow development. Some of the major simulations concerning initial conditions and their effects on RTI behavior follow based on complexity of the simulation, i.e. simpler models are listed before comprehensive studies.

Freed et al. (1991) have conducted numerical simulations of RTI in the self-similar turbulent regime by taking the 1D incompressible, two-phase model of Youngs (1984) as a starting point and modifying to an Arbitrarily Lagrangian Eulerian (ALE) code. Multi-wavelength, small amplitude, random noise is applied as initial perturbation

and the interface was explicitly tracked. The authors observed a non-dimensional combination of scales and density ratio resulting in a self-similar behavior of the fluid at late-times. Bubble growth rate was found to follow $\alpha g t^2$ whereas considerable numerical noise was observed at the spike tips.

Alon et al. (1995) performed 2D numerical simulations of multi-mode RTI by modifying Layzer's theory and accounted for bubble and spike growth rates as self-similar. Power laws for different Atwood number were formulated for single-mode cosine initial perturbations imposed on an incompressible flow hypothesis. They propose that the spike velocity is reduced because of the formation of a rounded-head, which reduces its drag and bubbles grow faster because of a smaller area to volume ratio, i.e. smaller drag. They have also performed simulations with binary-mode initial conditions and report the following:

For $t < t_0$, the two bubbles rise independently.

For $t > t_0$, larger bubbles expand faster and smaller bubbles are swept in their wake.

For $t >> t_0$, an asymptotically periodic array of bubbles and spikes of $2\lambda_p$ remains.

Here, λ_p is the dominant wavelength; t_0 is the onset-time of scale invariant regime, defined by

Equation 10:
$$t_0 = \frac{n\lambda_p}{u_0}$$

and u_0 is the average initial velocity and n depends on the initial condition. This bubble competition takes a longer time for smaller λ_p as compared to larger λ_p. The dependence

of bubble and spike height at late times on the wavelength of the initial perturbations for all Atwood numbers is noteworthy.

Abarzhi et al. (2003) have studied the dimensional dependence of RTI and RMI on late-time scaling laws in their numerical 2D and 3D simulations using a Buoyancy–drag model. They imposed a multi-mode initial condition with about 300 bubbles and improved upon the previous work by Alon et al. (1995). The dominant wavelength λ_p is defined differently as the length of a sample box cross-section divided by the number of bubbles present inside the box. Their 3D model predicts increased drag-rates (rate of drag force on the structure) and merger-rates (rate of merger of the structures) and reduced growth-rate constants, α. Bubble velocity depends on the dominant bubble size and spike velocity is dependent on bubble-motion. It was observed that bubbles reach saturation quicker compared to spikes.

1.3.2.3. Experiments

Fewer experiments campaigns were performed in the past to study the effect of initial conditions on RTI. Dimonte and Schneider (2000) used their Linear Electric Motor (LEM) facility (Dimonte *et al.* 1996) to perform these experiments over a wide combination of Atwood numbers and acceleration profiles. The experiments employed natural initial perturbations at the interface corresponding to the range 0.1-1mm and the meniscus of the fluid-solid interaction at enclosure walls served as a source of initial perturbation for some of the experiments. The projectile, which is basically the fluid container that slides along magnetic rails, is controllably accelerated to generate RTI. Observed acceleration profiles had an earlier steep rise and a plateau which are about

90% accurate. Bubble and spike displacements as a function of density ratio of the fluids and self-similar growth rate constants, α were reported. Average diameters at the mixing front location were also reported.

Huang et al. (Carlès *et al.* 2006; Huang *et al.* 2007) have studied magnetic levitated RTI with specific initial conditions using two immiscible fluids in a Hele-shaw cell and developed a theoretical model for the same. Here, the fluid- interface is stabilized until $t=0$ and the magnetic field is suddenly removed, so that density stratification results in RTI. The novelty of their experimental setup is the stabilization of the unstable two-fluid interface in required single-mode shapes for $t<0$ using the paramagnetic nature of the denser fluid. From these experiments, it was found that fluids of different viscosities behave like a fluid of almost same density-averaged viscosity for RTI purposes. Applying single-mode initial conditions at the interface, it was observed that the measurements are in close agreement with LST. Also, measured saturation growth rate constants, α were found to vary from 0.06 to 0.07 depending upon the wavelength, λ.

Waddell, Niederhaus and Jacobs (2001) have experimentally studied low Atwood number RTI with single-mode initial perturbations generated by oscillating the experimental test channel at a specified frequency. Using PLIF and a high-speed camera that traverses along with the test channel, they have measured amplitudes of bubble and spikes with time. Their measurements were found to be in good agreement with LST in the early phases and were found to have relatively constant terminal velocities for the bubbles and spikes.

To understand the present state of the art on Rayleigh Taylor instabilities, recent work by Abarzhi (2010) is paraphrased here: “Despite significant efforts, the universality of scaling h/gt^2 and λ/gt^2 and the mechanism of mixing process in RT flow still remain open issues”. Thus, emphasis is placed upon the study of details of the saturation regime with regard to the growth rate constant, α and the universality must be confirmed. Similarly, another recent work by Andrews (2010) mentions the importance of low Atwood number experiments with varying conditions as follows: “There is still to be more research to be done for small Atwood number RT involving shear and buoyancy, the effects of initial conditions, higher Reynolds number, high Schmidt number effects and cross coupling with chemistry/heat release”. The above statements emphasize the importance of the present experiments in this campaign in regard to the enhancement of the knowledge of the scientific community.

1.3.3. Summary of the literature review

From the literature review discussed above in sections §1.3.1 and §1.3.2, the current state of the art in RTI is as follows:

- Analytical theories were the starting point of RTI analysis. They are simplified, idealized and cannot account for the complex behavior of RTI.
- Some of the theories on RTI have considered shape of the fluid interface and bubble and spike curvature to describe the evolution of the instability in the linear, non-linear and mode coupling regimes.
- Many numerical simulations have been performed with varying degrees of accuracy and complexity.

- The effect of initial conditions has been studied in detail but the effect of initial perturbations on saturation and growth rates is not clarified for all Atwood numbers. Growth rates varied from study to study.
- Bubble and spike velocities also vary depending upon the model employed for solution and the 2D or 3D nature of the solution domain.
- More experimental data is needed to observe the dependence of multi-mode structures, competition and growth on component single-modes.
- The onset and growth characteristics of self-similarity are still to be clarified. Memory effects have to be studied to understand the chaotic or deterministic nature of turbulence.
- Experiments have provided data for validation of some of the numerical models. Multi-mode experiments with controllable initial conditions need to be performed for a range of Atwood numbers such that the physics of the problem can be understood.

Overall, it is essential to measure the initial conditions input into the system accurately as well as the effect of grid size on turbulence. As will be described in the coming sections §2.4, §3.3 and §3.4, a complete validation study of the fluid flow coming off the splitter plate is necessary to quantify the effect of ambient imposed initial wave numbers. This also includes the measurement of wake characteristics and molecular diffusion so that these can be parametrized and minimized. Therefore, this thesis attempts to observe the effect of binary initial conditions on the initial and self-similar growth regimes of RTI by precisely controlling the imposed initial perturbations

at the two-fluid interface and compare with literature. Future endeavors will study effect of initial conditions on the late time behavior of the flow, and the effect of multi-mode initial wave numbers.

1.4. Objective

The present set of multi-mode experiments are designed to study the effects of initial conditions on the development of Rayleigh-Taylor instabilities in the water channel. The objective of these experiments is to vary the phase-difference for a given pair of wavelengths and wavelength variation of the initial perturbation and quantify their effects. Therefore, the expected outcomes of this study are as follows:

- Perform a range of experiments with varying phase-difference and collect reliable data.
- Perform a set of experiments with varying wavelengths, such that the effect of magnitude of wavelength and the ratio of component wavelengths of binary and multi-mode initial conditions can be discerned.
- Observe the structures and obtain a relationship between the shape of the structures and the input wavelengths in the early and late-time stages. Also, to understand the physics behind mode-coupling between different modes of a multi-mode experiment.
- Do statistical growth-rate analysis of the data and study the variation of total mixing-width h and growth-rate constant α and compare with existing theories on multi-mode interactions.

- Obtain bubble and spike velocities from the high-speed images of the flow-field for comparing with existing models in literature.

The ultimate objective of this exercise is to find functional dependence of multi-modal instability growth on the component single-modes. Other outcomes of the research are to setup the facility for future experiments such that turbulent characteristics of RTI from experiments concerning late times of these flow-fields can be studied. Therefore, sets of experiments have been designed towards the objectives of:

- Validating the current water channel experimental setup.
- Studying the growth rate and mixing rate characteristics of binary initial perturbations.
- Measuring and comparing bubble and spike velocities with literature.

1.5. Organization

As explained above, section §1.1 introduces RTI along with its background theory in section §1.2. Literature review at TAMU and elsewhere is presented in sections §1.3.1 and §1.3.2 respectively, and summarized in section §1.3.3. This provides a foothold of the current state of art whereas the next few sections give an understanding of the present research, and the way to the future.

The thesis has been organized as follows: Section §2 describes the water channel experimental facility, diagnostic system and calibration procedure. Section §3.1 details the list of initial conditions input. Validation studies carried out for the servo mechanism are described in section §3.4 whereas the rest of them are explained in section §3.3.

Experimental results and discussions follow §3.5 for single mode cases, §3.1.2 for binary mode cases with phase difference variation, §3.6.2 for binary mode experiments with varying amplitude and §3.7 describes the multi-mode experimental outcomes. Each subsection entails the obtained mixing characteristics and other observations. Results of high-speed imaging are presented in Section §3.8. Finally, comparison with existing theories is provided in section §4.3 and the summary of the thesis is presented in section §4.1, including future endeavors in section §4.4. Operating procedures for different systems are attached as appendices A-F.

2. EXPERIMENTAL SETUP AND DIAGNOSTIC SYSTEM

2.1. Description of facility

The water channel facility was originally commissioned in the year 1994 in the TAMU Riverside campus. It is equipped for performing different types of experiments on Buoyancy (RTI) and shear-driven flows (KHI). A schematic of the current setup is shown in Figure 4. Listed in the figure are the components of the system. The previous setup was modified to accommodate the current servo motor system, which is used for generating the required set of initial perturbations at the flow interface. Although previously performed experiments such as those listed in section §1.3 were capable of performing binary mode experiments, the present setup has better control on prescribing the initial perturbations and repeatability. Other changes include setting up a flash system for illumination and imaging, and a high resolution Single Lens Reflex (SLR) camera. Use of the flash system is discarded in favor of the previously used backlight system because the backlight system provides higher intensities than the flash system. . Further details of the modifications on the channel system can be found in Doron (2009). Operation of the water channel is specified in section §A.1. A CAD representation of the Water channel from that thesis is shown in Figure 5.

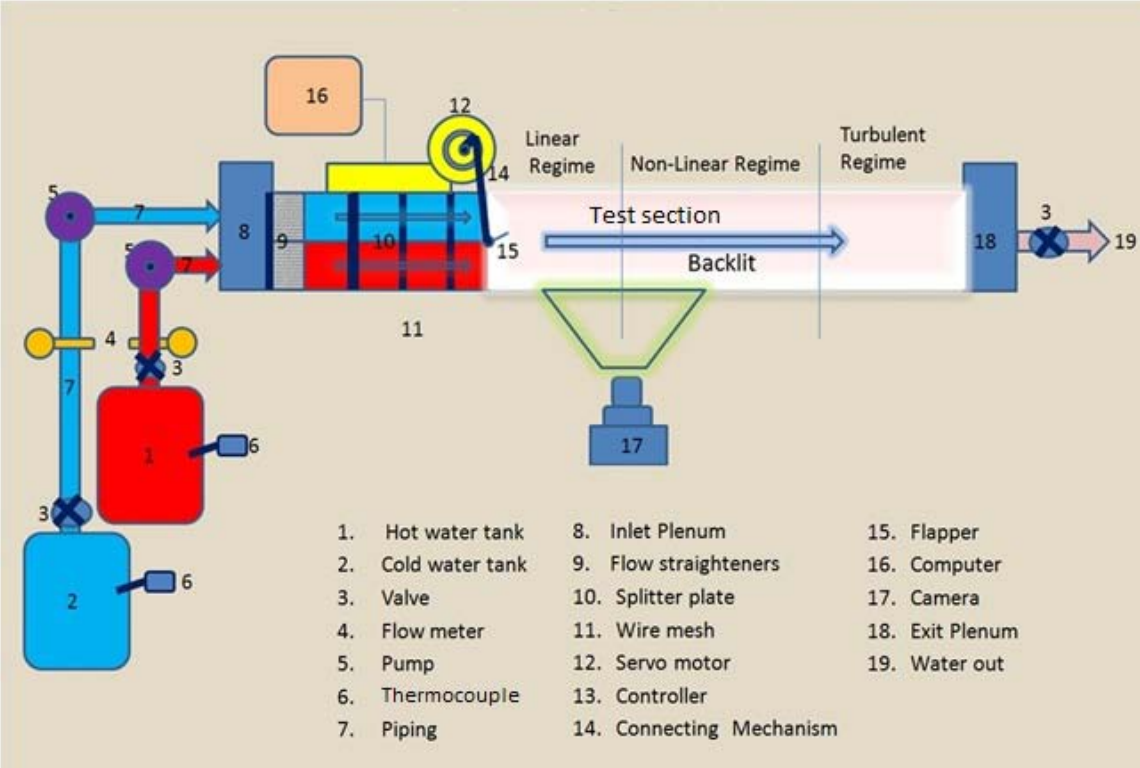

Figure 4: Schematic of water channel setup.

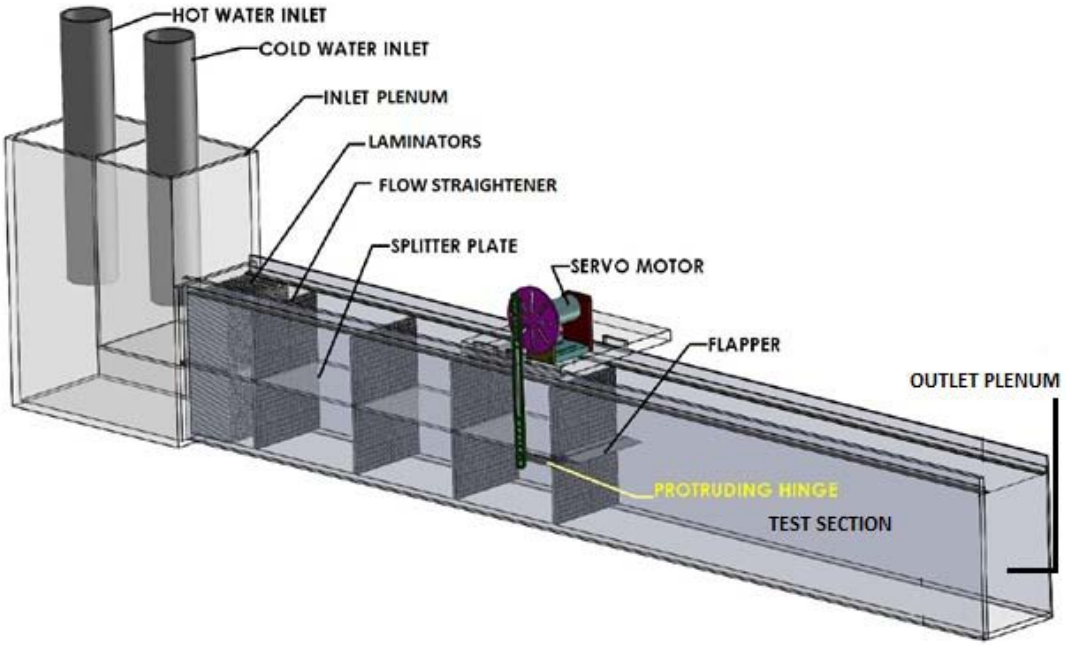

Figure 5: CAD representation of water channel.

This channel is made of ½'' Plexi-glass and is of dimensions 60''x14''x8''. The height of the upper section (from splitter plate to the top) is 7.1'' and the lower section (from splitter plate to the bottom) is of 6.9'' height. Two plastic tanks of about 550 gallons that store hot and cold water at controlled temperatures serve as working fluids. Flow from the tanks to the channel is regulated by valves and is measured by using rotameter. Two pumps attached to each of the tanks pump water from the tanks to the channel at a steady rate. Plenum chambers at the front and end of the channel serve to smooth the flow of water in and out of it. Flow straighteners placed in the early part of the channel and wire-meshes placed at regular intervals along the channel are used to regulate the flow for a laminar exit condition off the splitter plate. Splitter plates of

different thicknesses have been used in the past, and the latest set of experiments uses a splitter plate of ½'' thickness. Any bubbles that are trapped during filling water into the channel escape through holes provided at the corners of the sections of the splitter plate.

Hot water for the present set of experiments is supplied by using a heater as shown in the schematic. This heater supplies heated water to the hot water tank at an uneven temperature and therefore, the temperature of the hot water in the tank at mid-height must be monitored using a thermocouple. An E-type thermocouple with handheld digital reader is used for this purpose. As Chlorine content in the supply water varies on a daily basis, a 2.0N solution of Sodium Thiosulfate ($Na_2S_2O_3$) is added to neutralize it. This is essential for the successful visualization of the experiment as the color of Nigrosene dye used as fluid marker changes to murky brown in the presence of any non-neutralized acidic content in the water. It is to be noted that Sodium Thiosulfate of 5.0gm is added to the cold water tank for every fill of the tank. This amount adds sufficient contrast for visualization and lies within the range of amount of dye corresponding to a linear variation of dye absorption with fluid density. Details of calibration procedure can be found in section §2.4.

A single-axis integrated Ethernet controlled and amplifier, model # CDS-3310® by Galil Tools Inc. is used to create the required initial conditions. This servo unit, as will be called henceforth, consists of a Power unit, which supplies the power to the amplifier unit that goes through 4000 counts for each rotation of the axis. The amplifier works on torque mode (torque can be specified as the output), and has a supply voltage of 18-72V DC and continuous voltage of 7A. The motor is equipped with a feedback

sensor that reads the actual voltage and position of the axis with time, which can be plotted along with corresponding error. The software interface of Galil Tools Inc. is used to input commands for specifying motor function. The motor is capable of performing many complicated motions of the single axis, and it is validated for accurate output to input signal in section §3.4.

Motion of the single axis is specified by specifying a contour starting at the initial rest position to the final desired position, at user specified speed, acceleration and deceleration. Smoothing functions can be applied to reduce high-frequency noise in the system. The user specifies optimized gains for the axis such that the specified contour is followed with the least possible RMS error. Using the interactive scope of aforementioned software the error bars with time can be checked instantaneously, and the system can be tuned accordingly. Operating procedures for this system are detailed in section §B.1. A snapshot of the system during a typical experiment is shown here in Figure 6:

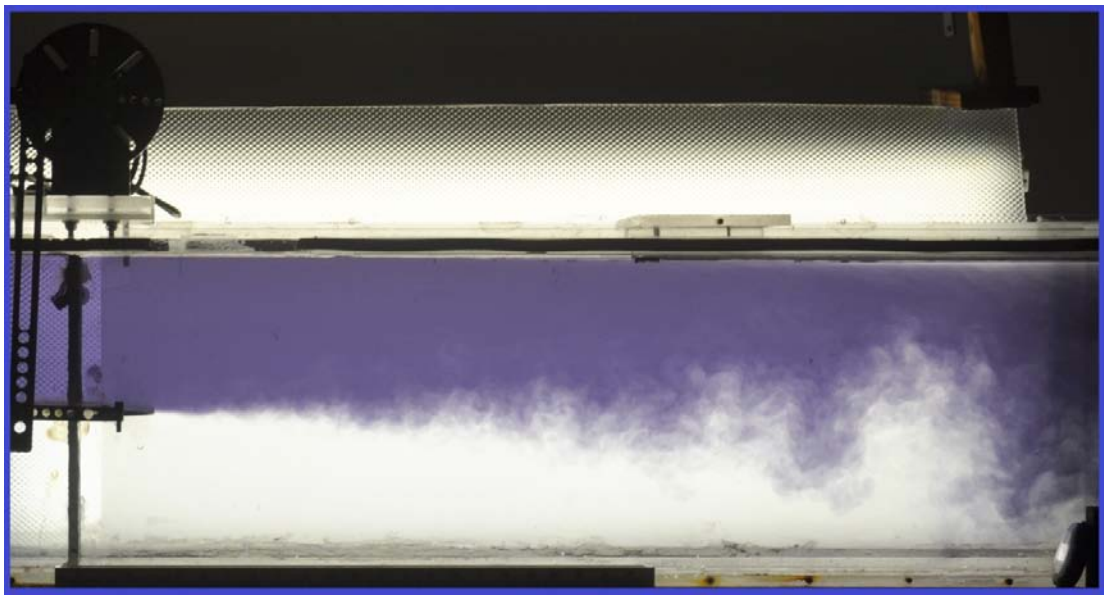

Figure 6: System snapshot during operation.

Free stream velocities of the top and bottom sections of the channel are chosen such that the all the regimes of the development of RTI can be observed at different locations in the test section. Higher free stream velocities quicken the growth rates and the height of the channel is insufficient for visualization in such instances. Reynolds number ($Re_\infty = U_\infty H/\nu$) based on the corresponding free stream velocity is provided in Table 1. An initial perturbation is defined as small only when the sinusoidal initial perturbation introduced into the system comes satisfies the following approximation:

$$y = \sin(kA) \approx kA, \text{ when } kA<<1.$$

Therefore, based on trial and error, a set of amplitudes of the initial perturbations was selected such that all regimes of the instability can be visualized. Corresponding

wavelengths of the initial perturbations, λ=20A are selected. A list of experimental parameters for all cases is given below:

S. No.	Experimental parameters		
1	Mean velocity (cm/s)	U_∞	4.7 -5.5
2	Atwood Number	At	6-10E^{-04}
3	Reynolds Number	Re_∞	1.00E^{04}
4	Wavelength (cm)	λ	2.0 - 4.0
5	Time-period (sec)	T_p	0.3-1.4

Table 1: List of experimental parameters.

2.2. Diagnostics

Backlit photography method is used for image acquisition. An array of tube-lights spaced at regular intervals set on a wooden stand is used as the source of backlight. This array is covered with a Plexiglas diffuser sheet to diffuse the light evenly. A sheet of acrylic paper is also attached to the back wall of the channel to further diffuse the light. All other sources are turned off during the experiments. As the backlight varies from image to image, image-analysis of the experimental data corrects for this variation by taking average background intensity of about 50 background images taken for every run of the experiment. Details of camera operation and image analysis can be found in the appendices §E.1 and §E.2.

For the entire ensemble averaged mixing analysis experiments, a Nikon D90® camera mounted on a tripod in front of the channel is used to take images of the flow with only backlight, at evenly spaced intervals of 1s using an automated timer. This camera provides a range of capabilities like high resolution (4288 x 2848), exposure and focus control. The camera, once set in a proper position to minimize parallax and optimize exposure, is ready to take quality images for the experiments. Images of a standard stop-watch taken with the camera in automated mode have established the accuracy to upto ± 0.1 sec.

Operating procedures for the high-speed imaging diagnostics are described in section §D.1. The Phantom-V series® camera was manufactured by of Vision Research Inc. and is capable of taking images at a rate of 1000 fps at a resolution of 512 x 256. Based on the free stream velocity of the water and the average size of the structures, a sample frequency of 1000 fps is deemed sufficient for photography such that evolution of bubbles and spikes can be recorded with adequate spatial and temporal resolution. Images were acquired for a total time of about 14.1 seconds and analyzed for bubble and spike velocities as described in section §3.8.

Temperature Measurements were performed using a standard NI based thermocouple system NI USB-TC01®. An E type thermocouple and a DAQ system with a maximum sampling rate of 4 samples per sec are used to measure temperature for a total time of about 80 seconds. Densities are calculated from temperature using the correlation obtained from measurements as specified in section §3.3.2. Accuracy of the thermocouple is ± 0.1 ^{0}C.

2.3. Calibration

For the flow visualization, we are using Nigrosene dye as fluid marker and take photographs of test section of the channel. To obtain quantitative information from these experiments, pixel intensity from the images must be correlated to dye concentration such that density of the fluid can be measured as an outcome. Density of the fluid is assumed proportional to the dye intensity. As the top section (above the splitter plate) of the test section is marked with dye, the darkest pixels correspond to cold water density, ρ_c. Similarly, the brightest pixels correspond to density of hot water, ρ_h.

The calibration method used is similar to the process described in the previous works of Snider and Andrews (1994) and (Banerjee & Andrews 2006). Amount of Nigrosene dye used was 7.0 gm. The objective was to establish a linear relationship between the Pixel intensity of the image and dye concentration, as per the Beer-Lambert's principle such that the employed 2D analysis stays valid. The Beer-Lambert's principle of visible Spectroscopy for determining concentration of absorbing species in solution states that

Equation 11: $$\frac{\partial I}{\partial z} = -\epsilon c I$$

where I_0 is the intensity of incident light into a solution, I is the transmitted intensity, z is the Spanwise distance, ϵ is the molar absorptivity and c is the concentration of the species in the solution. For the present setup, as the heavier and lighter fluids are of the same molecular composition, concentration can be treated as a marker of density. Concentration is in turn obtained from pixel intensity.

The theory by Davis and Walters (1922) details the linear relationship between exposure and pixel intensity for digital cameras. For all of the experiments, we had fixed the camera exposure setting to ISO 200. As the wedge width varies linearly with its length (15.5’’), a linear variation of pixel intensity with wedge width (7’’). Range of intensity for the current experiments is limited to about 50-220. Amounts of Nigrosene dye is measured using a digital Balance and is thoroughly mixed in the cold water of the supply tank. A new calibration wedge was designed to improve quality of the wedge surfaces for imaging. Described below is the curve corresponding to calibration performed using 7.0 gm dye in 500 gallons of cold water at 22^0C. It is to be noted that the normal range of operation for single and multi-mode experiments in the water channel corresponds to 5.0 gm of Nigrosene dye, as shown in the Figure 7.

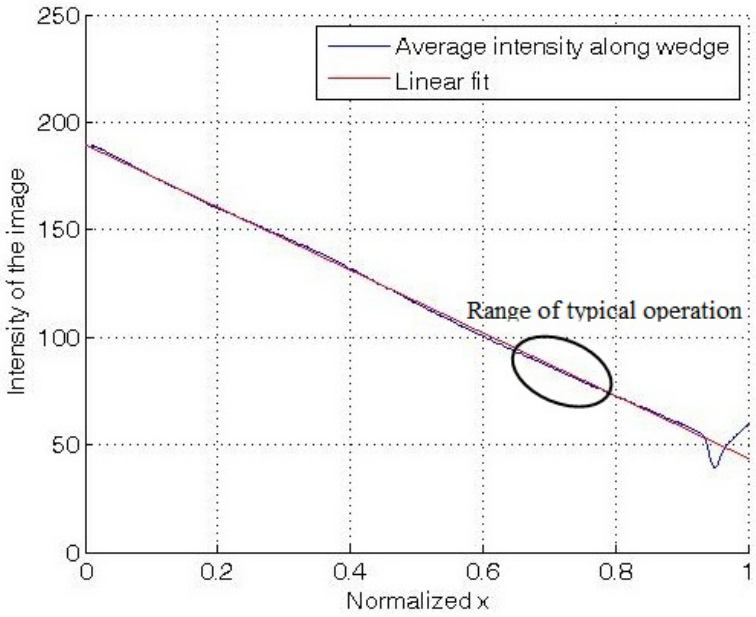

Figure 7: Calibration curve.

Shown below is a 3D view of the CAD model of the calibration wedge in Figure 8.

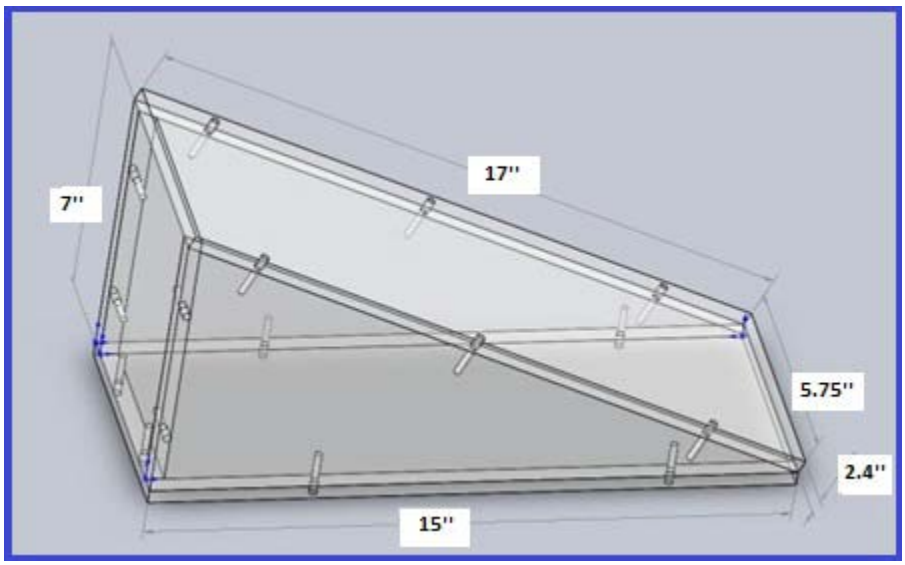

Figure 8: Calibration wedge.

The image shows CAD representation of the new calibration wedge along with its dimensions. Note that the width of the wedge is slightly less than the width of the channel. The wedge positioning is shown in Figure 9.

Image of the dye-filled calibration wedge was taken such that the concentration variation can be captured, as shown in Figure 9. Pixel intensity obtained from the image is plotted against distance along the wedge, normalized with total length of the side. Also shown in the typical configuration in which the wedge is filled with dyed water and placed inside the test section of the channel. Images are then taken with the camera axis properly positioned to be perpendicular to the channel flow-direction. As can be seen in

Figure 7, there still would be some error because of the edge roughness and parallax. Therefore, the camera must be positioned as far away as possible, with the maximum possible resolution and given zoom.

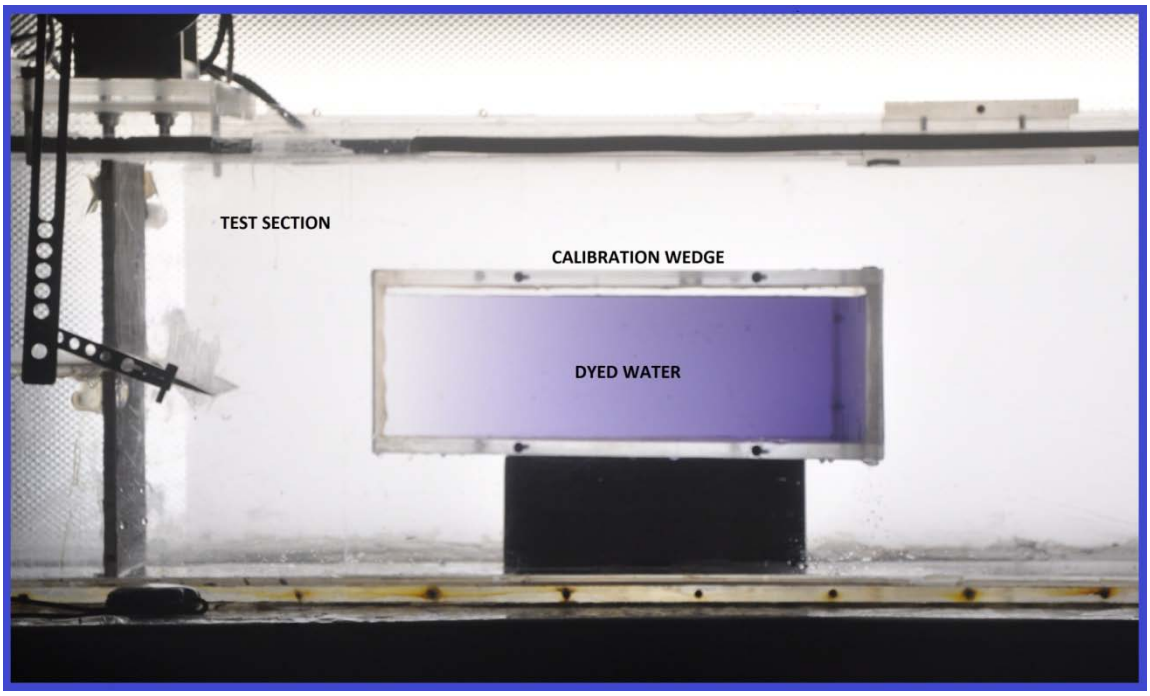

Figure 9: Calibration wedge positioning.

Image of the calibration wedge during dye calibration is plotted here. The uniformly varying dye concentration inside the wedge can be observed.

3.EFFECT OF INITIAL CONDITIONS ON RTI

From the above paragraphs, Atwood number, acceleration due to gravity and initial perturbations can be said to be the defining parameters of a specific RTI experiment. As explained the literature review section §1.3, several experiments were carried out to study the effect of Atwood number and driving acceleration on the instability. Therefore, a parametric study of initial conditions is performed here.

3.1. List of initial conditions

Each Experiment was performed with a unique initial condition at the flapper tip position. The comprehensive list of experiments performed to understand the effect of initial conditions on turbulent mixing is described here. For all experiments, λ_i/A_i equals 20. This value gives a kA of about 0.314 such that the linear approximation of small initial perturbation stands valid. Thus, time period for each wavelength is calculated from the corresponding wavelength. In order to input these initial conditions to the servo motor using Galil Tools software®, a code developed by Doron (2009) using EES® was modified. The code calculates the number of motor counts and the Time-period (in ms) for different waveforms that can be input to the servo motor. A sample program for motor motion is provided in the Appendix §B.1.

3.1.1. Single mode experiments

These set of experiments shown in Table 2 were performed to explore the effect of single-mode perturbations on RTI.

case #	λ_1 (cm)	A_1 (mm)	ω_1 (Hz)	Tp (sec)	T_c (°C)	T_h (°C)	At
1a	0	0.00	0.00	0.00	22.50	27.50	$9.04E^{-04}$
1b	2	1.00	17.91	0.35	22.50	27.50	$9.01E^{-04}$
1c	3	1.50	11.94	0.53	21.30	26.30	$8.58E^{-04}$
1d	4	2.00	8.95	0.70	22.00	27.50	$9.81E^{-04}$
1e	5	2.50	7.16	0.88	22.00	27.50	$9.81E^{-04}$
1f	6	3.00	5.97	1.05	22.00	27.50	$9.81E^{-04}$
1g	8	4.00	4.48	1.40	22.00	27.50	$9.81E^{-04}$

Table 2: List of single mode experiments.

3.1.2. Binary-mode experiments: Variation of phase-difference

These set of experiments with a varying phase difference was chosen to observe the effect of phase difference on the RTI. Table 3 lists the experimental parameters for these experiments. Waveforms for these experiments are plotted in Figure 10.

case #	λ_1 (cm)	λ_2 (cm)	A_1 (mm)	A_2 (mm)	ω_1 (Hz)	ω_2 (Hz)	(θ°)	T_1 (°C)	T_2 (°C)	At
2a	4	2	2	1	8.95	20.54	0	19.90	24.90	$8.08E^{-04}$
2b							45	19.90	24.90	$8.08E^{-04}$
2c							90	19.90	24.90	$8.08E^{-04}$
2d							135	19.90	24.90	$8.08E^{-04}$
2e							180	20.10	25.00	$7.97E^{-04}$
2f							225	20.10	25.00	$7.97E^{-04}$
2g							270	20.10	25.00	$7.97E^{-04}$
2h							315	20.10	25.00	$7.97E^{-04}$
2i							360	20.10	25.00	$7.97E^{-04}$

Table 3: List of binary mode experiments with varying θ.

As it can be observed from Figure 10, introduction of a phase-difference in the waveform results in a different shape of the waveform. Even though the instantaneous waveforms are different for each of these experiments (2a-2i), the time averaged displacement comes to a zero for sinusoidal perturbations. Therefore, it could be postulated that the ensemble averaging of the RTI over a large period of time will not exhibit any difference in growth rates or mixing widths. This is detailed in §3.6.1.

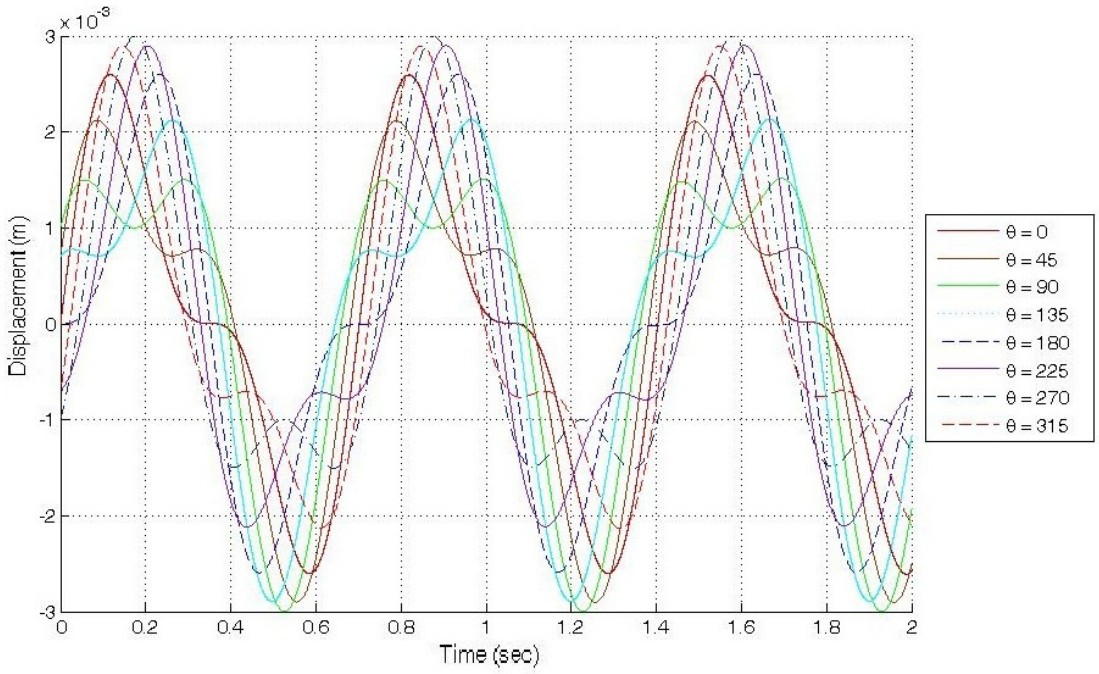

Figure 10: Binary waveforms with varying phase-difference: y_{bin} (θ) vs. t.

Plots of the average displacement, velocities and energy are shown in Figure 11, Figure 12 and Figure 13 respectively. In this analysis, the displacement, velocities and

energy of the binary waveform for any specific phase difference were averaged for the duration for which the flapper was above (Top) and below (bottom) of the splitter plate. For each experiment, minimum, mean and maximum values of above parameters from these plots provide information on the nature of the waveform that is introduced into the otherwise density stratified flow with no shear. Total displacement, which is the sum of mean displacements during which the flapper is in the top and bottom sections, is also plotted. Also, plotted is the line corresponding to zero displacement. Similar to the plots of displacement in Figure 11, plots of minimum, mean and maximum y velocity are plotted in Figure 12. This exercise is repeated for all of the binary and multi-mode experiments, and was deemed helpful in understanding the fluid structures visualized.

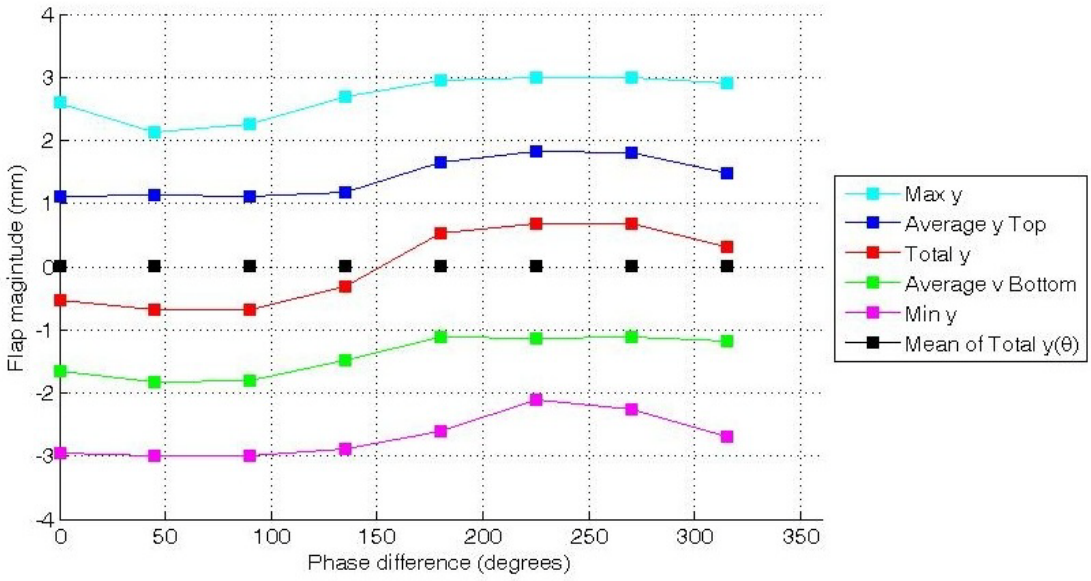

Figure 11: Time-mean of the flapper tip displacement, $\overline{\boldsymbol{y}}$ vs. phase-difference θ.

Flapper tip velocities are obtained from the displacement profiles and the plots of *u* and *v* are shown in Figure 12.

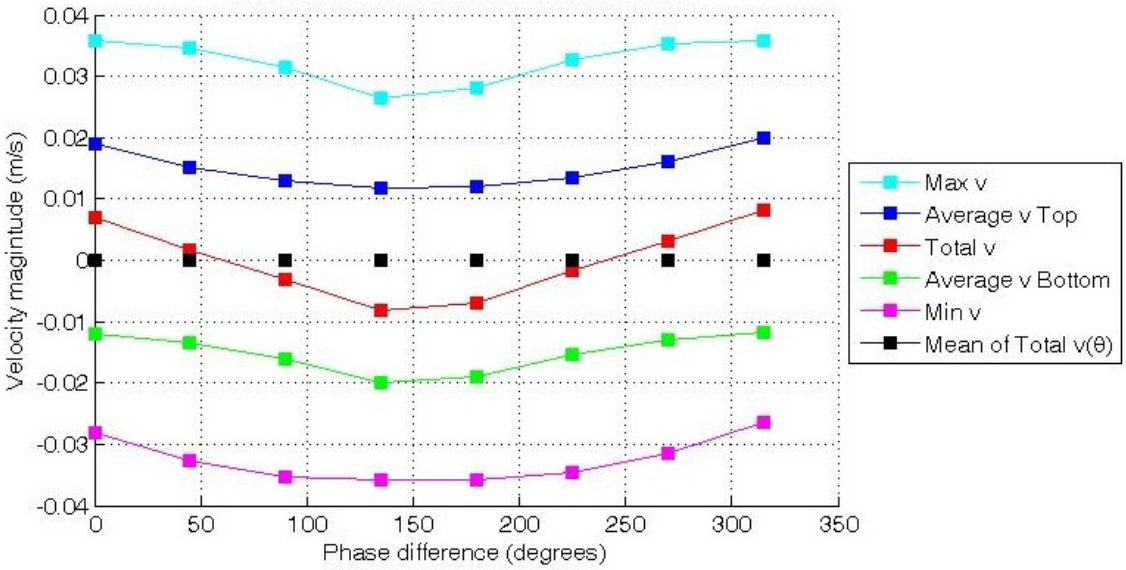

Figure 12: Time-mean of flapper tip velocity $\bar{v}$ vs. phase difference θ.

From the Figure 12, it could be observed that the flapper does not induce any net average velocity in the streamwise direction. The largest velocity *v* is induced into the denser fluid when θ=0°, whereas the smallest induced *v* corresponds to θ=180°. Similarly, the largest velocity *v* is induced into the lighter fluid when θ=315°, whereas the smallest induced *v* corresponds to θ=0°. Also shown are the maximum and minimum velocities for each phase difference. It is expected that the shape of the waveform coming off the plate is related to the maximum *v* of the flapper tip. Figure 13 shows the variation of time-mean of power deposited by the flapper into the top and bottom sections of the channel. Power is obtained by the relation:

Equation 12: $$\dot{e_{top}} = \rho y_{top} b U_{\infty} (u_{top}{}^2 + v_{top}{}^2)$$

where ρ is the density of water, y_{top} is the time-mean displacement of flapper tip in the top section, b is the width of the channel, u_{top} is the time-mean u in the top section and v_{top} is the time-mean v in the top section. A similar exercise can be performed for the bottom section of the channel.

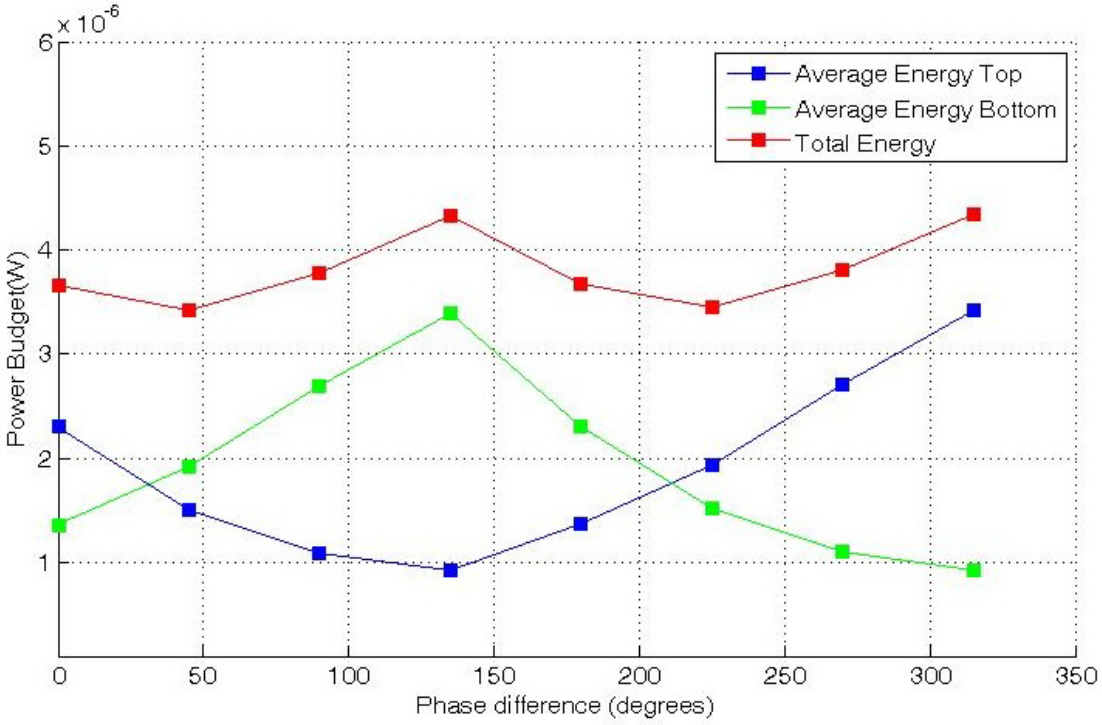

Figure 13: Time-mean of energy deposited vs. phase-difference θ.

From the above displacement, velocity and energy plots, we get an estimate of the magnitude of disturbance introduced into the flow by the flapper, which can be related to the mixing layer growth in the top and bottom sections of the channel respectively.

3.1.3. Binary-mode experiments: Variation of amplitude

The next set of experiments was carefully chosen to explore the effect of variation of amplitude on RTI such as the effect of ratio of amplitudes, and the average magnitude of amplitude above or below the X-axis. As shown in Table 4, the cases (3a-3e) have a constant λ_2=2cm, whereas λ_1 is varied. Experiment (3f) corresponds to a special case of $\lambda_1 = \lambda_2$ =4cm. Case (3b), (3g) and (3i) correspond to λ_1/λ_2 of 2.0. Cases (3e) and (3h-3j) correspond to λ_1=8cm, whereas λ_2 was varied uniformly. For all experiments, a phase-difference of θ=45° was chosen such that the component waves are out of phase but the phase-difference is not too large.

	case #	λ_1 (cm)	λ_2 (cm)	ω_1 (Hz)	ω_2 (Hz)	(θ°)	T_1 (°C)	T_2 (°C)	At
λ_1 varied, λ_2 constant	3a	3	2	11.94	20.54	45	20.10	24.90	$7.79E^{-04}$
	3b	4	2	8.95	20.54		20.10	24.90	$7.79E^{-04}$
	3c	5	2	7.16	20.54		20.10	24.90	$7.79E^{-04}$
	3d	6	2	5.97	20.54		20.10	24.90	$7.79E^{-04}$
	3e	8	2	4.48	20.54		20.10	24.90	$7.79E^{-04}$
	3f	4	4	8.95	8.95		20.10	24.80	$7.61E^{-04}$
	3g	6	3	5.97	11.94		20.10	24.80	$7.61E^{-04}$
λ_2 varied, λ_1 constant	3h	8	3	4.48	11.94		20.10	24.80	$7.61E^{-04}$
	3i	8	4	4.48	8.95		20.10	24.80	$7.61E^{-04}$
	3j	8	5	4.48	7.16		20.10	24.80	$7.61E^{-04}$

Table 4: List of binary mode experiments with varying A_i.

The time varying waveforms are shown in Figure 14 for a constant λ_2. A bubble or spike is release from the flapper every time the waveform reaches a maximum or minimum value respectively. Figure 15 shows the binary waveform for the set of cases

for which λ_1 / λ_2 =2.0. Therefore, observation of the images or videos of the initial stages of the RTI should be able to exhibit this phenomenon.

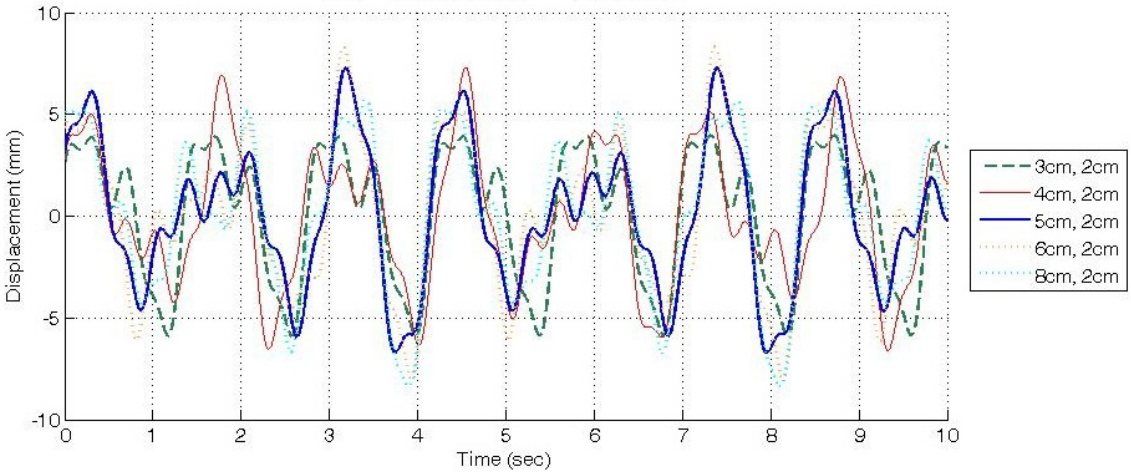

Figure 14: Binary waveforms with amplitude variation vs. time, constant λ_2.

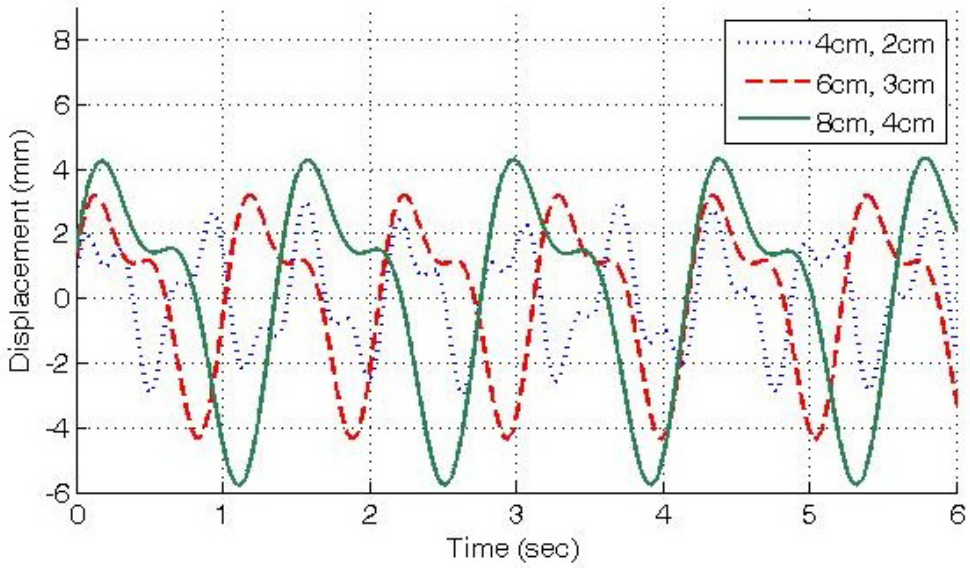

Figure 15: Binary waveforms with amplitude variation vs. time for $\lambda_{1/}\lambda_{2=}$ 2.0.

Characteristic time-mean, maximum and minimum of displacements, velocities and energies are computed and plotted for various cases and are shown in Figure 16, Figure 17 and Figure 18 respectively. The aim is relate these variations to the ensemble averaged mixing widths and size and shape of the bubbles and spikes emanating from the flapper tip point.

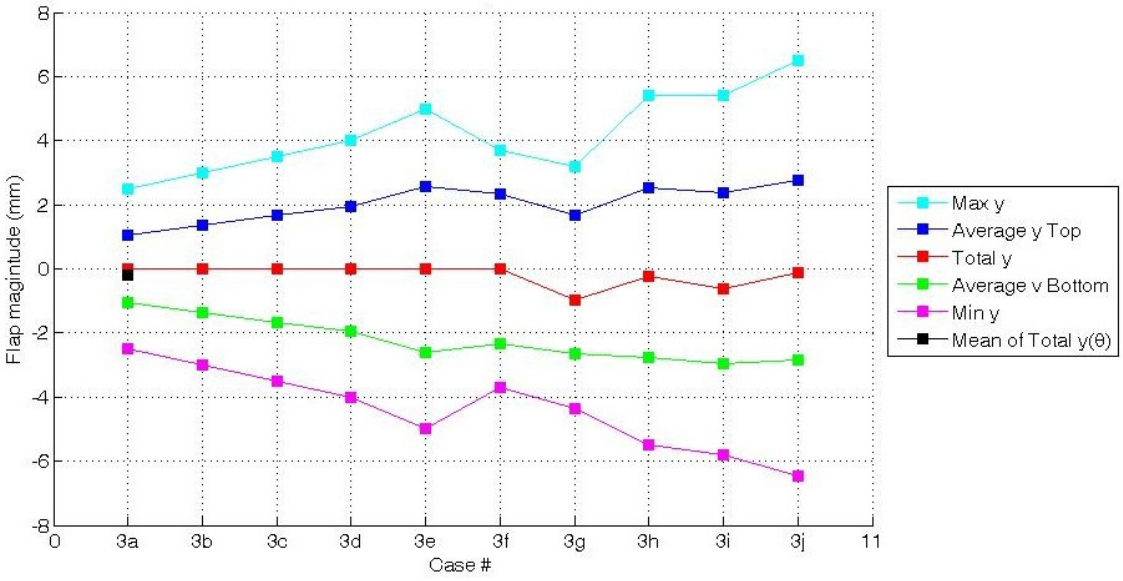

Figure 16: Time-mean of flapper tip $\bar{y}$ vs. experiment#.

Calculated flapper tip characteristic displacements plotted for binary mode experiments with varying amplitude are presented here.

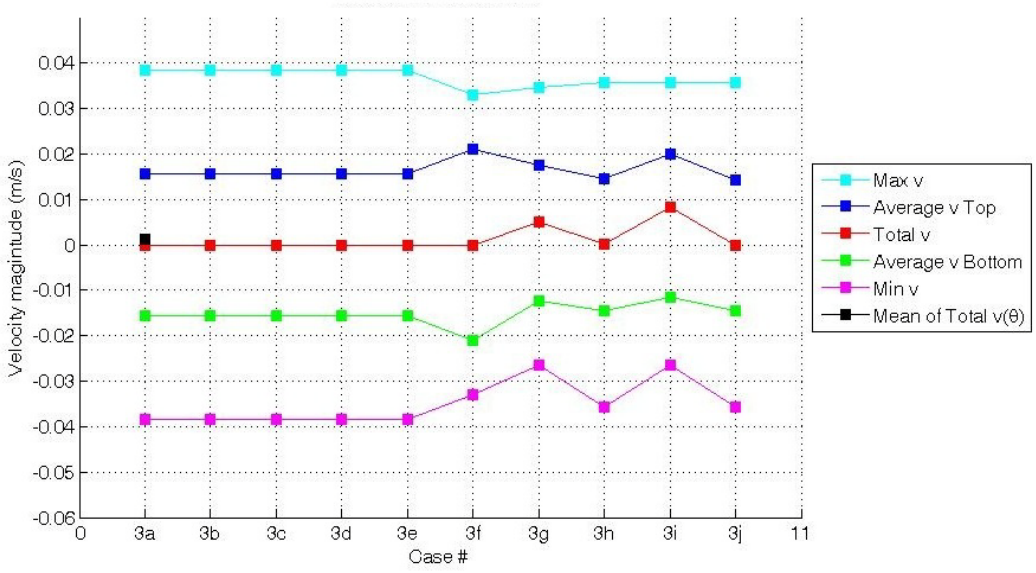

Figure 17: Time-mean of flapper tip $\bar{v}$ vs. experiment#.

Calculated flapper tip characteristic velocities plotted for binary mode experiments with varying amplitude are presented here.

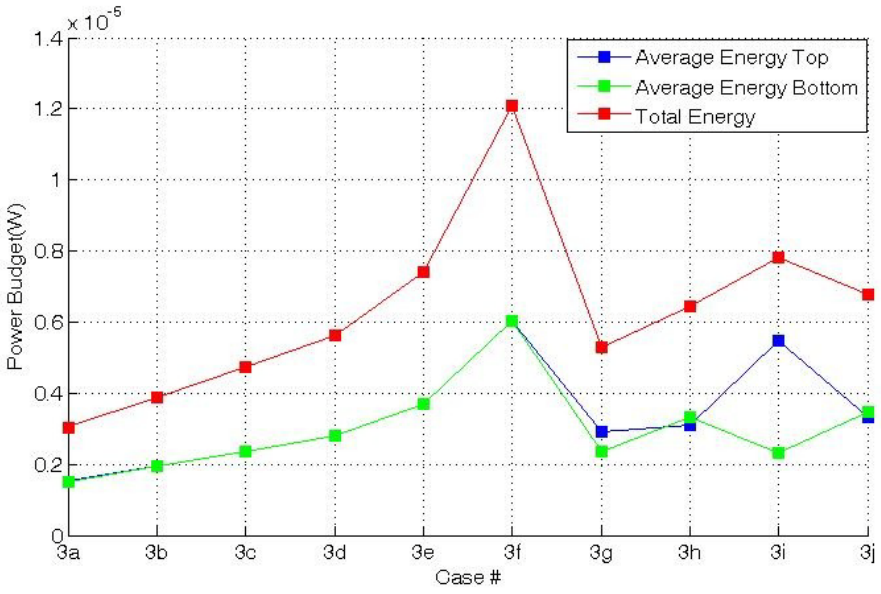

Figure 18: Time-mean of flapper tip $\dot{\boldsymbol{e}}$ vs. experiment#.

Calculated flapper tip characteristic energies plotted for binary mode experiments with varying amplitude are presented here.

3.1.4. Multi mode experiments

A unique set of experiments was performed to observe the above mentioned effects to a higher degree. Therefore, multi-mode (3 or higher) modal perturbations were introduced at the interface using the new flapper technique. To the author's knowledge, these are the first well controlled low Atwood number experiments performed to understand RTI. Table 5 shows the list of multi-modal experimental parameters.

case #	λ_1 (cm)	λ_2 (cm)	λ_3 (cm)	λ_4 (cm)	A_1 (mm)	A_2 (mm)	A_3 (mm)	A_4 (mm)
4a	8	4	2		8.0	2.0	1.0	
4b	8	5	2		8.0	2.5	1.0	
4c	8	6	2		8.0	3.0	1.0	
4d	8	6	3	2	8.0	3.0	1.5	2
4e	8	6	4	2	8.0	3.0	2.0	2

case #	ω_1 (Hz)	ω_2 (Hz)	ω_3 (Hz)	ω_4 (Hz)	(θ_1°)	(θ_2°)	(θ_3°)	T_1 (°C)	T_2 (°C)	ρ_1 (g/cc)	ρ_2 (g/cc)	At
4a	4.48	8.95	17.91		45	90		20.8	25.8	0.999	0.998	$6.6E^{-04}$
4b	4.48	7.16	17.91		45	90		20.8	25.8	0.999	0.998	$6.6E^{-04}$
4c	4.48	5.97	17.91		45	90		21.1	26.1	0.999	0.998	$6.1E^{-04}$
4d	4.48	5.97	11.94	17.91	45	90	135	21.1	26.1	0.999	0.998	$6.1E^{-04}$
4e	4.48	5.97	8.95	17.91	45	90	135	21.1	26.1	0.999	0.998	$6.1E^{-04}$

Table 5: List of multi-mode experimental parameters.

3.1.5. Single mode experiments for velocity measurement

To measure the spike and bubble velocities for comparison with literature, next set of cases was chosen with single-mode initial conditions as given below in Table 6.

case #	λ_1 (cm)	A_1 (mm)	ω_1 (Hz)	Tp (sec)	T_1 (°C)	T_2 (°C)	At
h12	2	1.00	17.91	0.351	23.80	28.70	$9.27E^{-04}$
h13	3	1.50	11.94	0.526	23.80	28.70	$9.27E^{-04}$
h14	4	2.00	8.95	0.702	23.80	28.70	$9.27E^{-04}$
h15	5	2.50	7.16	0.877	23.80	28.70	$9.27E^{-04}$
h16	6	3.00	5.97	1.053	23.50	28.70	$9.78E^{-04}$
h18	8	4.00	5.97	1.053	23.50	28.70	$9.78E^{-04}$

Table 6: List of experiments for velocity measurement.

3.2. Novelty of the current experiments

The novelty of the present investigation at TAMU is that the multi-mode experiments are performed in a repeatable, reliable and controlled manner. Application of a high-accuracy servo motor that provides feedback is the key to controlling the initial conditions in a preferable fashion. Although the diagnostic system is unable to capture the minute differences in phase and amplitude, the servo system is capable of sensitive measurements of angle upto 36/4000 degrees and amplitude upto a count of 0.45mm. Therefore this mechanism has inherent lower uncertainties than the other components of the Water-channel system.

Uncertainty analysis of the system performed by Doron (2009) has shown that the major sources of error in this system are due to vibrations induced by a nearly-laminar water flow out of the laminators in the top and bottom sections of the channel. Other sources of uncertainty are due to inaccuracies in velocity measurement, temperature measurement associated with Thermocouple, parallax error, free-stream turbulence introduced by the wire-meshes, and the thickness and roughness of the flapper and splitter plate. This was witnessed in the measured error in flapper motion using the servo feedback. A typical signal from the servo motor is shown in the figure on page 128. The step size input into the Galil tools® code written for operating the servo motor was optimized for highest possible accuracy and least possible high-frequency noise. Too large a step size would result in inaccurate tracing of the specified contour by the motor axis, whereas too small a size would result in increased high frequency noise.

3.3. Validations studies

3.3.1. Milk and dye experiments

The first step was to understand the physical processes that constitute RTI. So a set of experiments were performed to visualize the flow fields at different locations, using different methods. A typical water channel RTI experiment with no input perturbation by the flapper using milk as marker for hot water and a ΔT of 5°C is shown in Figure 19. Visualization using a mix of 5% milk in water for 45'' of the channel length is shown.

Figure 19: Milk visualization of RTI.

The purpose of this visualization technique is to clearly identify the structures arising due to RTI, and milk which diffuses slower than water enables the structures to be observed with higher distinction. This is a qualitative technique with no measureable outputs. A similar experiment with Nigrosene dye marker is shown below in Figure 20.

Figure 20: Dye visualization of RTI.

Grid meshes used for breaking down the boundary layer and other large scale structures in the flow act as source of turbulence in the free stream. This was limited to as low as possible as otherwise turbulent mixing might dominate RTI induced mixing. Therefore, dye was injected into the free stream using a syringe and its path was observed until the end of the channel. It was concluded that free stream turbulence values were fairly low because the blob did not change shape significantly due to diffusion and viscosity.

To observe the growth of the boundary layer arising from the flapper and to ensure the flapper reference position is horizontal, a blob of Nigrosene dye was dropped on the splitter plate near the exit section of the splitter plate, with no temperature gradient and flap. The streaklines of the dye can be observed in Figure 21 from a very smoothly polished splitter plate and flapper.

Figure 21: Dye streaklines from flapper tip.

Free stream velocity was measured using a similar technique, where a blob of dye was dropped into the stream at very low relative velocity and images of the channel taken at 0.25 second intervals using a high resolution camera. By measuring the pixel distance moved, the free stream velocity was measured to be about 5.79 cm/s for the single-mode experiments and about 6.1 cm/s for the binary set of experiments.

3.3.2. Density measurement

3.3.2.1. Introduction

Over the period of research using the Water channel facility, there has been a discussion over the methods of calculation of Atwood number for the experiments. Because of the nature of tap water supply and the addition of Sodium Thiosulfate ($Na_2S_2O_3$) and Nigrosene dye to the water, a comprehensive study of the density of water samples with temperature was warranted. Therefore, a highly accurate Densitometer was employed for these purposes, and Atwood numbers were calculated from the density measured using densitometer.

The Densitometer DDM 2911® is manufactured by Rudolph Research Analytical Inc. and is used for density and concentration measurements. It works on the principle of resonance of the internal U-tube with and without the liquid sample. The resonance frequency gives a measure of the mass contained in the given volume of the tube and a specified temperature. The calibration procedure of the Densitometer adheres to the NIST database and has a 6-decimal precision. Further details of operation of the Densitometer can be found in Appendix §C.1

3.3.2.2. Measurement

Water samples were taken for density measurements in the operating range of 15-35°C. This section aims to verify the accuracy of Kulkula's correlation (1981) for equation of state used in the previous works which is:

Equation 13:

$$\rho(kg/m3) = (999.8396 + 18.2249T - 0.007922T^2 - 55.448 \times 10^{-6}T^3 + 149.756 \times 10^{-9}T^4 - 393.295 \times 10^{-12}T^5)/(1 + 18.159 \times 10^{-3}T)\ (T\ in\ ^0C)$$

3.3.2.3. Effect of Sodium Thiosulfate, Nigrosene

100ml of 2.0N Sodium Thiosulfate, a base added to each water tank sample to neutralize the Chlorine content. It is to be noted that in the previous experiments, 50ml of Sodium Thiosulfate was added. As it was observed by trial and error that the Chlorine content of supply water varies from day to day, 100ml was deemed sufficient for all experiments after extensive trials.

Water samples were taken with and without sodium Thiosulfate and density of the samples measured at different temperatures. Similarly, density measurements were performed with and without Nigrosene to the water with added Sodium Thiosulfate. Typically, 5.0gm of Water soluble Nigrosene dye was added to the cold tank during each experiment. The variation is plotted in Figure 22, which shows the density of tap water increases with addition of Sodium Thiosulfate except at lower temperatures. The maximum variation in density amounts to about 0.019%. Addition of Nigrosene to the Water with Sodium Thiosulfate changes density by a maximum 0.006%, which is comparable to the precision of the Densitometer. Therefore, for all purposes, the effects of Sodium Thiosulfate and Nigrosene on the tap water can be assumed to be insignificant.

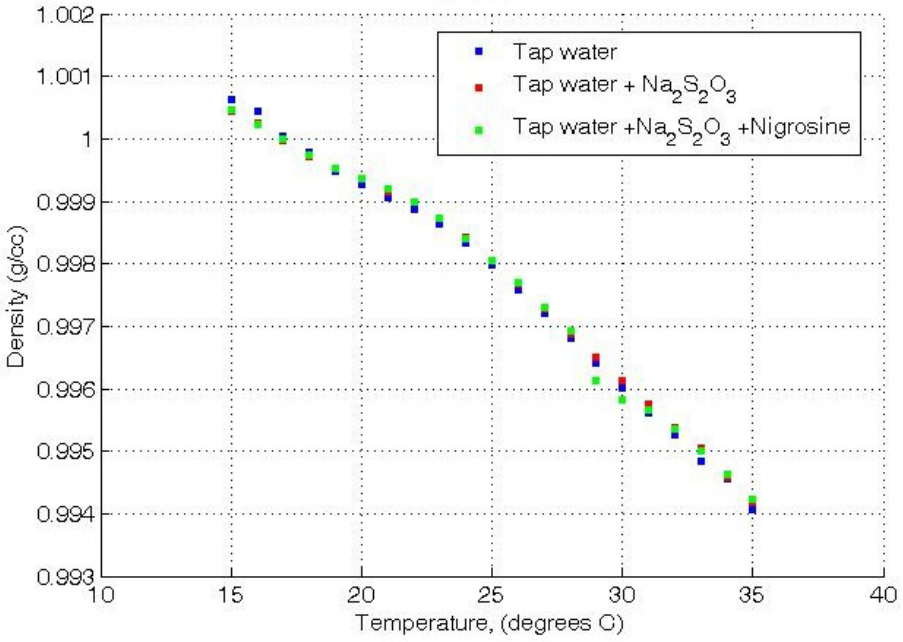

Figure 22: Effect of sodium thiosulfate and nigrosene on water density.

Measured density of water samples plotted with temperature.

3.3.2.4. Density comparison: Measured vs. NIST database & Kulkula's correlation

As can be seen from Figure 23, there is a difference in measured density and NIST data or Kulkula's correlation at lower temperatures but the density values collapse at higher temperatures. The maximum variation is about 0.15% which corresponds to a temperature of 15°C. The variation with NIST data can be attributed to the presence of chemicals in the tap water as compared to laboratory pure water. From the plots, it is evident that Kulkula's correlation has a fair match with NIST data. Measured density of tap water at different temperatures is shown in Table 7 along with Kulkula's Correlation and NIST data values. The attributed difference in density between the measured and Tap water values can be attributed to the chemicals that may be present in College Station supply water. Table 7 is also presented as Figure 22. Maximum variation between measured densities of supply water with NIST database value is about 0.154%.

S. No.	Temperature (°C)	Measured Density (ρ) g/cc	NIST density value (g/cc)	Correlation density (g/cc)	% variation between measured and NIST data	% variation between measured and Kulkula's
1	15	1.00064	0.999099	0.9991086	0.154	0.153
2	16	1.00043	0.998942	0.9989526	0.149	0.148
3	17	1.00004	0.998774	0.9987850	0.127	0.126
4	18	0.99978	0.998595	0.9986062	0.119	0.118
5	19	0.99949	0.998404	0.9984164	0.109	0.108
6	20	0.99927	0.998203	0.9982159	0.107	0.106
7	21	0.99906	0.997991	0.9980048	0.107	0.106
8	22	0.99886	0.997769	0.9977833	0.109	0.108
9	23	0.99863	0.997537	0.9975518	0.110	0.108
10	24	0.99833	0.997295	0.9973104	0.104	0.102
11	25	0.99797	0.997043	0.9970592	0.093	0.091
12	26	0.99759	0.996782	0.9967985	0.081	0.079
13	27	0.99721	0.996511	0.9965284	0.070	0.068
14	28	0.99681	0.996232	0.9962492	0.058	0.056
15	29	0.99642	0.995943	0.9959609	0.048	0.046
16	30	0.99602	0.995645	0.9956637	0.038	0.036
17	31	0.99562	0.995339	0.9953579	0.028	0.026
18	32	0.99527	0.995024	0.9950434	0.025	0.023
19	33	0.99485	0.994700	0.9947205	0.015	0.013
20	34	0.99456	0.994369	0.9943893	0.019	0.017
21	35	0.99406	0.994029	0.9940500	0.003	0.001

Table 7: Density of water: Measured vs. NIST data & Kulkula's correlation.

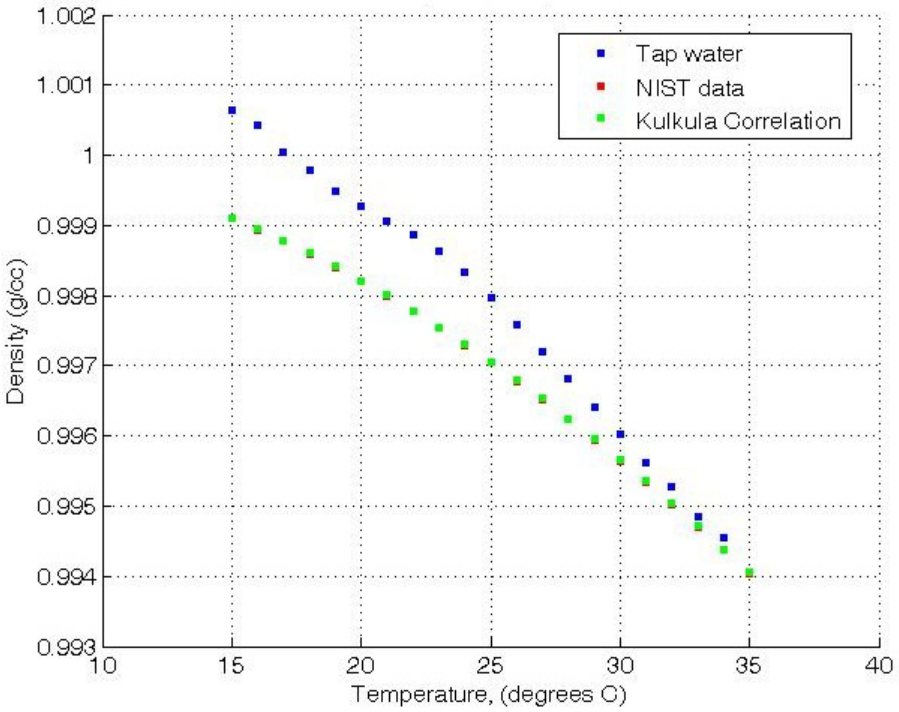

Figure 23: Density of water: variation with temperature.

Density obtained from measured vs. NIST data and Kulkula's correlation is plotted here.

Also shown in Figure 24 is a plot of Atwood number with Mean temperature of the sample for 5°C of temperature difference. The plot shows a similar trend to the correlation but the Atwood number is offset by about 30%. Fourth order polynomial fits to the data provide a smooth trend in Atwood number variation. Therefore, new correlations for density and Atwood numbers as a function of temperature of the water sample with added Sodium Thiosulfate and Nigrosene can be proposed for all further experiments with ΔT =5°C, as follows:

Equation 14:

$$\rho\left(\frac{g}{cc}\right) = -8.61 \times 10^{-9}T^3 - 6.496 \times 10^{-6}T^2 - 1.8515 \times 10^{-5}T + 1.0023\ (T\ in^0C)$$

Equation 15:

$$At = \frac{(1.2915 \times 10^{-7}T^2 + 6.4507 \times 10^{-5}T + 2.5604 \times 10^{-4})}{(-1.722 \times 10^{-8}T^3 - 1.312 \times 10^{-5}T^2 - 2.7456 \times 10^{-4}T2.0046)}\ (T\ in\ ℃)$$

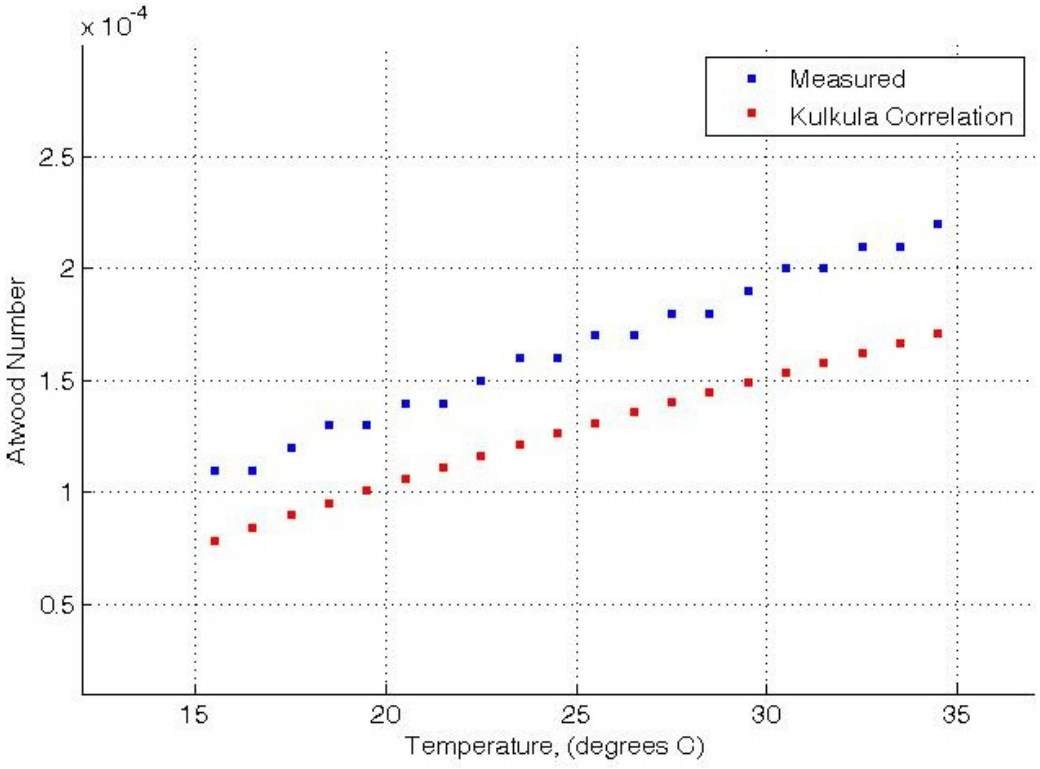

Figure 24: Measured and correlation *At* vs. mean temperature.

Atwood number calculated from measured data and Kulkula's correlation is plotted here for comparison.

From the above, it can be concluded that measured density values are preferred over Kulkula's correlation and the above Equation 14 can be used for density calculation and Equation 15 can be used for Atwood number calculation.

3.3.2.5. Atwood number variation with ΔT

To further explore the effect of *ΔT* on the variation of Atwood number with temperature, Atwood number is calculated from measured density values for different ranges of temperature *ΔT* and plotted in Figure 25. From the plot, it could be observed that the variation in Atwood number for Measured and Kulkula's correlation is smaller for smaller *ΔT*. For the present range of *ΔT* used in low Atwood number water channel experiments, measured density is more accurate.

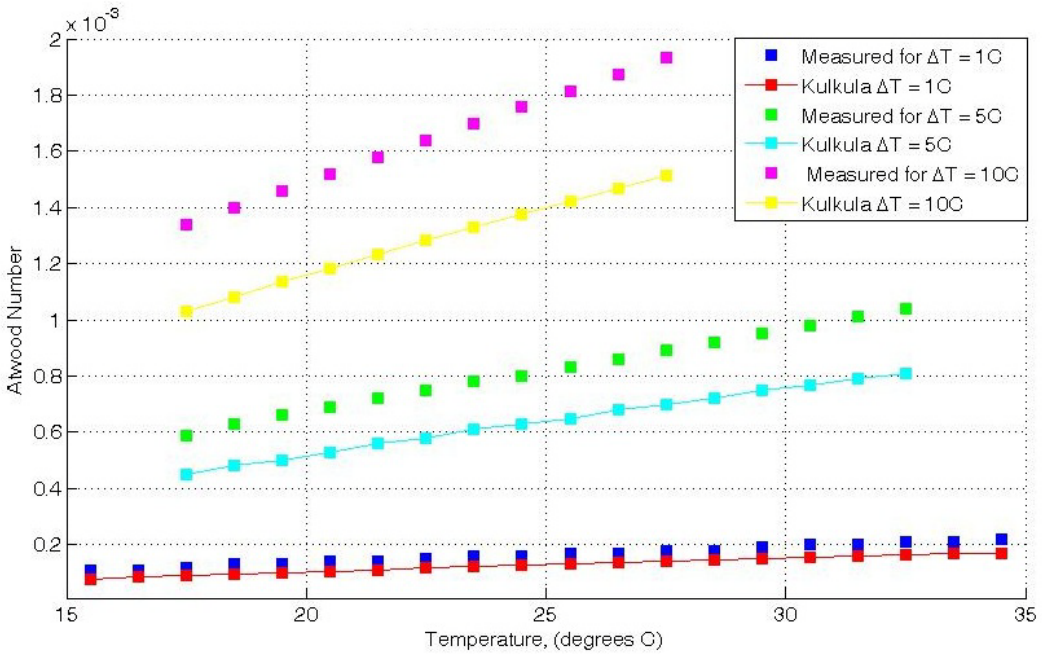

Figure 25: Measured and correlation *At* vs. temperature for different ΔT.

3.4. Servo motor validation

This section outlines the steps taken to validate the accuracy of the servo motor described in section §3.4. As the most significant modification to the previous methods of generating initial conditions, the accuracy and repeatability of the servo motor mechanism must be established for enhanced control. Operating procedures of this motor are detailed in appendix §B.1. A basic chart plotter is used for plotting the motion of required components of the mechanism. An ink marker that is attached to the required component moves on graph sheet loaded into the plotter when the servo is set into motion. The graph sheet moves at a constant speed of 30 cm/min. The plots are then measured with appropriate scaling and are presented here. Validation is performed at various stages of the motion transmission to check for sources of vibrations in the system.

3.4.1. Motor axis validation

A marker is attached to the pulley which is sturdily mounted on the motor axis. A time sample of 4 cycles out of a large duration of time was taken. Response plot for a single-mode motor motion taken specified by $y = 1 \times sin\left(\frac{t}{5}\right)$ (y in cm, t in sec) is shown in Figure 26. The waveform is slanted to the left because of the relative motion between the marker and the graph sheet. The motor was stopped for a small duration to check if it starts at the same position it was stopped. Measured amplitude is accurate upto 99%, while the time-period is accurate upto 98%.

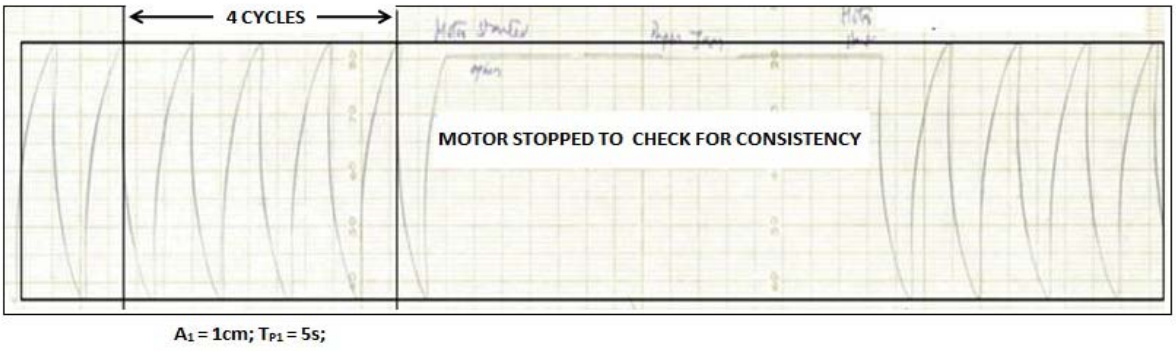

Figure 26: Servo motor single-mode response.

As high-frequency noise was observed during some practice multi-mode experiments, motion of the motor axis given by $y = 3 \times sin\,(\frac{t}{5}) + 1 \times sin\,(\frac{t}{2} + 0^0)$ (y in cm, t in sec) is plotted in Figure 27. A time sample of 7 cycles out of a large duration of time was taken.

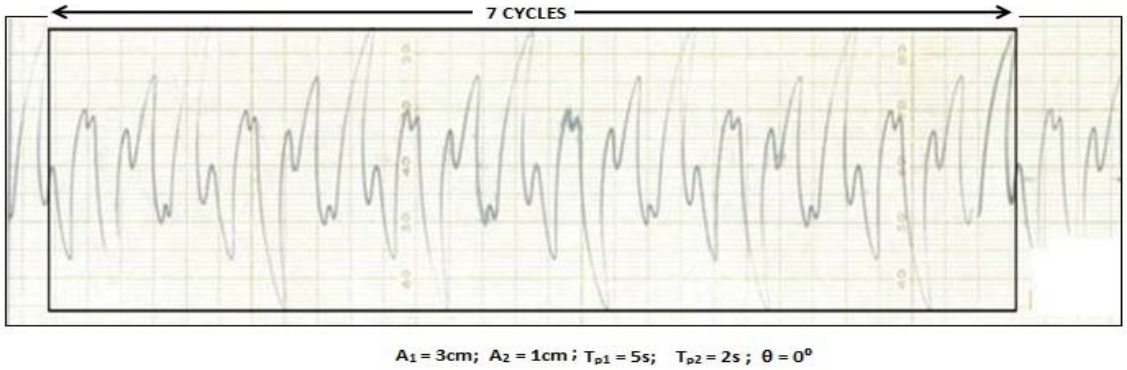

Figure 27: Servo motor binary-mode response.

3.4.2. Flapper tip validation without channel operation

The water channel was emptied and a marker of exactly the same length as the flapper is attached to the protruding arm of the flapper axis as shown in Figure 28. A time sample of 12 cycles out of a large duration of time was taken. Response plot for a single-mode motor motion given by $y = 1 \times sin\,(\frac{t}{5})$ (y in cm, t in sec) is shown in Figure 28.

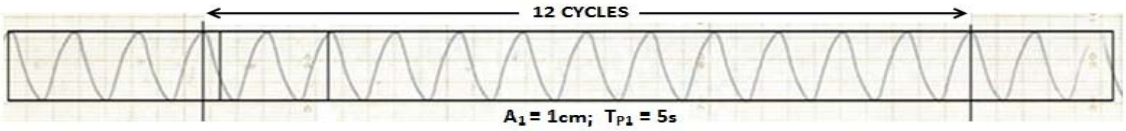

Figure 28: Flapper tip single-mode response.

A similar exercise was performed for multi-mode motion specified by $y = 3 \times sin\,(\frac{t}{5}) + 1 \times sin\,(\frac{t}{2} + 0^0)$ (y in cm, t in sec) is plotted in Figure 29. A time sample of 7 cycles out of a large duration of time was taken. Measured amplitude is accurate upto 98% while measured time-period is accurate by 95%.

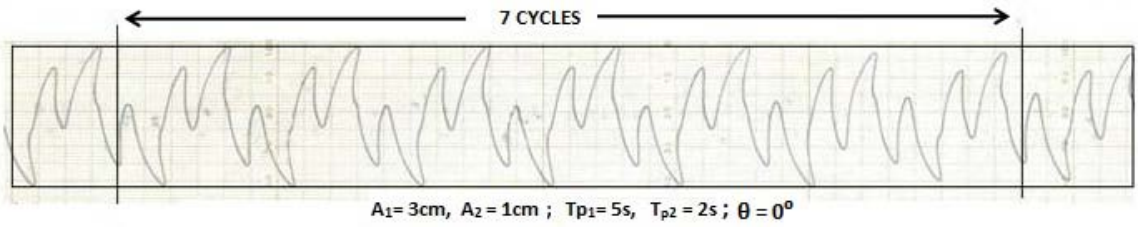

Figure 29: Flapper tip binary-mode response.

The above validation suggests that the flapper system is fairly accurate. It can be deduced that the vibration of links connecting the flapper to the pulley could be a possible source of error.

3.4.3. Flapper tip validation during water channel operation

Similar exercise to §3.4.2 was performed with the water channel operating and pumps turned on, to measure the effect of induced vibrations due to the flapper contact with running water. Single-mode response of marker specified by $y = 2.36 \times \sin(\frac{t}{1})$ (y in cm, t in sec) is shown in Figure 30 and multi-mode response given by $y = 3 \times \sin(\frac{t}{10.53}) + 2.4 \times \sin(\frac{t}{27.7} + 0^0)$ (y in cm, t in sec) is given below in Figure 31.

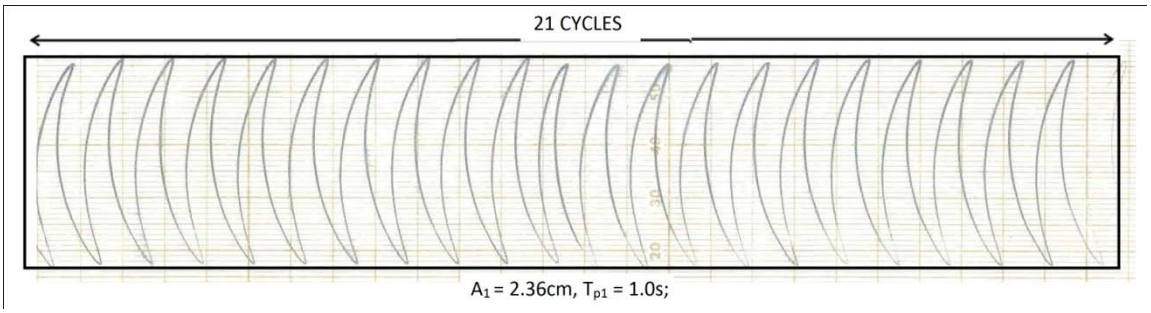

Figure 30: Flapper tip under water single-mode response.

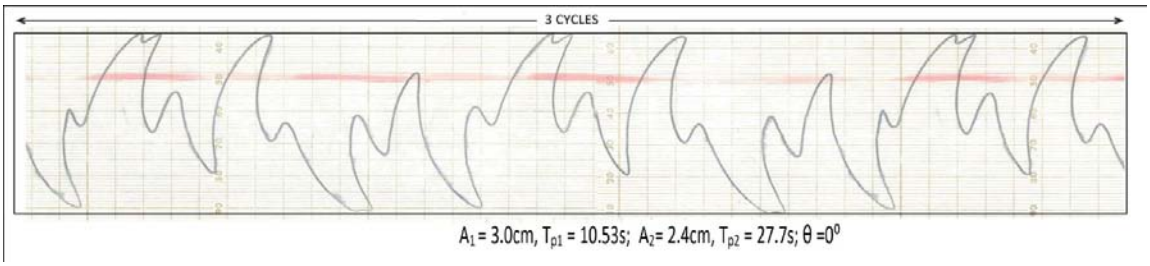

Figure 31: Flapper tip under water binary-mode response.

Measured amplitude for binary mode is accurate upto 96% while measured time-period is accurate by 90%. The difference in accuracy between parts §3.4.2 and §3.4.3 can be attributed to the vibration of the flow that is in contact with the flapper. This is supported by the dye and milk experiments in section §3.3.1 which exhibit free-stream turbulence.

3.5. Single mode experiments

3.5.1. Flow images – Structure visualization

Shown in Figure 32 is a collage of sample images of the instantaneous flow structures during the single mode experiments (1a)-(1g) performed with a temperature difference of about $\Delta T = 5^{o}$C between the two flow streams. These images were acquired using the Dye-visualization technique described in section §2.3. Experimental parameters for the same are specified in Table 1. Each photograph shows a region of about 16'' × 8'' of the channel, where the splitter plate is at the center of the vertical range. Right away, one can witness that the size of bubbles and spikes increases as we go further downstream from the splitter plate. As the amplitude of the single mode

increases from 0cm to 8cm as shown in Figure 32, Figure 33 and Figure 34, the size of the bubbles and spikes coming off the splitter plate increase proportionally. Symmetry among the bubbles and spikes with respect to the vertical axis is also a defining characteristic of single-mode perturbations with no shear between the top and bottom streams. Therefore, this characteristic is treated as the basis of eliminating shear within the flow. Before each set of experiments, a single-mode experiment is performed and the flow rates of the top and bottom streams of fluid are adjusted by controlling the valves (shown in Figure 4) such that the spikes and bubbles are vertical, and shear elimination is established. The experiment with no flapper motion was found to have large scale structures, which was unexpected. It was also observed from the images that experiments (1f) and (1g) do not reach saturation state, because the available channel length was insufficient. This was also observed in the previous work of Doron (2009) who used similar operating free-stream parameters.

(a) Experiment 1a

(b) Experiment 1b

(c) Experiment 1c

Figure 32: Single mode: (1a-1c) structures.

Images of the flow structures coming off the flapper using dye visualization are shown. Image 32a shows the structures with no-input flapper motion whereas figures 32b and 32c show flow structures corresponding to λ=2cm and λ=3cm.

(a) Experiment 1d

(b) Experiment 1e

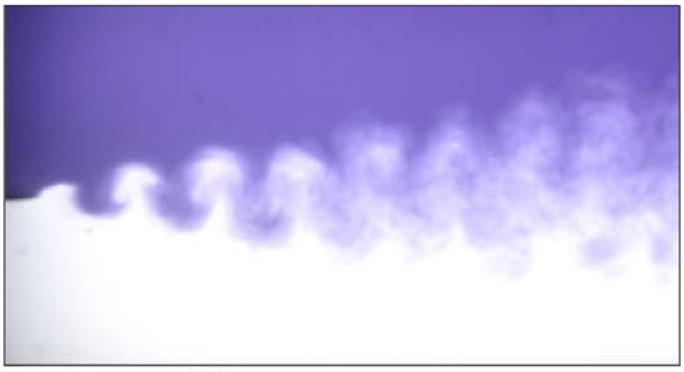

(c) Experiment 1f

Figure 33: Single mode: (1d-1f) structures.

Images of the flow structures coming off the flapper using dye visualization are shown. Image 33a, 33b and 33c show flow structures corresponding to λ=4cm, λ=5cm and λ=6cm respectively.

Figure 34: Single mode: (1g) structures.

Images of the flow structures coming off the flapper using dye visualization are shown. Image 34 shows flow structures corresponding to λ=8cm.

3.5.2. Growth rate calculations

Taylor's frozen turbulence hypothesis for fluid configurations with low turbulent intensities states that spatial correlations can be approximated by temporal correlations. It assumes that for a flow with free stream velocity (U_∞) much larger than the fluctuating components of velocity (u'), the advection contributed by turbulent intensity is small compared to the advection due to the free stream. Therefore, beyond a certain fixed point in space, advection due to a field of turbulence can be assumed to be due entirely to the free stream. Based on this hypothesis, ensemble averaged mixing data can be treated as equivalent to time-averaged data by substituting $t = x/U_\infty$. Therefore, in this present thesis, ensemble averaged mixing behavior is studied assuming low free stream turbulence.

For each experiment, 400 images of the test section were taken in order to generate reliable statistical information. The total mixing widths presented in this section are obtained by ensemble average of at least 200 images. Contour plots of average non-dimensionalized concentration gradient, f are given in Figure 35. The streamwise direction x and crosswise direction y were non-dimensionalized with the channel full-width, *H*. The non-dimensionalized concentration gradient is given by $f = \frac{(\rho - \rho_h)}{(\rho_c - \rho_h)}$. Maximum *f* of 1.0 occurs in the unmixed cold stream of the channel whereas minimum *f* of 0.0 occurs in the unmixed hot stream. Symmetry of the contours with respect to the splitter plate location can be observed from these contour plots. As the bubbles and spikes are symmetric for low Atwood number RTI experiments, this symmetry is in valid. Details of the image analysis technique are described in Appendix §E.1.

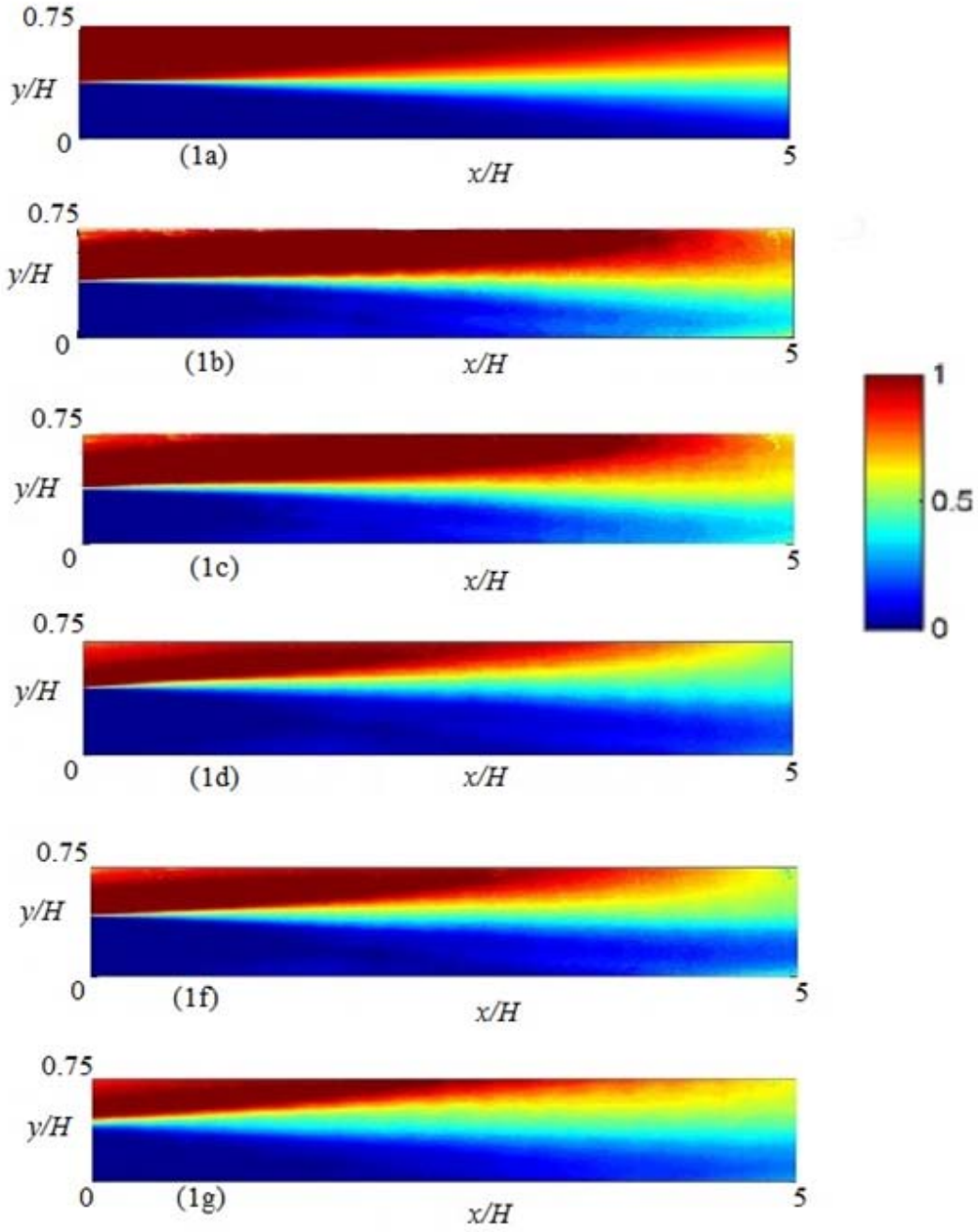

Figure 35: Single mode: Contour plots of ensemble averaged *f*.

Contour plots of non-dimensionalized density fraction *f* are plotted in the channel domain. Figure 35 shows the contours corresponding to experiments (1a-1g) as listed in Table 2 respectively.

As can be seen from the contour plots, the mixing width increases with single mode wavelength from λ=2cm to λ=8cm. The mixing width is over predicted for the case with no flapper motion. This is a deviation from the expected result. Total Mixing width defined by the width of the mixing region bound by the contours of f=0.9 at the top and f=0.1 at the bottom are calculated from the above contour plots in Figure 36. Plots of mixing widths for the same experiments are given in Figure 36. Both streamwise displacement x and mixing width, h have been non-dimensionalized with the channel full width, H.

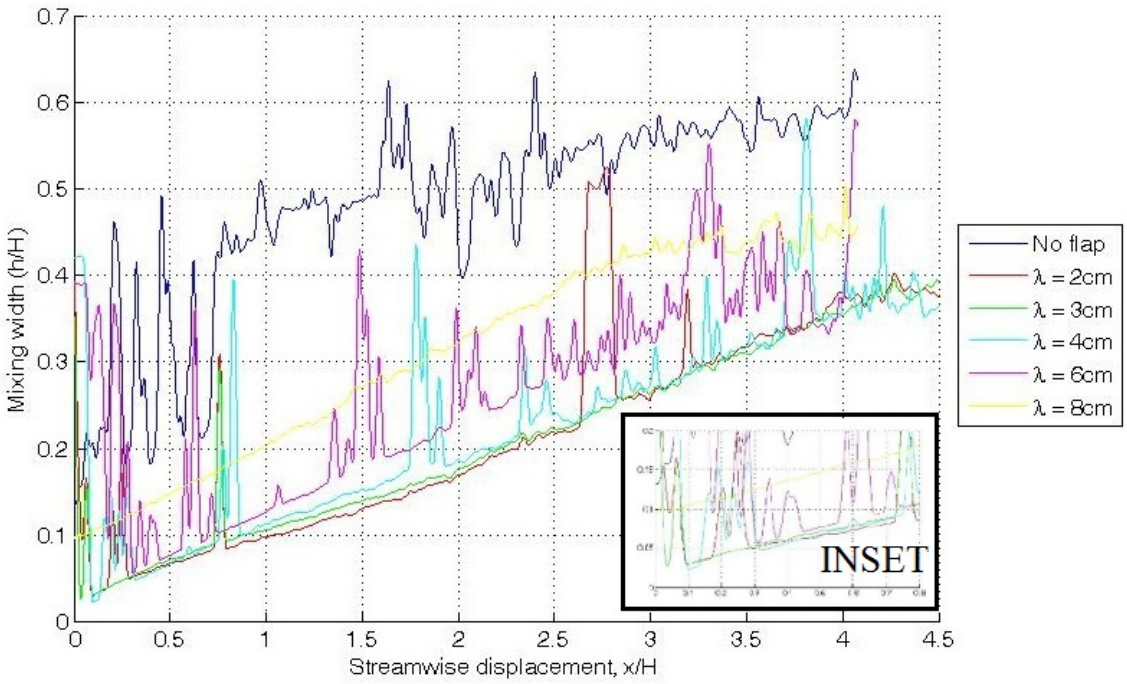

Figure 36: Single mode experiments: Mixing width data.

Analysis of each of the experimental cases is performed individually and ensemble averaging was completed for each image set. Because mixing width grows symmetrically for both bubbles and spikes at low Atwood numbers, only total mixing width is considered for all of the experimental analyses. Based on the previous experiments described in the literature, the total mixing width growth is least in the case of no initial perturbation. Total Mixing width growth rates are as predicted for the rest of the experiments, where mixing width increases with the increasing value of λ. Because of non-uniform backlighting, spikes are seen at certain points on the curves. Smoothing of each mixing width curve was performed by a moving averaging technique, where the width at each location is smoothed with 21 neighboring pixels so that sudden jumps in the width because of backlight non-uniformity can be minimized.

Growth rate analysis was performed on the mixing data for each experiment by using the Moving window method previously used by Banerjee et al. (2006). Here a window size of 200 pixels was used to average the saturation growth rate constant, α at each point. Mean values of α in the saturation zone are presented in Figure 37. These constants are used as base values for comparison in Binary and multi-mode experiments. As image data is not available for experiment (1e), α=0.059 was assumed according to the above observed trend.

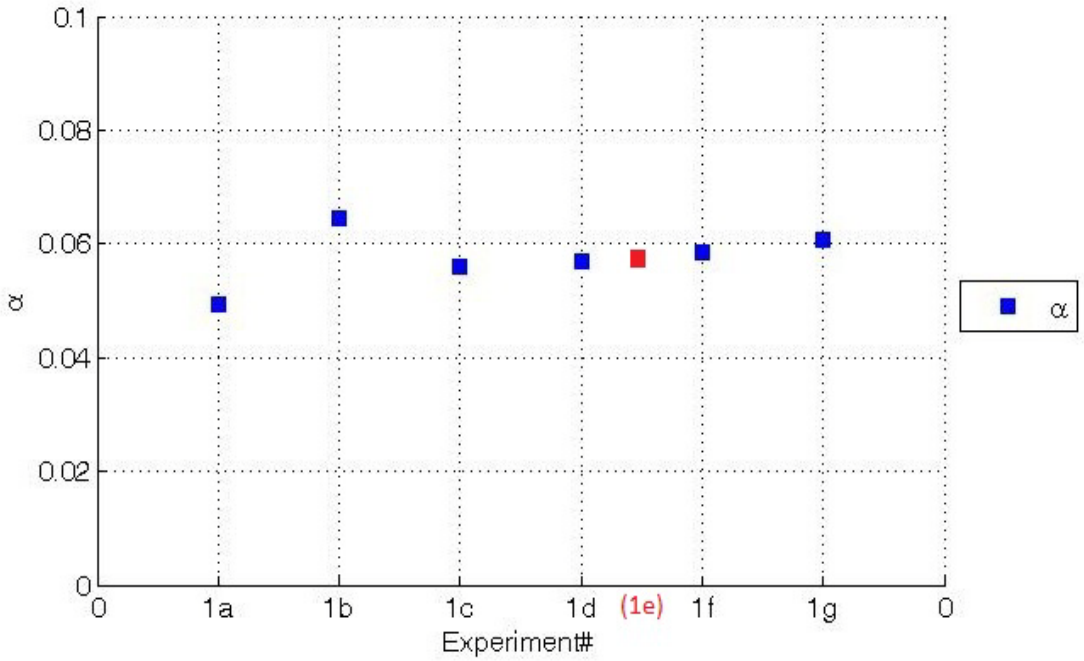

Figure 37: Single mode experiments: α values.

Variation of α is plotted for each single mode experiment is plotted against experiment#. Details of the experimental parameters are specified in Table 2.

3.6. Binary-mode experiments

3.6.1. Binary-mode experiments with varying phase-difference

3.6.1.1. Flow images – structure visualization

A similar approach as explained in section §3.5 was implemented for the Binary mode experiments as well. A similar dye-visualization technique is implemented for these experiments. The list of experimental parameters is given in Table 3. Shown in Figure 38, Figure 39 and Figure 40 are collages of the images of the instantaneous flow structures coming off the splitter plate for each of the binary mode experiments in a region of about 10’’x10’’ size that was photographed, with the splitter plate at the center

of vertical axis. In contrast to the single mode experiments, these flow structures exhibit the ‘leaning phenomenon’ because of the phase-difference between component modes of the binary mode. This phase shift in perturbation adds a small streamwise fluctuation u to the free stream velocity, U_∞ that results in the leaning of the bubbles and spikes by a certain angle, called ‘angle of lean’ measured with respect to the vertical axis. This leaning phenomenon is a defining characteristic of KHI experiments where shear between the two flow streams tend to lean the structures. A logical explanation of the variation of angle of lean in RTI experiments with the maximum velocity of the flapper tip during in the top and bottom sections is sought. The displacement, velocity and energy calculations were performed in section §3.1.2 so that the leaning phenomenon can be associated to the variation in θ. Another broader objective is to associate an equivalent KHI shear such that it produces the same amount of angle of lean as produced by a specific phase difference θ.

Secondary structures (bubbles and spikes) are generated at earlier stages of evolution in these experiments than compared to single mode experiments. The number of secondary structures and their orientation with respect to the primary structures is also being explored. Lastly, both these primary and secondary structures dissipate faster as compared to single mode experiments, as can be observed from the images. This could be attributed to various sources of error in the experiment as explained in section §4.2. An optimal location for the camera mount was decided so as to minimize the parallax error which causes smearing of the flow structures, but utilize the maximum available zoom without loss of resolution.

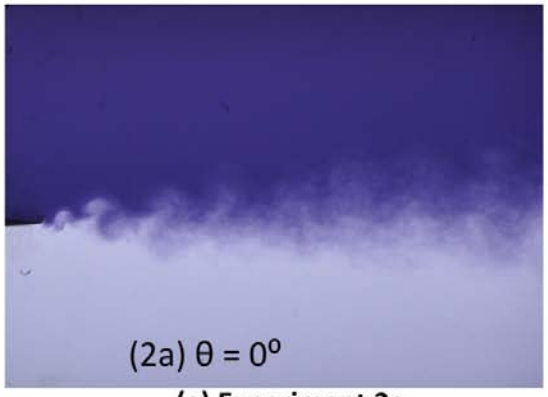

(a) Experiment 2a

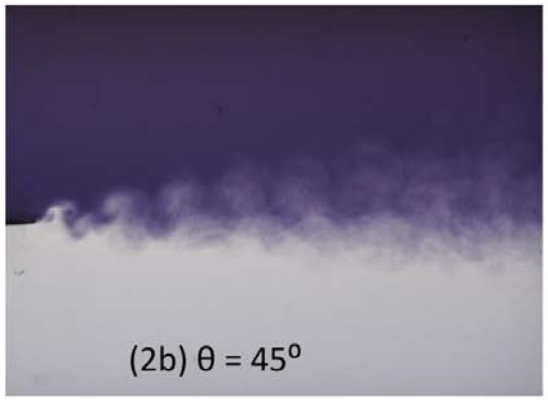

(b) Experiment 2b

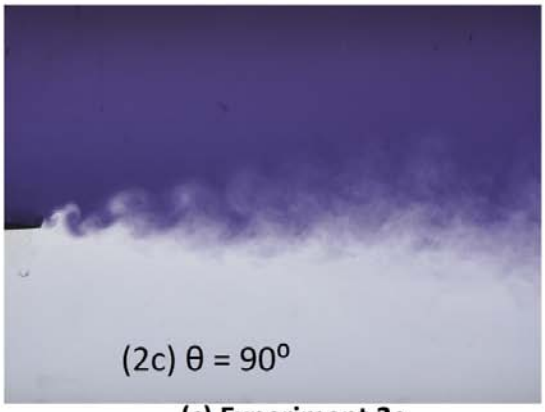

(c) Experiment 2c

Figure 38: Binary mode: (2a-2c) structures with θ.

Images of the flow structures coming off the flapper using dye visualization are shown. Image 38a, 38b and 38c show flow structures corresponding to λ_1=4cm, λ_2=2cm and varying θ respectively.

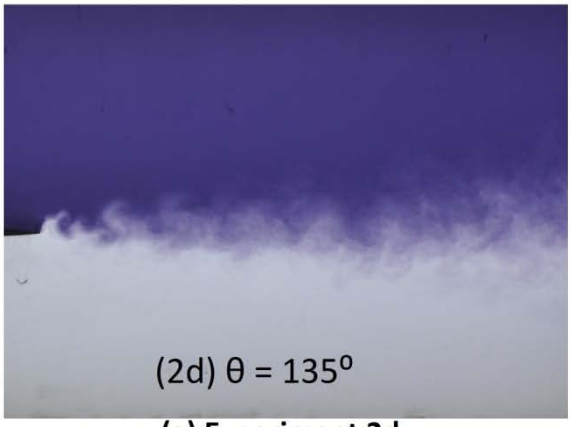

(a) Experiment 2d

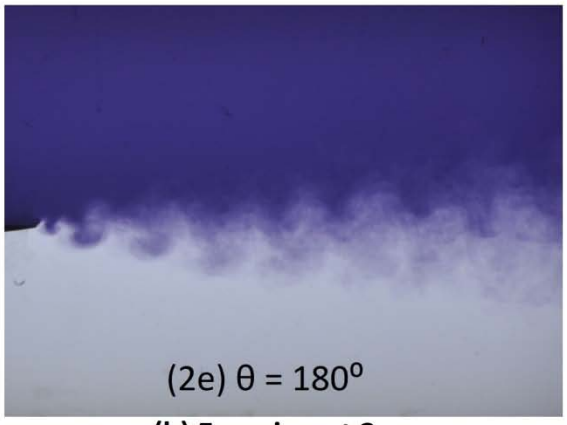

(b) Experiment 2e

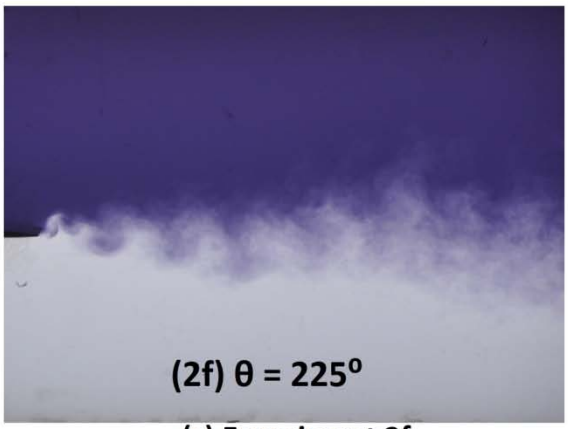

(c) Experiment 2f

Figure 39: Binary mode: (2d-2f) structures with θ.

Images of the flow structures coming off the flapper using dye visualization are shown. Image 39a, 39b and 39c show flow structures corresponding to λ_1=4cm, λ_2=2cm and varying θ respectively.

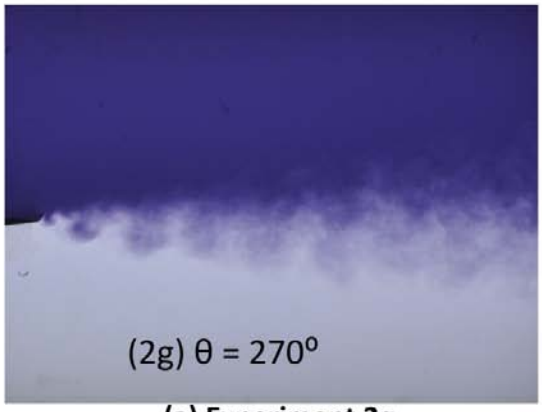

(a) Experiment 2g

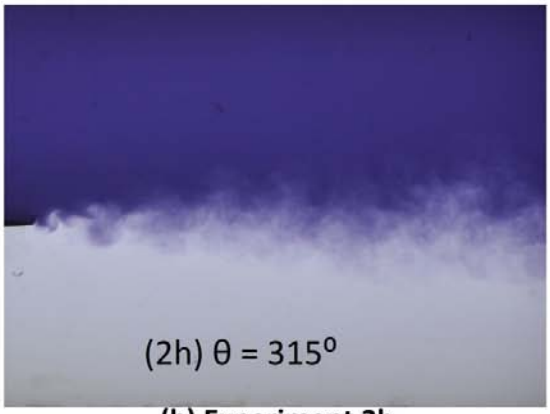

(b) Experiment 2h

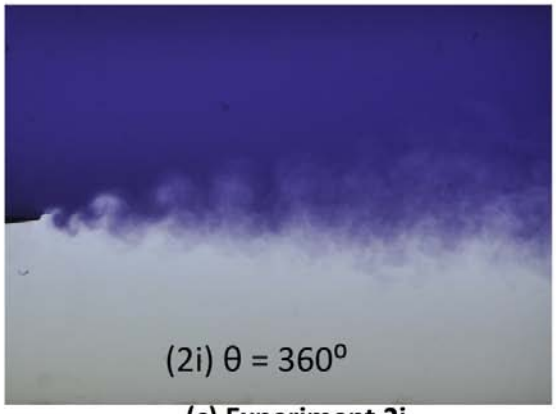

(c) Experiment 2i

Figure 40: Binary mode: (2g-2i) structures with θ.

Images of the flow structures coming off the flapper using dye visualization are shown. Image 40a, 40b and 40c show flow structures corresponding to λ_1=4cm, λ_2=2cm and varying θ respectively.

3.6.1.2. Growth rate calculations

A similar exercise was performed for the list of experiments (2a-2i) as single-mode experiments. Ensemble averaging as described in section §E.1 was performed for about 180 images for each experiment. Figure 41 and Figure 42 show the following contour plots of averaged non-dimensionalized concentration gradient, *f*. It is to be noted that the axis variables *x/H* and *y/H,* and limits of the contour plots are as described earlier. As compared to single-mode experiments, these contour plots exhibit lesser symmetry with respect to the splitter plate location. Even though binary mode perturbations produce leaning instantaneous structures that are non-symmetric about the vertical axis, ensemble averaging of sinusoidal perturbations would result in symmetry of the concentration contours for low Atwood numbers. Therefore, the observed loss of symmetry could be attributed to certain sources of error as explained in section §4.2.

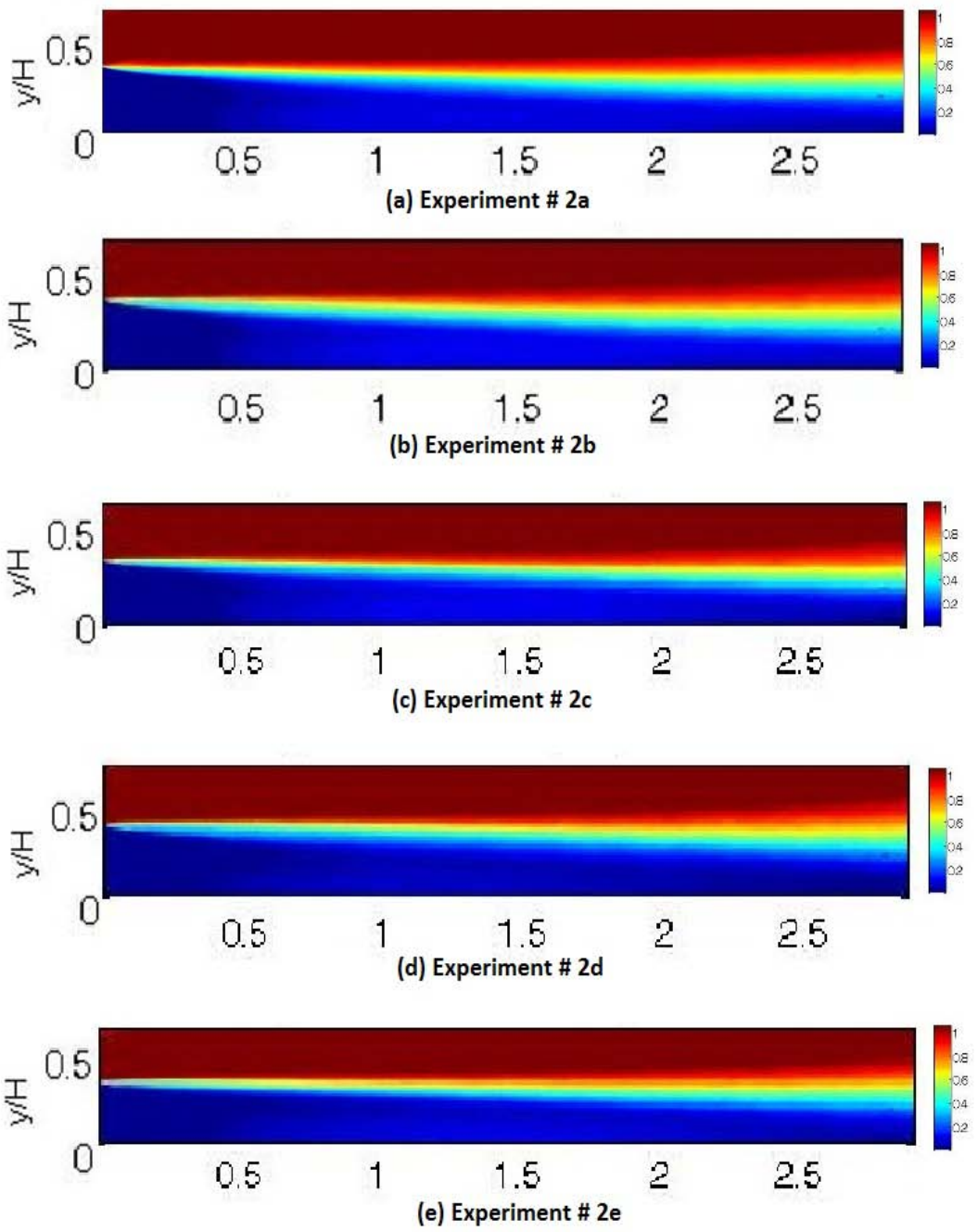

Figure 41: Binary mode: (2a-2e) contour plots of ensemble averaged *f* vs. θ.

Contour plots of non-dimensionalized density fraction *f* are plotted in the channel domain. Figure 41 shows the contours corresponding to experiments (2a-2e) as listed in Table 3 respectively.

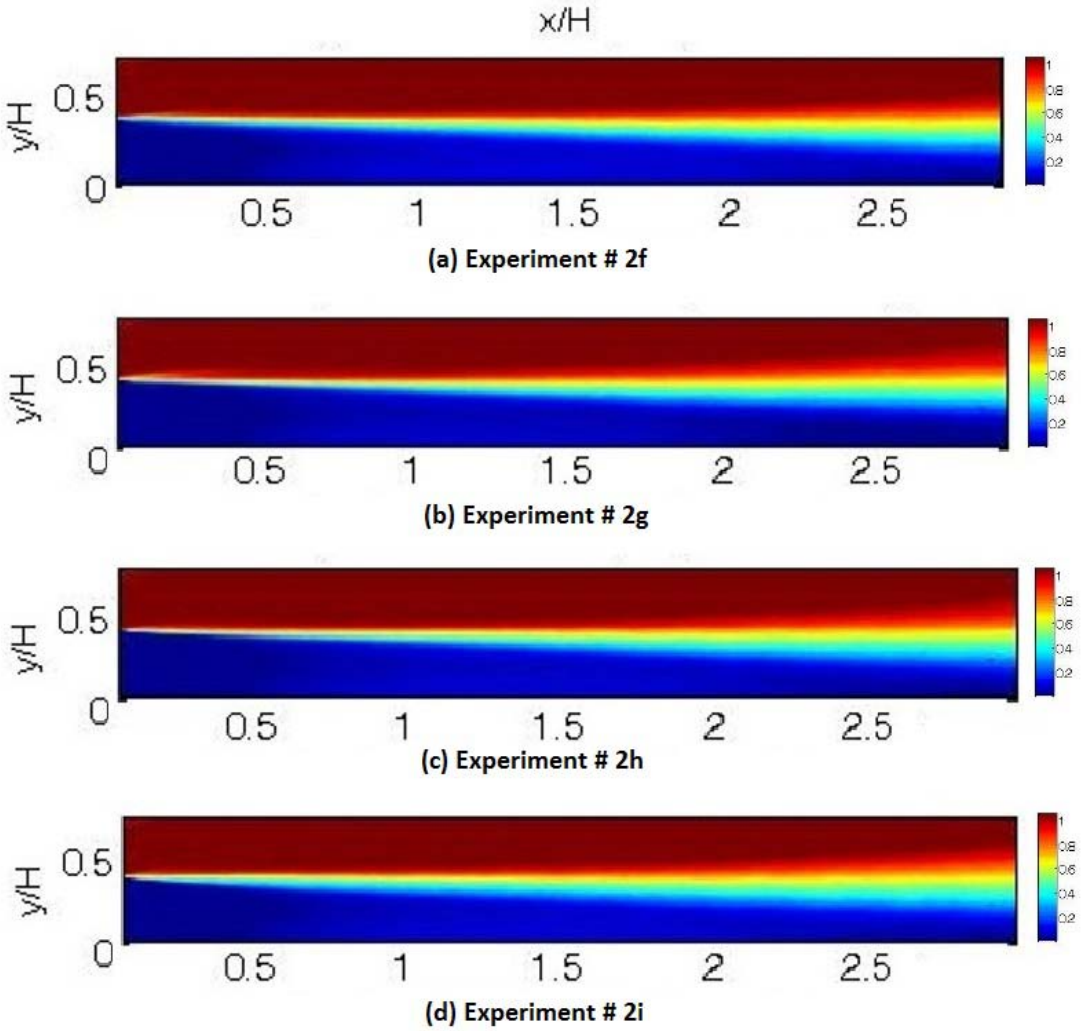

Figure 42: Binary mode: (2f-2i) contour plots of ensemble averaged *f* vs. θ.

Contour plots of non-dimensionalized density fraction *f* are plotted in the channel domain. Figure 42 shows the contours corresponding to experiments (2f-2i) as listed in Table 3 respectively.

Mixing width is calculated from the above contours for each experiment using the same criterion for *f*. Shown in Figure 43 are plots of mixing width of binary mode vs. component modes for phase-difference θ=0°, 45° and 90° respectively.

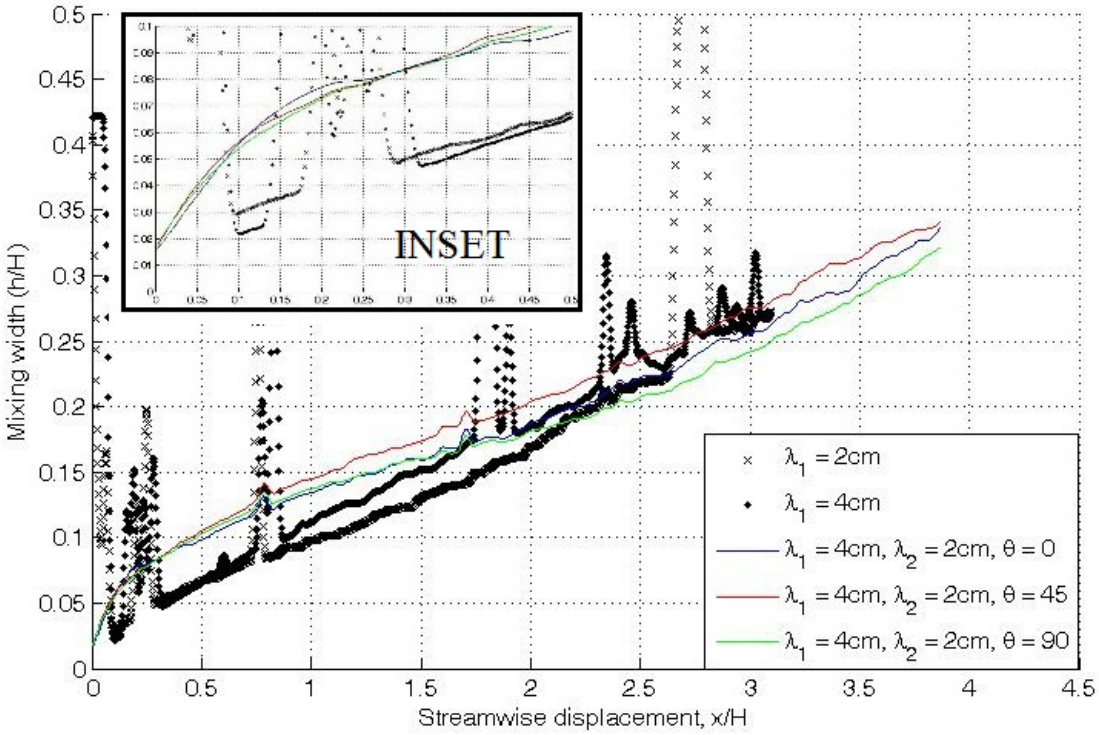

Figure 43: Binary mode: Binary vs. component mixing width *h.*

It can be clearly seen that binary mode mixing is higher in the earlier stages, i.e. exponential and non-linear stages but the saturation mixing widths are close to the larger wavelength, λ_1=4cm. This is because of bubble and spike competition and the larger wavelength emerges as the dominant wavelength. Also, this might explain the growth and dissipation of spikes and bubbles in the binary mode experiments as compared to single mode experiments. Another point to note is that mixing width curves of the single-mode data has larger amount of noise than binary mode experiments. This can be due to the improvement in imaging technique by the operator resulting in improved image quality as the experiments are performed over time.

Mixing width variation for all cases is shown below in Figure 44. As it can be seen from the graph, the binary mode mixing width grows at a similar rate for the linear stage of evolution irrespective of phase difference. Phase difference seems to affect the non-linear stages of evolution, and growth rates are dependent on θ. Once the growth rates reach saturation and bubbles and spikes attain terminal velocity, the growth rates are seemingly constant. From the figure, it can be concluded that the mixing widths are highest for the case of θ=45° or θ=135° and lowest for the cases of θ=90° or θ=270°.

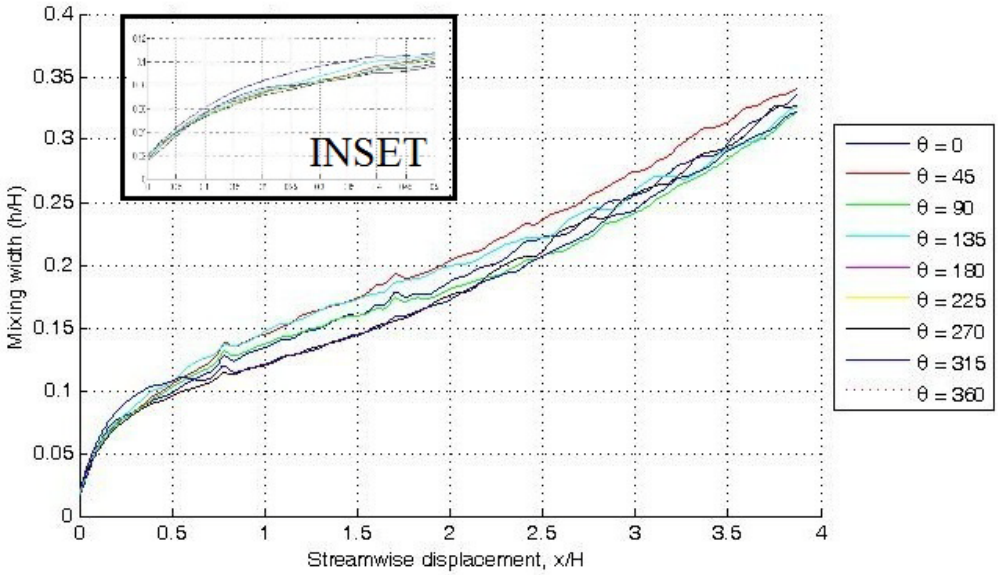

Figure 44: Binary mode: Mixing width vs. streamwise displacement (varying θ).

Quadratic saturation growth rate constant, α is plotted in Figure 45 for each experiment. Measured α values are higher than their corresponding single-mode growth rate constants except for θ=90° and θ=225°. This consistent trend is observed over all

sets of binary mode experiments during the current campaign, and perhaps can be related to initial energy deposition. Using the moving windows method for measuring α from ensemble averaging was observed to be sensitive to the size of window and background lighting. Accuracies of α measurement with respect to sources of error are further discussed in section §4.2.

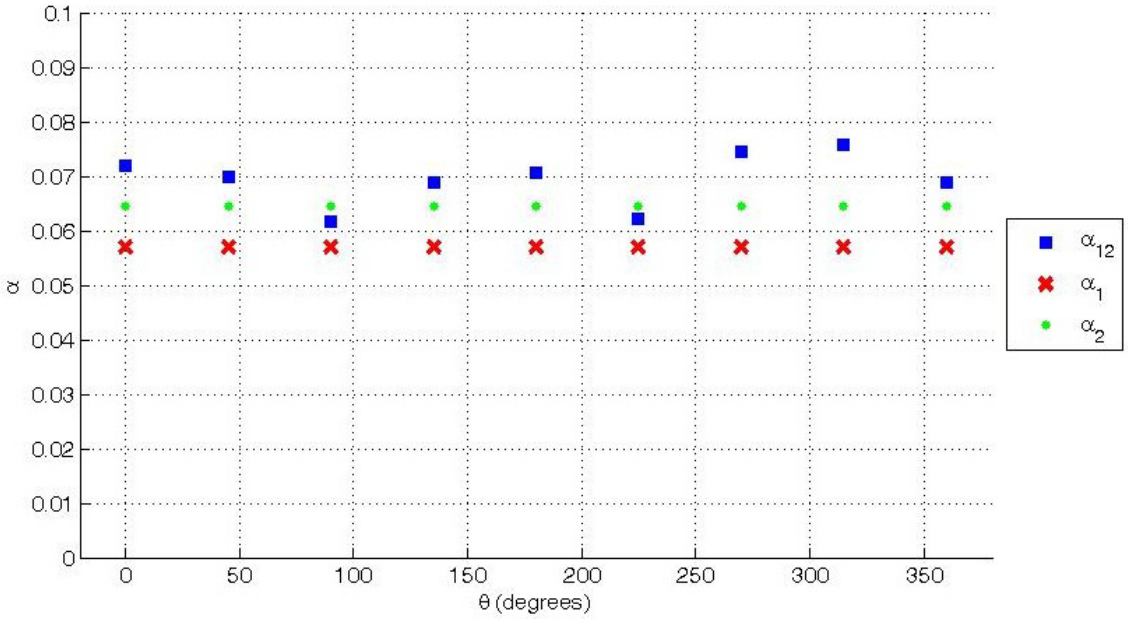

Figure 45: Binary mode: Growth rate constant α vs. θ.

Variation of α is plotted for each binary mode experiment with varying phase-difference. Details of the experimental parameters are specified in Table 3. Here α_{12} is the binary mode constant and α_1 and α_2 are the component saturation growth rate constants.

3.6.2. Binary mode experiments with amplitude variation

This section describes the experiments performed to observe the effect of magnitude of component wavelengths and ratio of component wavelengths of a binary mode initial

perturbation. A similar approach as explained in section §3.6.1 was implemented for the Binary mode experiments with amplitude variation as well. A similar dye-visualization technique is implemented for these experiments. Experimental parameters for this set of experiments are specified in Table 4.

3.6.2.1. Flow images – structure visualization

Shown in Figures 47-49 are collages of the images of the instantaneous flow structures coming off the splitter plate for each of the binary mode experiments in a region of about 10’’x10’’ size that was photographed, with the splitter plate at the center of vertical axis. The ‘leaning phenomenon’ as discussed earlier in section §3.6.1 is also observed here. As with the experiment set (2a-2i), primary and secondary structures are observed for this set of experiments (3a-3j), and were found to dissipate at quicker rate than compared to single mode experiments. This could be attributed to various sources of error in the experiment as explained in section §4.2.

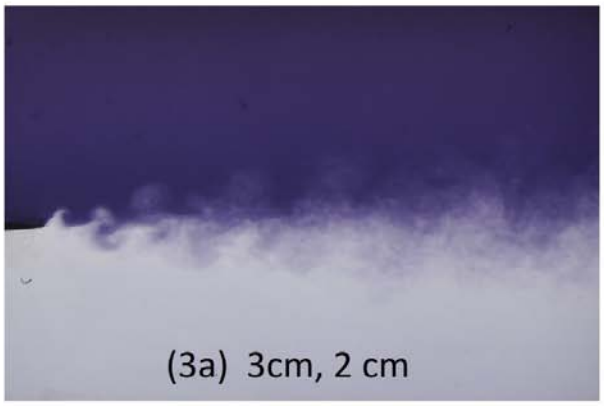

(a) Experiment # 3a

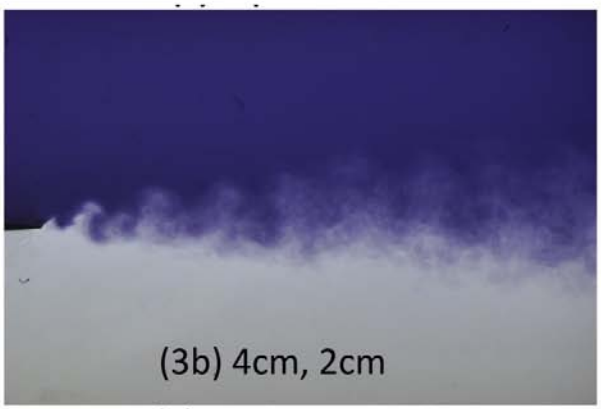

(b) Experiment # 3b

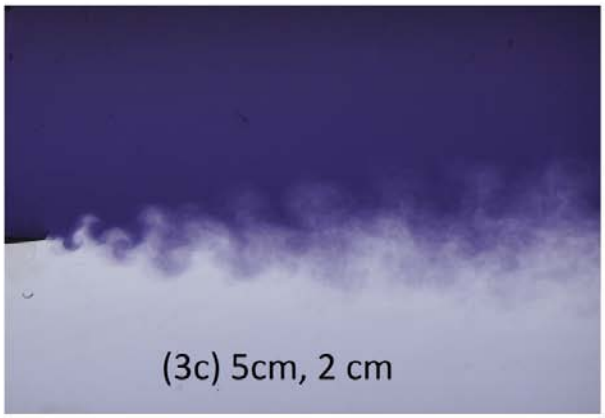

(c) Experiment # 3c

Figure 46: Binary mode: (3a-3c) structures with λ_i.

Images of the flow structures coming off the flapper using dye visualization are shown. Image 46a, 46b and 46c show flow structures corresponding to λ_2=2cm, λ_1=3, 4, 5cm and θ=45° respectively corresponding to experiments# (3a-3c).

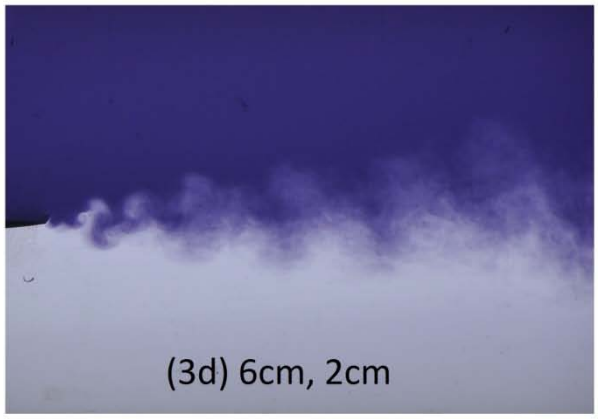

(a) Experiment # 3d

(b) Experiment # 3e

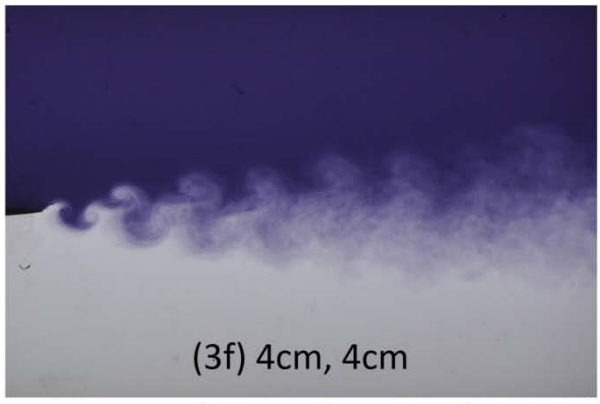

(c) Experiment # 3f

Figure 47: Binary mode: (3d-3f) structures with λ_i.

Images of the flow structures coming off the flapper using dye visualization are shown. Image 47a, 47b and 47c show flow structures corresponding to (λ_1, λ_2) = (6, 2), (8, 2) and (4, 4) cm, and θ=45^{o} respectively. These correspond to experiments# (3d-3f).

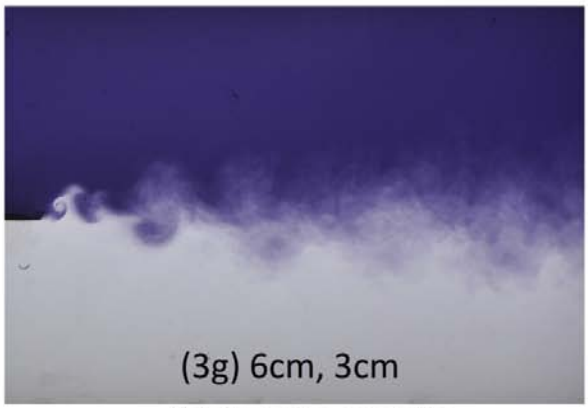

(a) Experiment # 3g

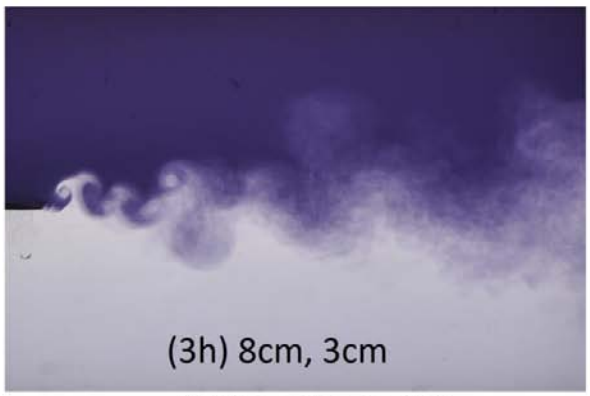

(b) Experiment # 3h

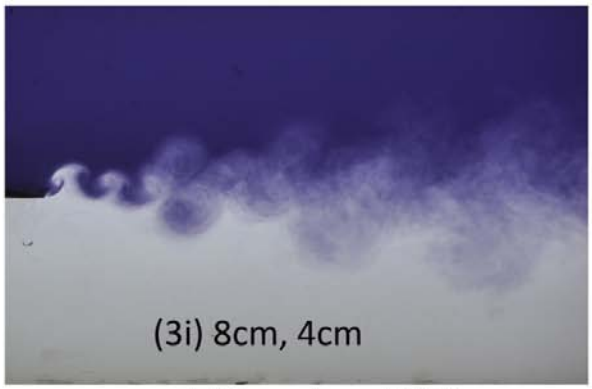

(c) Experiment # 3i

Figure 48: Binary mode: (3g-3i) structures with λ_i.

Images of the flow structures coming off the flapper using dye visualization are shown. Image 48a, 48b and 48c show flow structures corresponding to (λ_1, λ_2) = (6, 3), (8, 3) and (8, 4) cm, and θ=45° respectively. These correspond to experiments# (3g-3i).

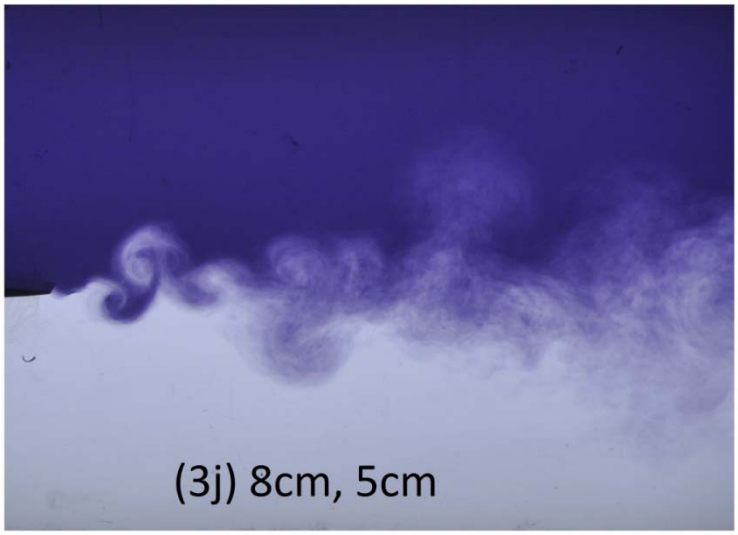

Figure 49: Binary mode: (3j) structures with λ_i.

Image of the flow structure coming off the flapper using dye visualization is shown. Image 49 shows flow structures corresponding to (λ_1, λ_2) = (8, 5) and θ=45°. This corresponds to experiment# (3j).

From the above images, it could be observed that the shape of structures is similar for experiments (3a-3e), i.e. the number of secondary structures, and the relative inclination between adjacent bubbles and spikes is similar. This is because only λ_1 was varied for this set of experiments, whereas λ_2 and θ were kept constant. As λ_1 was increased, the size of the longest bubble and spike also increased accordingly. Experiment (3f) was a special case of λ_1=λ_2. One could witness the symmetry of the structures from the image. It can also be observed that flow structures take longer time for dissipation into the ambient as compared to the rest of the experiments.

From images of experiments (3b), (3g) and (3i), effect of the magnitude of the component wavelengths on the shape of the structures can be witnessed. As can be seen

from the waveforms in Figure 15 for these experiments, (3g) and (3i) have a similar shape and therefore, similar fluid structures, whereas (3b) has a different waveform. Lastly, effect of λ_2 can be seen from the images of cases (3e) and (3h-3j), which are all very similar because of similar waveforms.

3.6.2.2. Growth rate calculations

A similar exercise was performed for the list of experiments (3a-3j) as experiments (2a-2i). Ensemble averaging as described in section §E.1 was performed for about 180 images for each experiment. Figure 50 and Figure 51 show the contour plots of averaged non-dimensionalized concentration gradient, *f*. It is to be noted that the axis variables *x/H* and *y/H*, and limits of the contour plots are as described earlier.

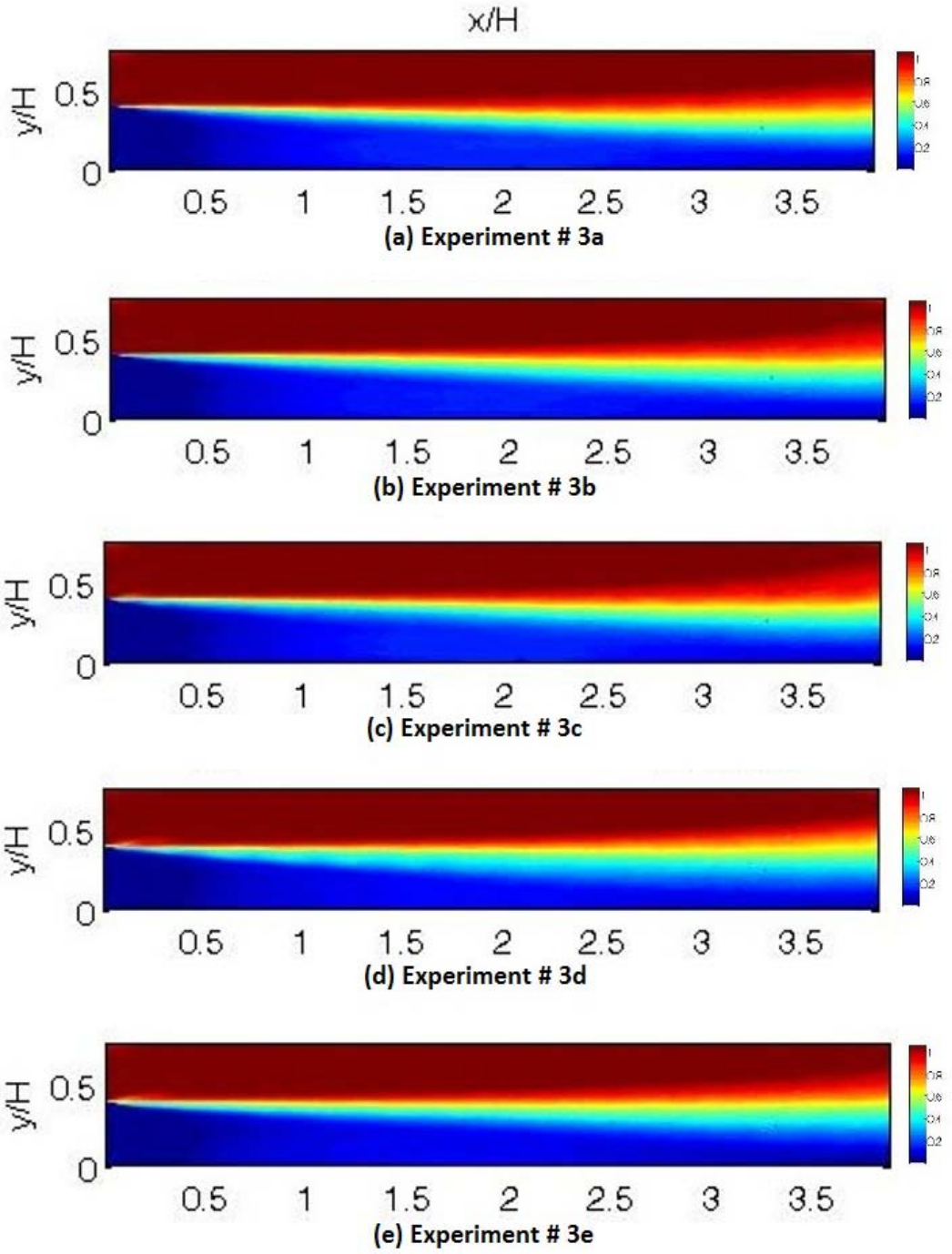

Figure 50: Binary mode: (3a-3e) contour plots of ensemble averaged f (with λ_i).

Contour plots of non-dimensionalized density fraction f are plotted in the channel domain. Figure 50 shows the contours corresponding to experiments (3a-3e) as listed in Table 4 respectively.

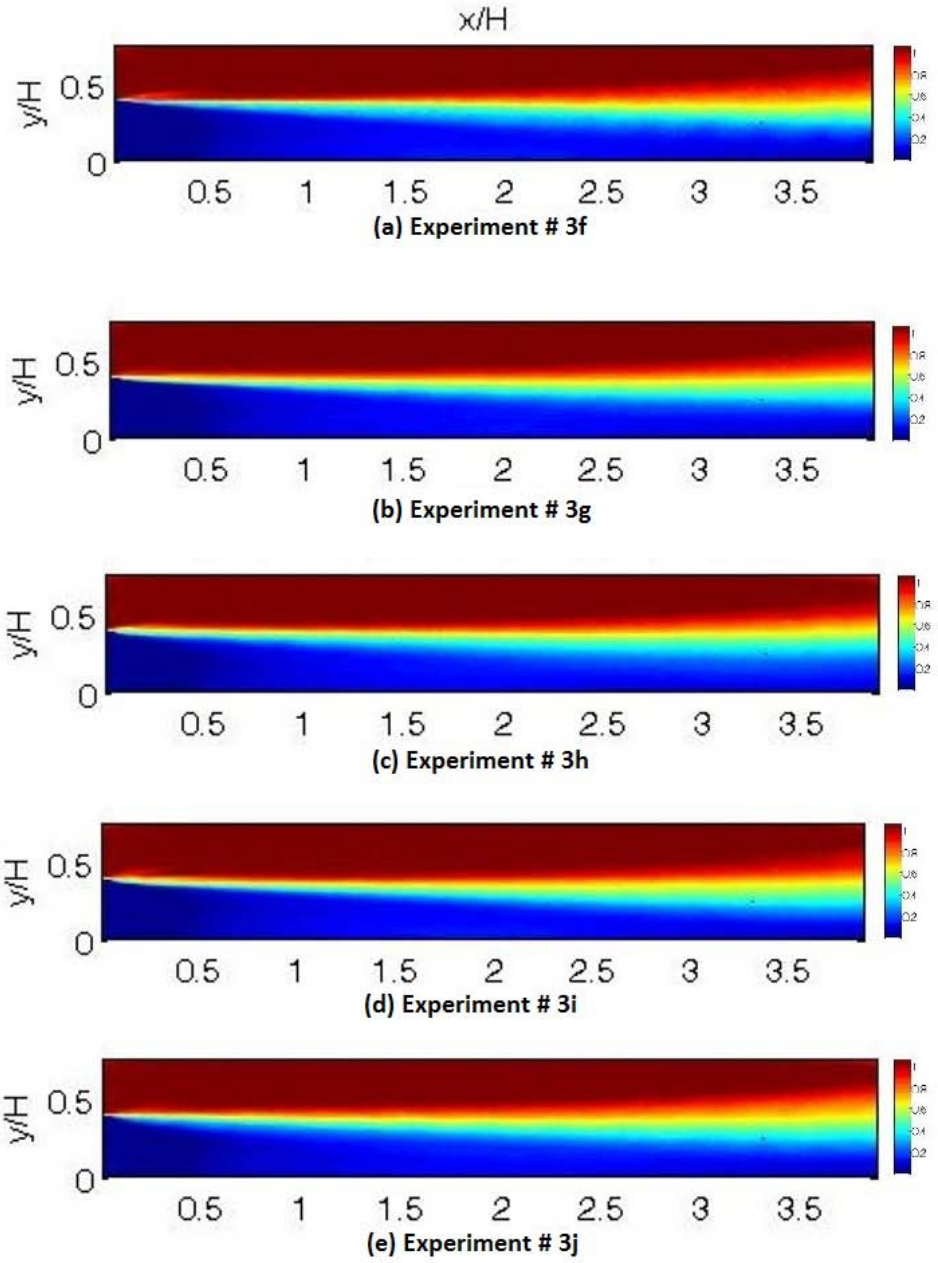

Figure 51: Binary mode: (3f-3j) contour plots of ensemble averaged f (with λ_i).

Contour plots of non-dimensionalized density fraction f are plotted in the channel domain. Figure 51 shows the contours corresponding to experiments (3f-3j) as listed in Table 4 respectively.

Shown below in Figure 52 is the variation of mixing widths with λ_1 for experiments (3a-3e). In the earlier regimes of RTI, the mixing width grows proportional to λ_1 but in the later stages λ_1=6cm has a higher mixing width. This can be explained using Mode coupling in the non-linear regime, which might cause suppression or expression of the growth rate.

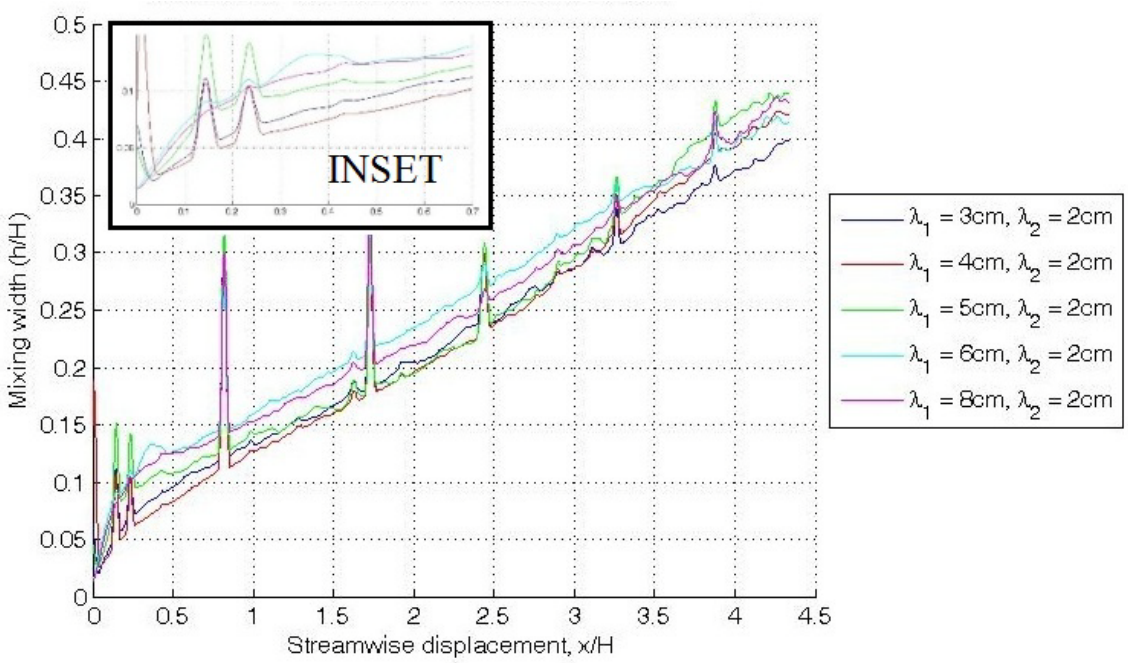

Figure 52: Binary mode: (3a-3e) mixing width variation with λ_1 with constant λ_2.

Mixing width variation with streamwise distance is plotted for experiments# (3a-3e) to observe the effect of variation in width due to increasing λ_1. λ_2=2cm was kept constant.

Figure 53 shows the plots of α for the same set of experiments. Measured α values are higher than the component αs. As α_1 increases, α_{12} was found to decrease with α_2 kept constant.

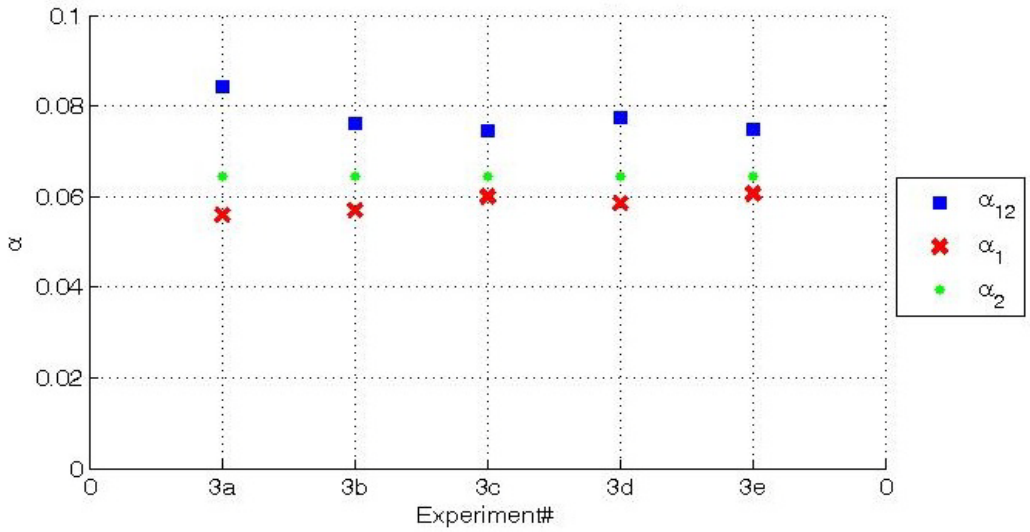

Figure 53: Binary mode: (3a-3e) α variation with λ_1 with constant λ_2.

Details of the experimental parameters are specified in Table 4. Here α_{12} is the binary mode constant and α_1 and α_2 are the component saturation growth rate constants. Conditions (λ_1, λ_2) for these experiments are (4, 2), (6, 3) and (8, 4) cm respectively, with θ=45°. Ratio of λ_1/λ_2 was kept constant.

Presented in Figure 54 are the mixing widths vs. *x/H* to observe the effect of the magnitude of wavelength $|\lambda_i|$. In consistency with the earlier observed experiments in this present campaign, growth of the binary mode occurs proportionally to $|\lambda_i|$ in the earlier regimes of RTI evolution, but in the early saturation regime, the mixing widths all collapse independent of $|\lambda_i|$. This is an interesting development which means that at saturation, for θ=45° and λ_1/λ_2 = 2.0, RTI induced mixing is independent of the

magnitude of the component waves. Variation of binary mode saturation growth rate constant α_{12} is shown in Figure 55. α_{12} is varies almost linearly with increasing magnitude of the component wavelengths. The definition of saturation deems that α_{12} be similar independent of $|\lambda_i|$ but the observed discrepancy can be attributed to sources of error discussed in section §4.2.

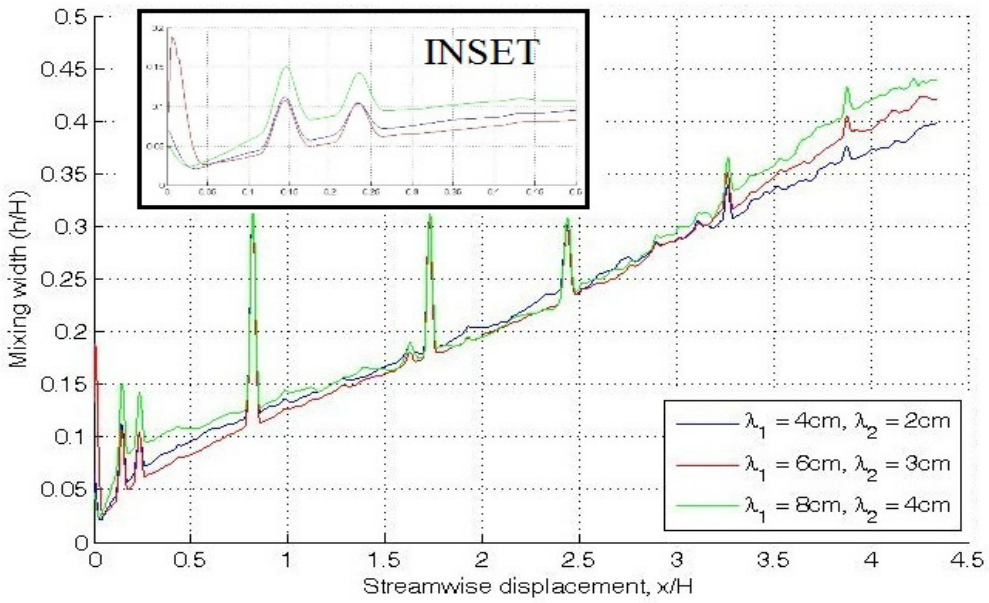

Figure 54: Binary mode: (3b, 3g, 3i) mixing width vs. $|\lambda_i|$ with a constant $\lambda_1/\lambda_2 = 2.0$.

Variation of mixing width with streamwise distance is plotted to observe the effect of magnitude of amplitude. $|\lambda|$.

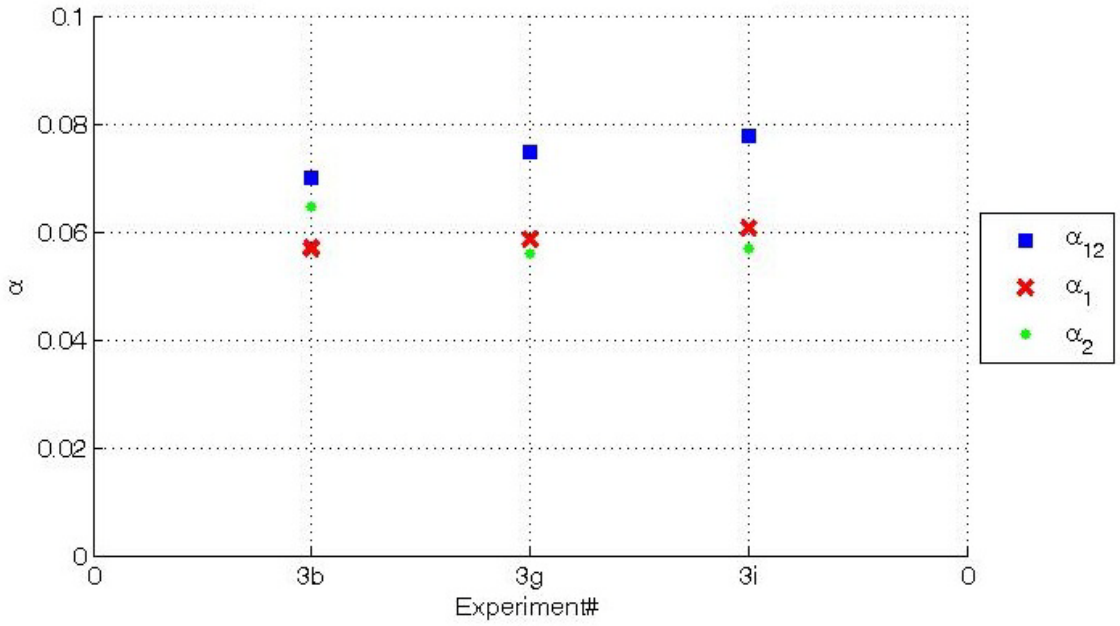

Figure 55: Binary mode experiments: α vs. $|A_i|$. Given $\lambda_1/\lambda_2 = 2.0$. From the left to the right, magnitude of λ_1 increases linearly.

Similarly, mixing widths of cases (3e), (3h-3j) are plotted in Figure 56 to observe the effect of λ_2. In consistency with the earlier binary mode experiments, the mixing width grows proportional to λ_2 in the earlier stages and then saturates. In the saturation regime, maximum mixing width occurs for λ_2=3cm, whereas minimum mixing width corresponds to λ_2=4cm.

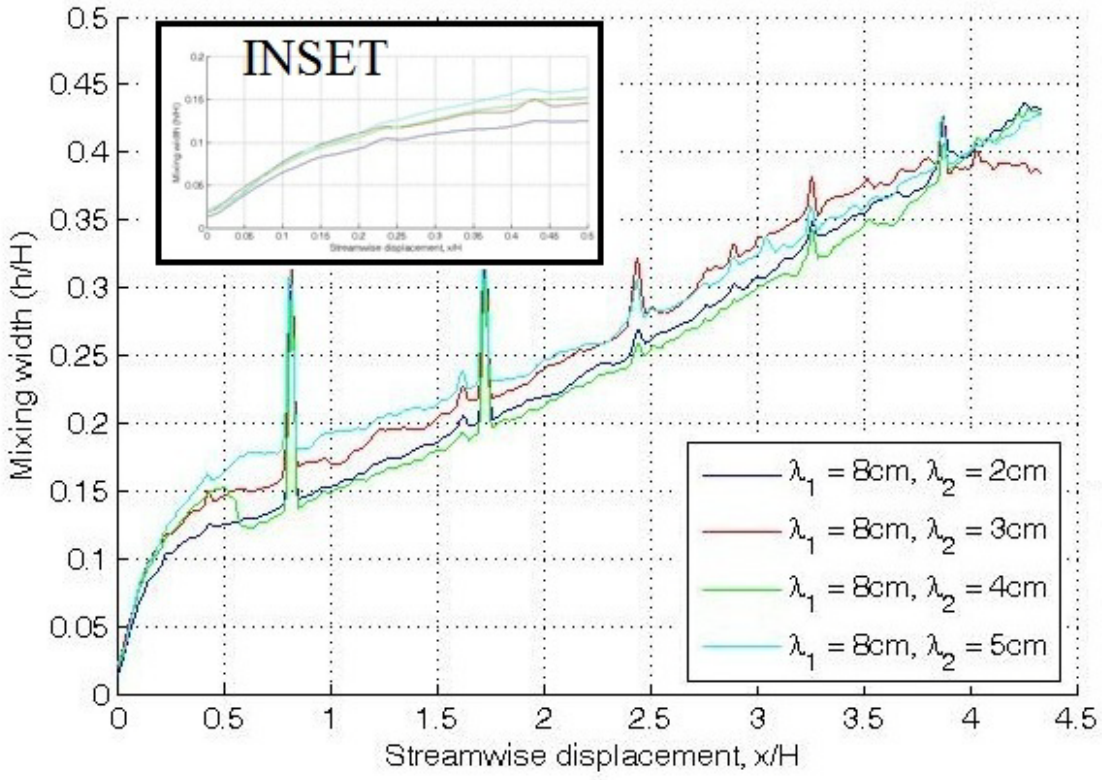

Figure 56: Binary mode: (3e, 3h-3j) mixing width vs. λ_2.

Variation of mixing width with streamwise displacement is plotted for experiments (3e, 3h-3j) with λ_2= 2, 3, 4, 5cm respectively and λ_1=8cm kept constant.

Variation of α for the same set of experiments is presented in Figure 57. It can be observed from the figure that α_{12} decreases with increasing α_2 with α_1 kept constant. Also, overall values of α_{12} are higher than the component α values.

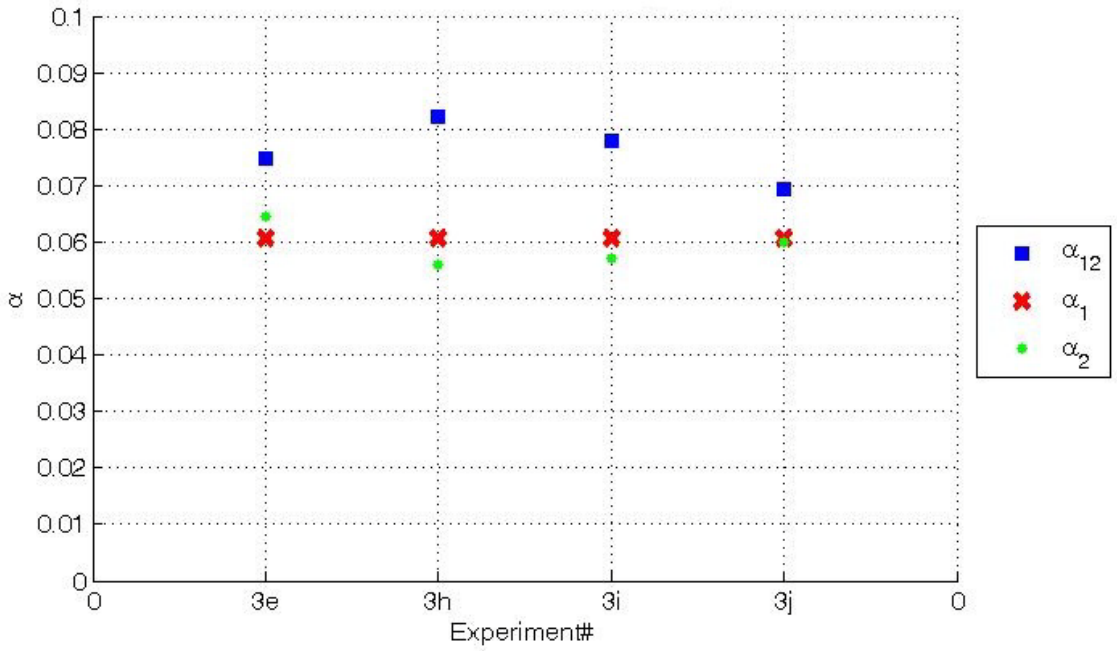

Figure 57: Binary mode: (3e, 3h-3j) α vs. λ_2.

Details of the experimental parameters are specified in Table 4. Here α_{12} is the binary mode constant and α_1 and α_2 are the component saturation growth rate constants. Conditions λ_2 = 2, 3, 4, 5cm respectively, with λ_1 =8cm and θ=45°.

3.7. Multi-mode experiments

This section describes the experiments performed to observe the first ever experiments with a multi-modal (3 or more modes) initial perturbation at the fluid interface. A similar approach as explained in section Binary-mode experiments with varying phase-difference was implemented for these Multi mode experiments. A similar dye-visualization technique is implemented for these experiments. Experimental parameters for this set of experiments are specified in Table 7. It was observed during the experiments that the RMS error of the servo motor signal were higher than those

observed in the previous sets of experiments. This might be due to the higher required speed of servo motor. Thus, it was observed that high-frequency noise was present in the system, causing earlier small scale structures and quicker viscous dissipation.

3.7.1. Flow images – structure visualization

Collages of the flow structures coming off the flapper are presented in Figure 58 and Figure 59. A region of 10’’×15’’ was photographed for the set of experiments (4a-4e). Blurriness of the images could be due to boundary layer effects and other sources of error discussed in section §Sources of error. Also, difficulties with proper backlight were encountered while performing experiments (4c-4e). Large Scaled structures can be observed in the images, and small scaled structures are generated earlier than in binary mode experiments. Each of these experiments constitutes a large wavelength of 8cm and a short wavelength of 2cm such that the effect of small wavelength on the larger wavelength can be understood. Particular trends in the shapes cannot be discerned because of the lack of a distinctive visible interface.

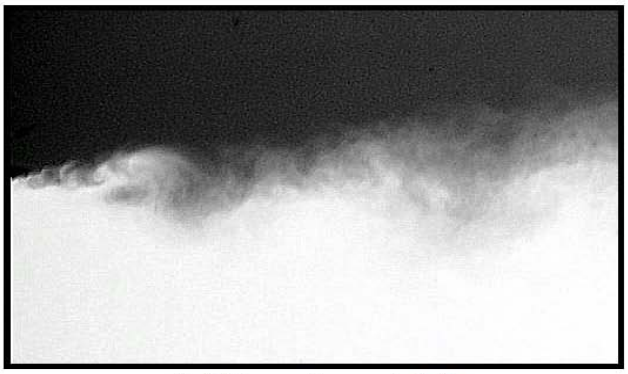

(a) Experiment # 4a

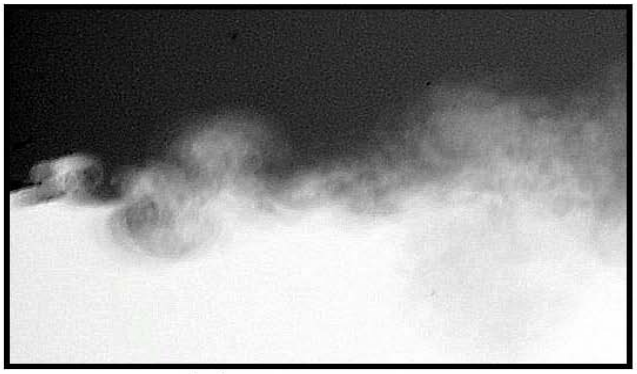

(b) Experiment # 4b

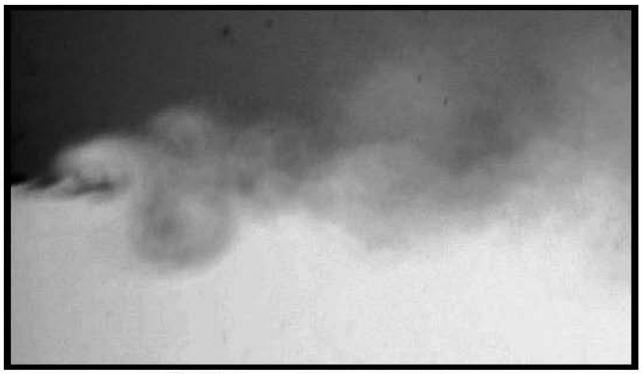

(c) Experiment # 4c

Figure 58: Multi-mode: (4a-4c) structures.

Images of the flow structures coming off the flapper using dye visualization are shown. Image 58a, 58b and 58c show flow structures corresponding to ($\lambda_1, \lambda_2, \lambda_3$) = (8, 4, 2), (8, 5, 2) and (8, 6, 2) cm, and (θ_1, θ_2) = (45°, 90°) respectively. This corresponds to experiments# (4a-4c).

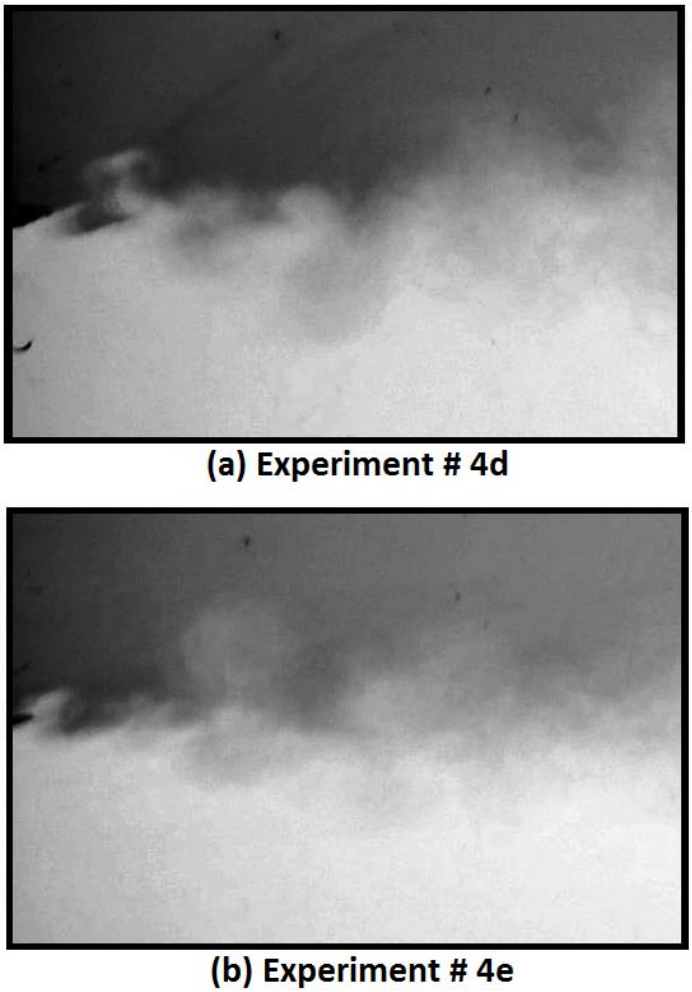

(a) Experiment # 4d

(b) Experiment # 4e

Figure 59: Multi-mode: (4d-4e) structures.

Images of the flow structures coming off the flapper using dye visualization are shown. Image 59a, and 59b show flow structures corresponding to ($\lambda_1, \lambda_2, \lambda_3, \lambda_4$) = (8, 6, 3, 2) and (8, 6, 4, 2) cm, and ($\theta_1, \theta_2, \theta_3$) = (45°, 90°, 135°) respectively. This corresponds to experiments# (4d-4e).

3.7.2. Growth rate analysis

A similar exercise was performed for the list of experiments (4a-4e) as experiments (2a-2i). Ensemble averaging as described in section §E.1 was performed for

about 180 images for each experiment. Figure 60 shows the contour plots of averaged non-dimensionalized concentration gradient, *f*. It is to be noted that the axis variables *x/H* and *y/H*, and limits of the contour plots are as described earlier. Plots of mixing width contours were not plotted for experiments (4c-4e) because of difficulties with background lighting and dye concentration.

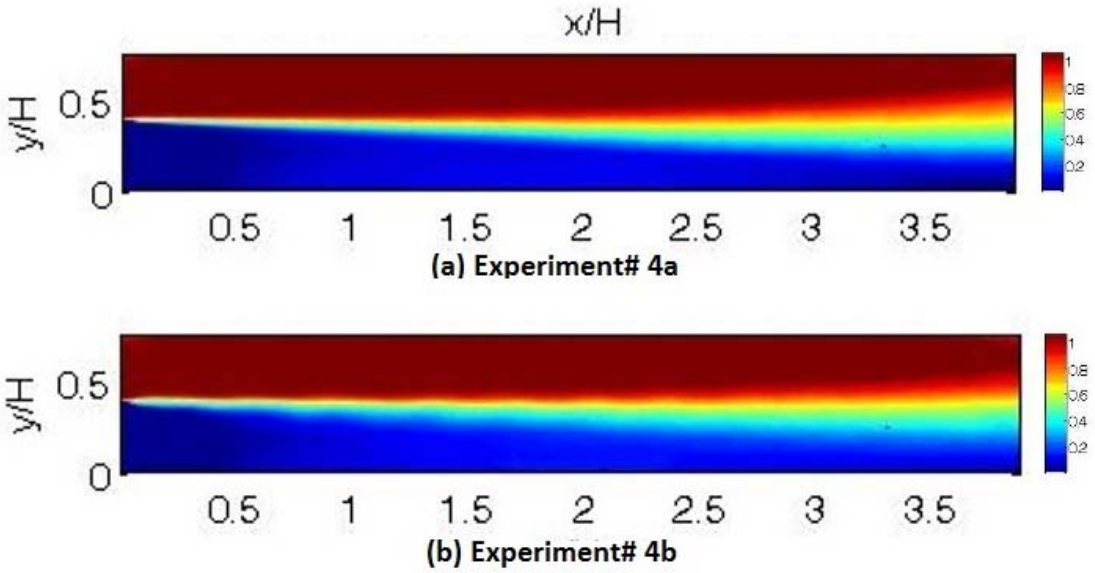

Figure 60: Multi-mode: (4a-4b) contour plots of averaged *f*.

Contour plots of non-dimensionalized density fraction *f* are plotted in the channel domain. Figures 60a-60b show the contours corresponding to experiments (4a-4b).

Mixing width variation for experiments (4a-4b) is presented in Figure 61. They exhibit a similar trend in variation, with higher growth rates for experiment (4b) as compared to (4a). It is to be noted that while (4a) and (4b) have the same λ_1, λ_3, θ_1 and

θ_2, λ_2 is greater for (4b) compared to (4a). Mixing width seems to be not affected by mode coupling and grows in accordance with λ_2.

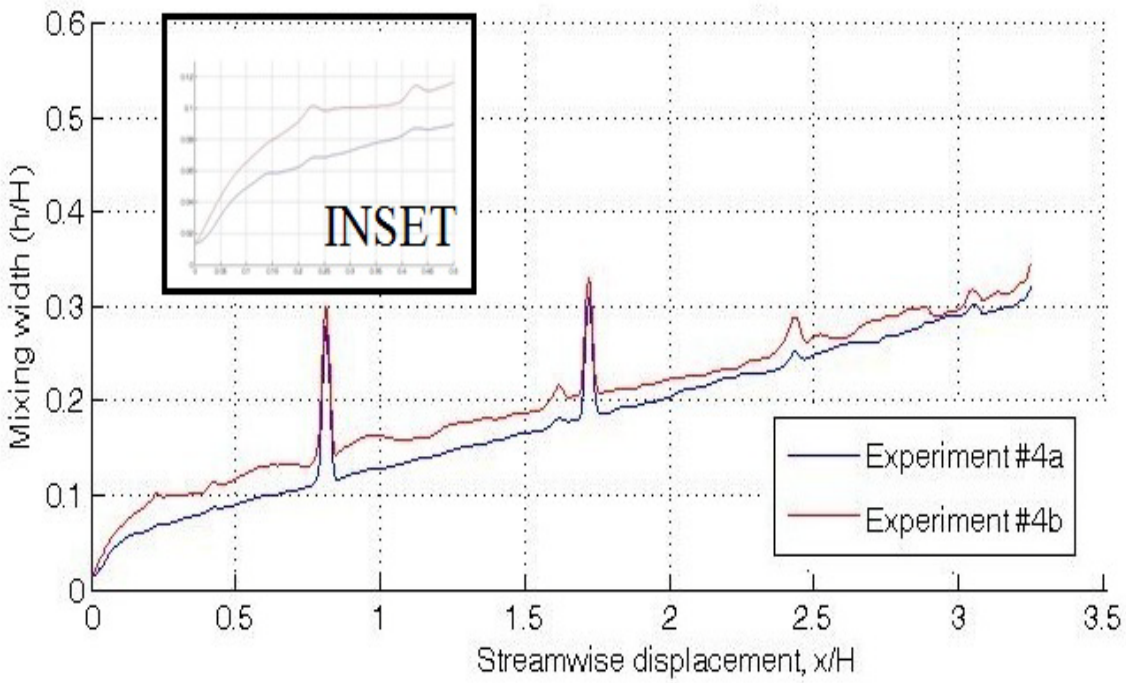

Figure 61: Multi-mode: Mixing width vs. experiment#.

Variation of mixing width with streamwise displacement is plotted for experiments (4a-4b) with ($\lambda_1, \lambda_2, \lambda_3$) = (8, 4, 2) and (8, 5, 2) cm, and (θ_1, θ_2) = (45°, 90°) respectively.

Presented in Figure 62 is a comparison of multi-mode mixing width with component modes. As can be clearly observed, multi-mode mixing width decreases compared to the largest wavelength of λ_1=8cm and increases in comparison with the other 2 modes of λ_2=4cm and λ_3=2cm. Therefore, addition of more modes to the largest wavelength single mode seems to mitigate its growth, but growth of the smaller wavelengths is increased by the addition the largest wavelength.

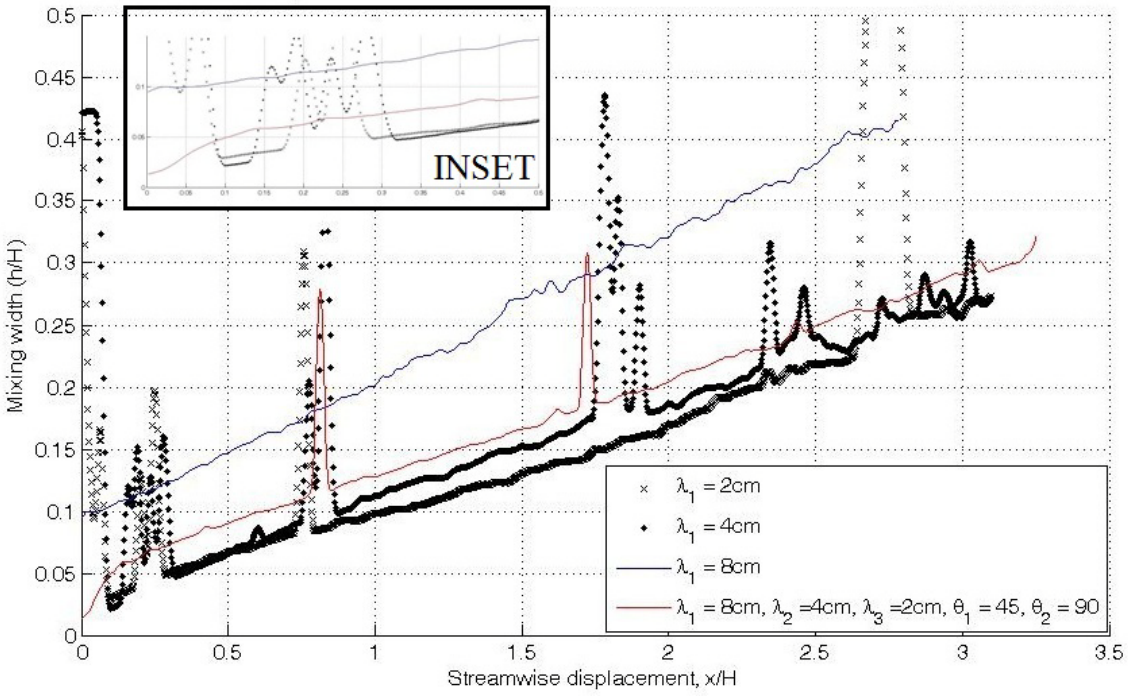

Figure 62: Multi-mode: Multi-mode vs. component mixing width.

Variation of multi-mode mixing width with streamwise displacement is plotted for comparison with component single mode mixing widths.

Lastly, variation of multi mode saturation growth rate constant, α_m is plotted against component α_i for each experiment in Figure 63. It can be observed that α_m decreases with λ_2 for tri-modal experiments with constant λ_1, λ_3, θ_1 and θ_2. For experiments with initial conditions with 4 component modes, such as experiment (4d), multi-modal growth rate α_m decreases compared to tri-modal experiments. This phenomenon is dependent upon several factors like the involved parameters like phase-differences, θ_i, wavelengths, λ_i and is therefore complicated to understand. Given the uncertainties in measurement of α_m, more number of experiments must to be performed such that the contribution of these parameters towards saturation growth rates can be

established. Also, mixing width data is required to support the above observations such that a generalized theory can be obtained.

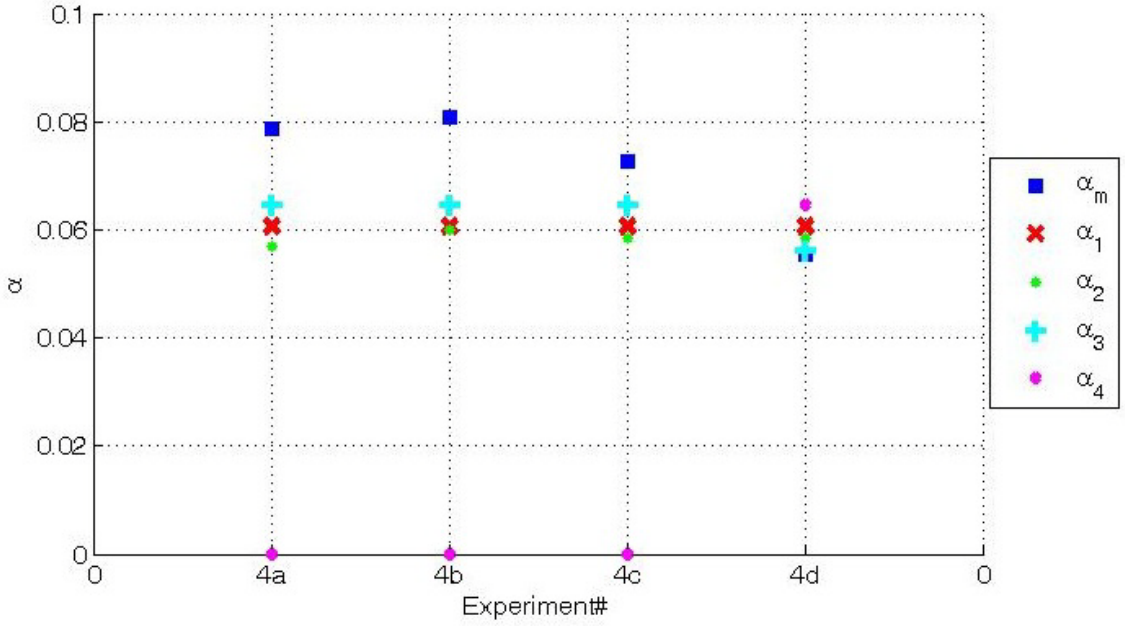

Figure 63: Multi mode experiments: α_m vs. α_i.

Details of the experimental parameters are specified in Table 5**.** Here α_m is the multi mode growth rate constant and $\alpha_1, \alpha_2, \alpha_3$ and α_4 are the component saturation growth rate constants. This corresponds to $(\lambda_1, \lambda_2, \lambda_3, \lambda_4)$ = (8, 4, 2, 0), (8, 5, 2, 0), (8, 6, 2, 0) and (8, 6, 3, 2) cm, and $(\theta_1, \theta_2, \theta_3)$ = (45°, 90°, 135°) respectively.

3.8. Bubble and spike velocity calculations

This section details the experiments conducted to measure the bubble and spike velocities of RTI with single-mode initial perturbations. Measurement of bubble and spike velocity data in different regimes of the evolution of RTI is necessary in order to establish a robust system to perform and analyze the first well-controlled binary and

multi-mode experiments, which is the main objective of this thesis. As such, velocity measurements for single mode experiments provide us valuable data for establishing accuracy as well as for understanding the physics of RTI. Validating these experiments provides a foothold for future experiments with binary and multi-mode initial conditions, experimental bubble and spike velocity data for which is scarcely available in the literature. Therefore, the set of experiments specified in Table 6 were performed with the same operating parameters as specified in Table 1 using High-speed imaging technique as described in Appendix §D.1. Details of the high-speed camera are given in section §2.0

The following observations were made from the analysis: The images were very sensitive to backlight. At high frequencies of operation such as the present frequency of 1000Hz, backlight variation of about 280% was observed for the darkest sections of the channel (corresponding to unmixed cold water) and a variation of about 220% for the brightest sections of the channel (corresponding to unmixed hot water). For lower operating frequencies of imaging such as the frequency of regular ensemble averaging technique, this variation in backlight was not observed. This might be because the arrays of tube lights that comprise the backlight fluctuate at about 100 Hz as measured from the high-speed image data. This variation in backlight presented difficulties in image analysis due to which velocity data could not be accurately measured. Details of the image analysis code with flow chart are described in section §E.2. Defining an exact location for the tip of the bubble or spike was not possible due to varying pixel intensities. Therefore, videos of bubble and spike motion were captured at high

frequency to observe the details of the RTI phenomenon. It is suggested to use a LED as a source of backlight in the future such that this difficulty can be overcome. Use of a Telescopic lens to reduce parallax error while retaining the resolution of high-speed images was also proposed. Comparison of bubble and spike velocity data with analytical theories and numerical simulations will establish the accuracy of this procedure for multi-mode experiments to be performed at a later stage.

4. DISCUSSION

4.1. Summary

From the above section §3, the following observations could be made:

- Motivated by the ICF and many other applications, many experiments were performed using the water channel facility towards the objectives specified in section §1.4.
- A list of experiments with varying initial conditions was chosen such that the effects of initial conditions can be measured and analyzed.
- Calculations were performed to obtain the variation of the time-means of displacements, velocities and energy introduced by the flapper into the top and bottom streams of the channel. The maximum, minimum, mean variables were plotted for each binary and multi-mode experiment to understand the effect of flapper motion in generation of RTI.
- Visualization of the system was performed using dye and milk visualization techniques. Velocities of the top and bottom streams were measured using the dye-blob technique to accurate values. Based on the dye visualization from the flapper tip, a measure of the amount of free-stream turbulence in the channel flow can be obtained.
- Density of the working fluid was measured upto 6 digit accuracy using a densitometer. Measured density from densitometer established the effect of Sodium Thiosulfate and Nigrosene on the density of water to be insignificant. Variation of measured density of supply water with temperature was

compared with NIST database values and Kulkula's correlation. It was observed that there was a deviation of about 0.15% between measured density and the database values. Kulkula's correlation matches very closely with the NIST database values. Atwood number calculated from measured density values and Kulkula's correlation were compared and a deviation of about 30% was found for a ΔT of 5°C. Therefore, new correlations were formulated for density and Atwood number variations with temperature.

- The Servo system setup was validated using a traditional plotter mechanism at different stages in the mechanism for generating the input initial conditions. It established high levels of accuracies of motor axis motion, flapper tip motion in air and flapper tip motion under water. The system's operating software code was also optimized for smoother and accurate generation of initial conditions. Thus, the system was validated as highly-accurate and repeatable, and capable of performing multi-mode experiments.
- Single mode experiments were performed to validate the setup according to previous results. The symmetry of structures observed in the image data taken from these experiments was used for elimination of shear between the top and bottom streams of the channel. Total Mixing width and saturation growth rate constant α values were calculated for each of the single-mode experiments. Measured α values for these experiments is observed to be in the range of 0.0494-0.06. This data should serve as a basis of comparison for binary-mode and multi-mode experiments.

- Binary mode experiments were performed with highly controlled initial conditions with great accuracy. Two sets of experiments were chosen to allow the study of two fundamental parameters, namely, phase-difference θ and wavelength, λ.
- The first set of experiments was performed with constant wavelength component modes of 4cm and 2cm wavelength, respectively and a varying phase difference. From these experiments, the structures of binary modes coming off the splitter plate were photographed. A theory on the angle of lean is sought such that the effect of phase-difference in binary mode RTI could be quantized as equivalent to a specific shear in a KHI experiment. Mixing width analysis reveals that binary modes grow faster in the linear regime of growth compared to component single-mode mixing widths, and mode coupling can be witnessed in the non-linear regime. This mode coupling mitigates effective growth rate by a maximum for θ=90° or θ=270° and enhances the growth rate for θ=45° or θ=135°. Also, α values were found to be generally higher than the component αs, except for θ=90° and θ=225°.
- The second set of experiments was performed to observe the effect of wavelength, λ on the growth rates. A similar imaging to visualize the structures was performed and it was observed that the structures have a similar shape for all the cases. One peculiar case is that of λ_1=λ_2=4cm, which displayed very symmetric structures with respect to the horizontal axis. A first subset of experiments was performed to observe the effect of λ_1. Initial

growth rates of binary modes were found to be higher than the component modes but mode coupling affects the saturation growth rate. Highest saturation growth rate was found to be for λ_1=6cm. Calculated α_{12} values were found to be higher than both component modes but they decrease with increasing α_1. The second subset of experiments was performed to observe the effect of the magnitude of the amplitude. The structures visualized for this subset were very similar to each other. Mixing widths grew proportional to $|\lambda_i|$ initially but reached similar values in the non-linear regime. In the saturation regime, though, mixing width is higher for higher $|\lambda_i|$. The third subset of experiments was performed to observe the effect of λ_2 on the binary mode growth characteristics. As expected, mixing widths are higher for higher λ_2 in the linear regime, whereas λ_2 = 3cm was found to have the highest width in the non-linear regime. An explanation is sought for the observed behavior.

- For the first time, highly-controlled multi-mode experiments were performed using the novel servo motor mechanism. Visualization of the structures showed a large number of small scale secondary structures arising from primary structures due to the large wavelengths. This could be attributed to the higher RMS errors in the motor signal compared to the earlier binary mode experiments. Also, because of the difficulties in backlight and dye visualization, the structures could not be clearly discerned. Mixing widths of tri-modal experiments show that the mixing width increases with λ_2 in all regimes, with λ_1, λ_3, θ_1 and θ_3 kept constant.

- High-speed imaging was performed to measure the bubble and spike tip velocities as a function of time. Many difficulties were faced during this analysis, especially due to the backlight fluctuation. Therefore, videos of the flow were made to understand the flow behavior. It was deemed that future endeavors on high-speed imaging must be equipped with better backlight and higher temporal and spatial resolution.
- The physics behind RTI is yet to be understood clearly quantified by the scientific community. Because RTI is such a complex phenomenon involving the physics of buoyancy, viscosity, vorticity and turbulence, characterized by a range of time and length scales, a generalized theory of the mechanism underlying RTI can only be constructed from a detailed analysis of the comprising phenomena. Therefore, parametric studies must be performed in order to study the effect of non-dimensionalized parameters like Atwood number, Froude number, Schmidt number and Grashof number. Also, other parameters of interest like initial conditions and relative acceleration between the heavier and lighter fluids must be varied and their effects studied. The present state of the art in RTI is incapable of completely predicting the mixing behavior and control the resulting turbulence. Therefore many further experiments must be performed to provide further insights into this fascinating physical phenomenon.

4.2. Sources of error

This section identifies the possible sources of error in the experiments performed such that an idea of the accuracy of measured experimental parameters can be established. The following are the possible sources of error:

- Non-uniform backlighting: This is the most significant source of error. Imaging of the test section with non-uniform background lighting produces uneven pixel intensities which result in inaccurate measurement of the ensemble averaged mixing characteristics. Thus, the background has to be perfectly uniform for getting quality data from ensemble averaging analysis. In fact, symmetry of the contours, mixing widths and growth rates are all affected by this parameter.
- Free stream turbulence: Results in secondary structures to be created earlier resulting higher mixing. Caused due to insufficient length of the channel, improper wire meshes etc.
- Thick splitter plate: Introduces a wake into the system which interacts with the RTI interface and creates higher mixing. This could also be a reason for quicker molecular diffusion of the structures into the ambient. Small scale structures enhance viscous dissipation thereby resulting in higher calculated mixing characteristics. An optimized thickness for the splitter plate must be chosen based on strength considerations and minimization of wake effects.
- Parallax error: Difficulties in structure visualization is caused because of parallax error, which results in smearing of the flow structures, thereby making it difficult for any dependent calculations. This is especially true in the case of

high-speed imaging methodology for measuring bubble and spike angles and velocities.

- Servo mechanism errors: Although small, servo mechanism introduces error into the initial conditions such that the initial conditions are not quantified accurately. This can be minimized by tuning the system for optimized software and hardware performance.
- Error in Atwood number measurement: Any uncertainties in measuring the temperature of both fluid streams results in less accurate density calculation, which in turn affects the Atwood numbers. It is to be noted that the value of At is used for calculating α using the Moving window method. Therefore, α is sensitive to temperature measurements.

4.3. Comparison with other research from literature

- Waddell, Niederhaus and Jacobs (2001) have measured the amplitude of bubbles and spikes for low Atwood number RTI using their experimental setup which generated single mode initial conditions by oscillating the test section and generating standing waves. Their data showed bubble and spike amplitudes in very good agreement with the LST. Therefore, bubble and spike velocities measured from the present high-speed imaging technique should be compared with their work.
- Rosenblatt's group (Huang *et al.* 2007) has performed RTI experiments for magnetically levitated fluids with specified single mode initial conditions varying

from 0-3 mm and have reported α values within a range of 0.06 to 0.007. These values are in good agreement with measured αs from this campaign.

- An analytical theory by Dimonte (2004) was modified terminal velocity formulation for bubbles to incorporate Froude number. They have proposed that the evolution of a multi-mode wave packet proceeds by either Non-linear mode coupling or exponential amplification and saturation of ambient modes. Therefore, they have suggested that the saturation growth rate constant α is dependent upon initial conditions. It was observed from the current experiments that in the linear regime, growth rates depend directly upon the component modes, while in the non-linear regime, mode-coupling seems to be the driving mechanism for mixing. Thus, these observations are in agreement with Dimonte's work, and measured α values are one of the first available data on multi-modal experiments.

4.4. Future work

Based on the above discussion of results, comparison of the results with literature and the sources of error in the current experiments, this present section identifies the path forward in RTI research:

- Improve upon the system configuration: More improvements can be acted upon the water channel's current setup such as improved backlighting, reduced free stream turbulence, thinner splitter plate and increased capacity of water tanks etc. for larger data collection times.

- Lagrangian Approach: To study the binary and multi-mode structures in detail, a Lagrangian approach of imaging is proposed wherein images of the primary and secondary flow structures could be photographed with the camera sliding in the streamwise direction at the same free stream velocity of the flow. This would enable capturing the temporal evolution of the structures.
- Improvised High-speed imaging: Based on the above two points, high-speed imaging as described in this thesis in section §3.8 can be performed with better accuracy to measure the bubble and spike angles and velocities. This should enable a clear understanding of the physics of RTI with multi-modal initial conditions and will serve as a benchmark for all further analyses.
- PLIF and PIV: One suitable alternative to alienating the effects of non-uniform backlight is the usage of PLIF for flow visualization purposes. This method will generate reliable scientific data for binary mode imaging and give a clear understanding of the leaning phenomenon. Finally, late time regimes of the RTI can be studied using PIV techniques. Measured fluctuating velocity components would give an estimate of various stress tensors in the late time regions and help validate turbulent modeling methodologies. Such an exercise was performed by Peart (2008) to measure the terms for the BHR model of turbulence.

REFERENCES

ABARZHI, S. I., NISHIHARA, K. & GLIMM, J. 2003 Rayleigh-Taylor and Richtmyer-Meshkov instabilities for fluids with a finite density ratio. *Physics Letters A* **317**, 470-476.

ABARZHI, S. I. 2010 Review of theoretical modelling approaches of Rayleigh-Taylor instabilities and turbulent mixing. *Philosophical Transactions of the Royal Society A: Mathematical, Physical and Engineering Sciences* **368**, 1809-1828.

ALON, U., HECHT, J., OFER, D. & SHVARTS, D. 1995 Power laws and similarity of Rayleigh-Taylor and Richtmyer-Meshkov mixing fronts at all density ratios. *Physical Review Letters* **74**, 534-537.

ANDREWS, M. J. & DALZIEL, S. B. 2010 Small Atwood number Rayleigh–Taylor experiments. *Philosophical Transactions of the Royal Society A: Mathematical, Physical and Engineering Sciences* **368**, 1663-1679.

BANERJEE, A. & ANDREWS, M. J. 2006 Statistically steady measurements of Rayleigh-Taylor mixing in a gas channel. *Physics of Fluids* **18**, 035107-035113.

CARLÈS, P., HUANG, Z., CARBONE, G. & ROSENBLATT, C. 2006 Rayleigh-Taylor instability for immiscible fluids of arbitrary viscosities: A magnetic levitation investigation and theoretical model. *Physical Review Letters* **96**, 1-4.

CHANDRASEKHAR, S. 1961 *Hydrodynamic and Magnetic Stability*. Clarendon.

DALY, B. J. 1967 Numerical Study of Two Fluid Rayleigh-Taylor Instability. *Physics of Fluids* **10**, 297-307.

DAVIS R. & WALTERS, F. M. 1922 Sensitometry of photographic emulsions and a survey of the characteristics of plates of American manufacture. *Bur. Stand. USA Sci. Papers* **18**, 1-120.

DIMONTE, G. 2004 Dependence of turbulent Rayleigh-Taylor instability on initial perturbations. *Physical Review E* **69**, 1-14.

DIMONTE, G., MORRISON, J., HULSEY, S., NELSON, D., WEAVER, S., SUSOEFF, A., HAWKE, R., SCHNEIDER, M., BATTEAUX, J., LEE, D. & TICEHURST, J. 1996 A linear electric motor to study turbulent hydrodynamics. *Review of Scientific Instruments* **67**, 302-306.

DIMONTE, G. & SCHNEIDER, M. 2000 Density ratio dependence of Rayleigh-Taylor mixing for sustained and impulsive acceleration histories. *Physics of Fluids* **12**, 304-321.

DORON, Y. 2009 Effect of single mode initial conditions on Rayleigh-Taylor turbulent mixing. MS Thesis, Texas A&M University, College Station.

FREED, N., OFER, D., SHVARTS, D. & ORSZAG, S. A. 1991 Two-phase flow analysis of self-similar turbulent mixing by Rayleigh--Taylor instability. *Physics of Fluids A: Fluid Dynamics* **3**, 912-918.

GONCHAROV, V. N. 2002 Analytical model of nonlinear, single-mode, classical Rayleigh-Taylor instability at arbitrary Atwood numbers. *Physical Review Letters* **88**, 1-4.

HUANG, Z., DE LUCA, A., ATHERTON, T. J., BIRD, M., ROSENBLATT, C. & CARLÈS, P. 2007 Rayleigh-Taylor instability experiments with precise and arbitrary control of the initial interface shape. *Physical Review Letters* **99**, 1-4.

KRAFT, W. 2004 Experimental investigation of a stratified buoyant wake. MS Thesis, Texas A&M University, College Station.

KULKULA, D. J. 1981 Thermodynamic and transport properties of pure and saline water. MS Thesis, State University of New York Buffalo.

LAYZER, D. 1955a On the instability of superposed fluids in a graviational field. *Astrophysics Journal* **1222** 1-12.

LAYZER, D. 1955b Reference to Fermi's paper is found here. *Astrophysics Journal* **122**.

LEICHT, K. A. 1997 Effect of initial conditions on Rayleigh-Taylor mixing development. MS Thesis, Texas A&M University, College Station.

LEWIS, D. J. 1950 The instability of liquid surfaces when accelerated in a direction perpendicular to their planes-II. In *Proceedings of the Annual Meeting of Proceedings of the Royal Society of London. Series A, Mathematical and Physical Sciences.*

LINDL, J. D. & MEAD, W. C. 1975 Two-Dimensional simulation of fluid instability in laser-fusion Pellets. *Physical Review Letters* **34**, 1273-1276.

LINDL, J. D. 1999 Inertial confinement fusion: The quest for ignition and energy gain using indirect drive. *Nuclear Fusion* **39**, 825-829.

MIKAELIAN, K. O. 2003 Explicit expressions for the evolution of single-mode Rayleigh-Taylor and Richtmyer-Meshkov instabilities at arbitrary Atwood numbers. *Physical Review E* **67**, 1-7.

MUESCHKE, N. J. 2004 An investigation of the influence of initial conditions on Rayleigh-Taylor mixing. MS Thesis, Texas A&M University, College Station.

OLSON, D. H. & JACOBS, J. W. 2009 Experimental study of Rayleigh-Taylor instability with a complex initial perturbation. *Physics of Fluids* **21**, 034103-034113.

ORON, D., ARAZI, L., KARTOON, D., RIKANATI, A., ALON, U. & SHVARTS, D. 2001 Dimensionality dependence of the Rayleigh--Taylor and Richtmyer--Meshkov instability late-time scaling laws. *Physics of Plasmas* **8**, 2883-2889.

PEART, F. M. 2008 Effect of initial conditions on the development of Rayleigh-Taylor instabilities. MS Thesis, Texas A&M University, College Station.

RAMAPRABHU, P., DIMONTE, G. & ANDREWS, M. J. 2005 A numerical study of the influence of initial perturbations on the turbulent Rayleigh-Taylor instability. *Journal of Fluid Mechanics* **536**, 285-319.

RAYLEIGH 1883 Investigation of the equilibrium of an incompressible heavy fluid of variable density. *Proc. Lond. Math Soc* **170-177.**

ROBEY, H. R. 2008 Results and analysis of indirectly driven precision double shell implosions on the Omega laser facility. In *Proceedings of the 11th Annual Meeting of IWPCTM,* Santa Fe.

SCHMITT, A. J., VELIKOVICH, A. L., GARDNER, J. H., PAWLEY, C., OBENSCHAIN, S. P., AGLITSKIY, Y. & CHAN, Y. 2001 Growth of pellet imperfections and laser imprint in direct drive inertial confinement fusion targets. *Physics of Plasmas* **8**, 2287-2295.

SNIDER, D. M. & ANDREWS, M. J. 1994 Rayleigh-Taylor and shear driven mixing with an unstable thermal stratification. *Physics of Fluids* **6**, 3324-3334.

SOHN, S.-I. 2003 Simple potential-flow model of Rayleigh-Taylor and Richtmyer-Meshkov instabilities for all density ratios. *Physical Review E* **67**, 1-5.

SOHN, S.-I. 2009 Effects of surface tension and viscosity on the growth rates of Rayleigh-Taylor and Richtmyer-Meshkov instabilities. *Physical Review E* **80**, 1-4.

TAYLOR, G. 1950 The instability of liquid surfaces when accelerated in a direction perpendicular to their planes-I. In *Proceedings of the Annual Meeting of Proceedings of the Royal Society of London. Series A, Mathematical and Physical Sciences.*

WADDELL, J. T., NIEDERHAUS, C. E. & JACOBS, J. W. 2001 Experimental study of Rayleigh-Taylor instability: Low Atwood number liquid systems with single-mode initial perturbations. *Physics of Fluids* **13**, 1263-1273.

YOUNGS, D. L. 1984 Numerical simulation of turbulent mixing by Rayleigh-Taylor instability. *Physica D: Nonlinear Phenomena* **12**, 32-44.

APPENDIX A. WATER CHANNEL

A.1 Water channel: Operating procedures

1. Turn on water supplies into the hot and cold water supply tanks. Ensure that remnant dye water from previous experiments is purged. This is done by pumping the remnant water to the plastic drain tanks.
    a. Cold water is supplied from the hose that connects to the tap near the men's restroom.
    b. Hot water is supplied through the white-colored PVC tubing that enters at the corner of the water fountain. The blue valve controls supply.
2. Plug in sump pumps in both supply tanks and turn them on to mix the water uniformly. This is essential for reliable mixing of dye.
3. Add 100 ml of Sodium Thiosulfate (Na_2S_23) 2.0N to the water in either tanks. It was observed during the course of performing the experiments that Chlorine content in the supply water varies with the day. It was also observed that any surplus Chlorine content in the water turns the Nigrosene dye to a dirty-brown color, which is not desired for imaging purposes. Therefore, addition of Sodium Thiosulfate was proposed to neutralize the Chlorine content in water.
4. After Sodium Thiosulfate mixes with the water thoroughly, measure Nigrosene dye using the Digital scales and mix with the Cold water in the tank.
5. Make sure the outlet plenum valves are closed and start filling the water channel using the pumps or the water hose that supplies to the Cold water channel. Remove any unwanted particles or material sticking to the channel surfaces.

6. Remove trapped air bubbles beneath the splitter plate using the water hose to guide the flow to the holes. Removing the used tape that blocks the holes in the splitter plate will release any bubbles to the outside. After bubbles are removed, close the holes using new tape.
7. Check both tanks for desired water temperatures, using Thermocouples. Depending on the type of thermocouples, hold the reader for sufficient time and read a steady temperature. Release hot or cold water until desired temperatures are attained.
8. Set the Servo system to sit on the top plane surfaces of the water channel. Connect all servo motor cords properly. The present system is idiot-proofed. Tune the system using Galil tools® Software, as described in the Operating procedures for servo motor (APPENDIX §B.2), then set the flapper to the desired position. The standard horizontal position for flapper tip is marked as a red line on the channel front side.
9. Set the camera in the correct position. Ensure the horizontal level of camera mount using bubble levels. Check that the axis of the camera stays exactly perpendicular to the flow-direction of channel and the camera is in focus. Check the tripod is sturdy and memory card properly inserted with sufficient free space. Connect the remote control for self-timer. Adjust all other settings as required, like resolution, image type, timing settings, exposure and focus. Other details of the SLR operation can be found in the User manual.
10. Turn on the system backlight.

11. Cover the channel top with Plexi-glass and place weights on them.
12. Observe the channel from the front with the backlights turned on and check for the presence of water droplets on the channel walls. (Front and back, especially between the diffusing acrylic sheet and the channel surface).
13. Turn off sump pumps before beginning the experiments, and turn on the motors.
14. Open all valves at the outlet plenum location and ensure that the water level in the channel- remains constant. Valves that need partial opening are marked. Flow-rates of the top and bottom sections of the channel have to be adjusted beforehand using rotameter valves such that the required shear conditions are created in the channel. This can be done with dye experiments and Single-mode initial conditions on the flapper. The spikes and bubbles generated for a single-mode perturbation at any Atwood number are always aligned with vertical.
15. Start the servo motor for flapping, and take images of the flow.
16. Once the experiment is completed, turn off all motors and drain the water in the channel. Also unlock the flapper so that it does not damage due to the pressure.

A.2 Water channel: Safety precautions

1. Do not leave power cords lying on the floor. The channel leaks and that might be a hazard.
2. Caution has to be exercised when tuning the servo motor. Use of Auto-tune is preferred to manual tune where change of gains can cause the flapper to move at high speeds and cause high vibrations that cause damage to the channel.

3. Control speeds of the flow such that the water does not flood the channel. Close and open valves when necessary.
4. Reduce clutter at the workspace for ease of operation.

APPENDIX B. SERVO MOTOR

B.1 Servo motor: Operating procedures

Use of a servo motor for creating initial conditions at the interface of fluid streams is described here. Description of the motor system and its features are specified in section §2.1. It is necessary to read the User Manual/ Operating procedures if it is the first time of operation.

1. Take the servo motor and mount it firmly on the Plexi-glass base fitted to top of the water channel. Use lock-nuts to restrict the motion of all links to a plane. Fasten the bolts tightly enough because a sturdy mounting of the motor is required for reducing vibrations that are propagated into the flow.
2. Move the links by hand and check that the connecting joints are well oiled. If not, grease them.
3. Place the Power and controller units on the Plexi-glass base. Ensure all surfaces are dry.
4. Image of the servo system is shown in Figure 64 with the labeled components and connections. Insert the connectors in the appropriate slots.

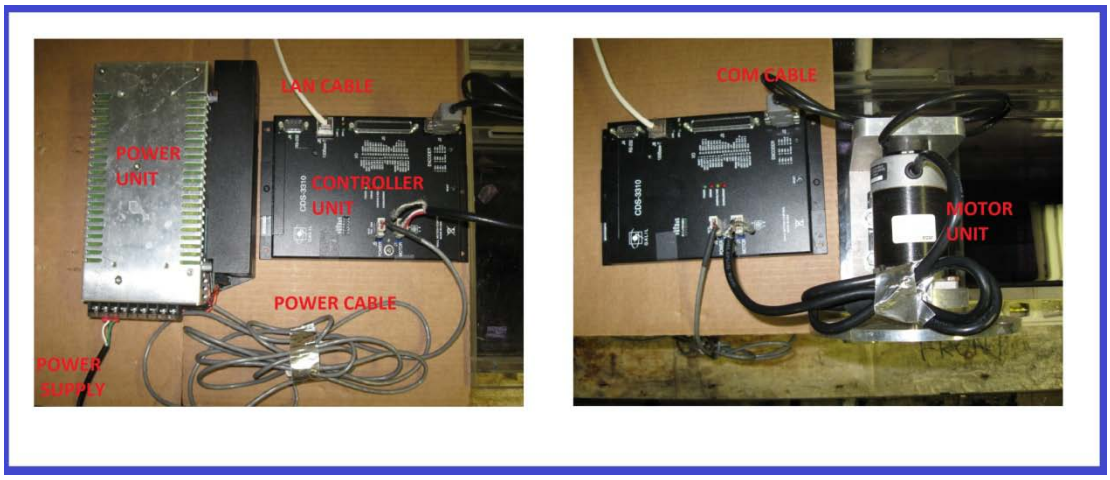

Figure 64: (a) Power and controller unit connections.

(b) Servo and Controller Unit connections.

5. Polish the surface of the flapper and splitter plate if required. Make sure there is no mixing of top and bottom water streams because of leaks through any holes.
6. After checking the flapper is free to rotate in its axis, turn on the power supply.
7. These IP address settings need to be assigned to the servo controller unit such that the computer can directly connect and control it through a Local Area Network (LAN) collection:
    a. IP Address: 165.091.148.10
    b. Subnet mask: 255.255.25.0
    c. Default gateway: 165.091.148.1
8. Turn on the computer and check that the LAN connection to the servo controller is established. This can be seen in the bottom right hand corner of the screen for a Windows based machine.

9. Open the Galil Tools® software interface and connect to the IP address using the + shaped symbol shown at the top. As the servo connects, it is locked in its axis and cannot move freely.
10. Use the auto-tune option of the software to set the gains K_D, K_P and K_I of the motor. A way to test the smoothness of operation is through holding by hand, and another is by hearing the sound. As was observed during validation of the servo for our purposes, in section §3.4, the smoothness of flapper motion and frequency response are highly dependent on the said gains.
11. Run the code. Read operating manuals for further details about the software.
12. A sample code and sample feedback of a typical multi-mode experiment with initial waveform,

$$y = 4 \times sin(\frac{2\pi t}{1.404}) + 3 \times sin(\frac{2\pi t}{1.053} + 45^o) + 18 \times sin(\frac{2\pi t}{0.3509} + 90^o)$$

(y in mm), is shown here in Figure 65:

```
#INITPA
AB1
SPX=12000 'S
ACX=12000 'A
DCX=12000 'D
i=0.2; 'INCREMENT STEP
v=0; 'START RUNNING
PTX=1; 'ENABLE POSITION TRACKING
A = 76.39;‘8cm wavelength
A1 = 1404;
B = 57.23;‘6cm wavelength
B1 = 1053;
C = 19.05;‘2cm wavelength
C1 = 350.9;
T = 360;
```

```
#LOOP
IT 0.2 ‘Smoothing function parameter
                    'θ = t/TP×360
PAX                                                                    =
A*@SIN[TIME*T/A1]+B*@SIN[TIME*T/B1+45]+C*@SIN[TIME*T/C1+90;
                    ‘Position = Amplitude* Sin(θ)
                    'Amplitude is calculated from the EES code
WT2;
                    ‘ Put a brief wait so the code does not update too fast
                    ' This wait is the ultimate wait period of the loop
JP#LOOP
EN
```

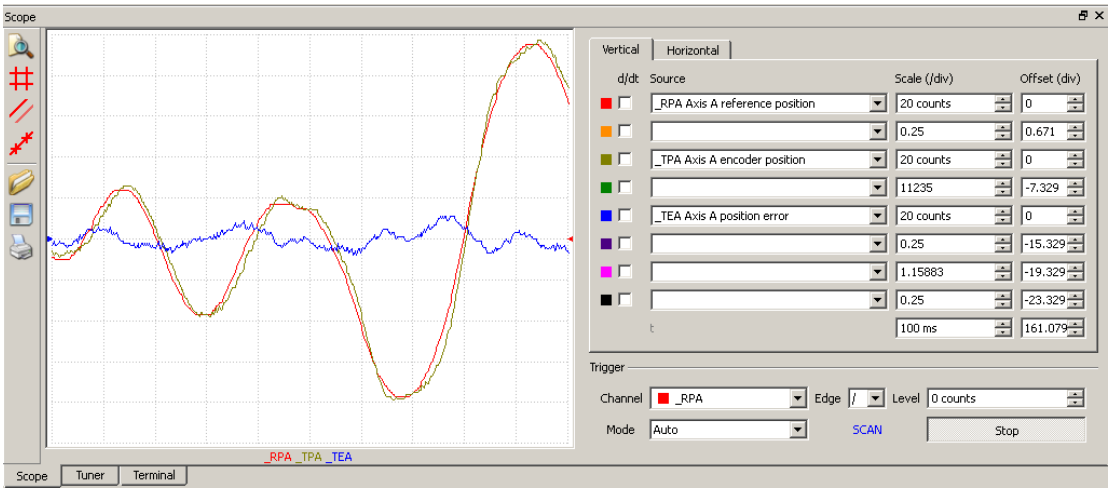

Figure 65: Sample signals of servo motor operation using above code

13. Note the delay, the amplitude and the frequency distribution of the signals.

B.2 Servo motor: Safety precautions

1. Always keep the servo system in a dry environment. This might be a hazard.
2. Caution has to be exercised when tuning the servo motor. Use of Auto-tune is preferred to manual tune where change of gains can cause the flapper to move at high speeds and cause heavy vibrations that can cause damage to the channel.

3. The rotating disk should be tightly mounted on the motor axis. If the disk slips during rotation (tuning or operation) that might cause injury.

APPENDIX C. DENSITOMETER

Details of the densitometer and operating procedure are explained below.

C.1 Densitometer: Instrument details

It is a digital Densitometer type DDM 2911 make by Rudolph Research Analytical Inc. used for measuring density, specific gravity and Concentration of liquids. It works on the principle of resonance of the internal U-tube with and without the liquid sample, the frequency of which gives a measure of the mass contained in the given volume of the tube and a specified temperature. A tube of dry desiccant, a glass tumbler, nozzles, few syringes of 3ml capacity and documentation are provided as accessories. Further details about the setup can be found in the User Manual.

C.2 Densitometer: Operating procedures

1. Connect all cables and turn on the densitometer.
2. Check that the thin transparent rubber tube is dry and connects the slots on the side and the back of the densitometer. Any liquid droplets inside the tube can vary the moisture of the measured liquid and therefore affect density.
3. Check that the desiccant is dry by its color. Desiccant is white when dry and blue when moist. Remove moisture by heating desiccant removed from the tube carefully in a microwave. Caution must be exercised that the tube is not heated or it will melt.
4. Select a factory method for measuring for measuring liquid density. For density of water, Density NC method is recommended by the manufacturer. Customize if required.

5. Set the appropriate room temperature, liquid temperature, measurement mode (single or batch), stability criterion (determines accuracy of the measurement) and duration of measurement.
6. Calibrate the instrument. Use a pure sample of water for density measurement with factory loaded settings and verify with provided NIST data. Measurements are to be taken only when the measurements are accurate upto 1%.
7. See in the video view display if the U-tube is dry and clean. Otherwise, rinse with acetone and turn the air-pump on until the tube dries up.
8. Take a clean syringe and fill it with sample liquid. There must not be any bubbles in the sample. Remove rubber tube from the right hand side slot and inject sample fluid from syringe into it.
9. Start the measurement and save data.

APPENDIX D. HIGH SPEED CAMERA

Note the connections of cables and the positioning of the camera as per the specifications of the User Manual. Listed below are the steps in setting up the high-speed camera for imaging purposes:

1) Place the tripod at a suitable location and adjust for a horizontal setting with least parallax error, by adjusting the bubble levels.
2) Connect power cords of the camera properly and connect the camera to the computer.
3) Turn on camera. Check for sufficient space on the computer hard drive. It takes about 2-3GB data for each experiment.
4) Calculate the duration of flow for recording based on the free-stream velocity of the flow and the frame rate of the camera. As the size of the RAM is limited, the number of images is inversely proportional to the resolution of the camera. So choose a specific resolution at a specific frame rate.
5) Set the water channel for operation. Check the operating procedures (Appendix §A.1) for details.
6) Set the Servo motor for operation. Check the operating procedures (Appendix §B.1) for details.
7) Take images of the background at the same frame rate. This is necessary for confirming the proper positioning of the camera as well as any adjustments to exposure etc. Exposure settings of the lens have to be set constant for all

imaging. The basic settings for exposure and trigger control can be through the software interface.

8) Save the images to a .cine file. This file can be edited later to generate movie clips or images for analysis. Further details of the camera software operation can be found in the user manual.
9) Start the servo motor and run the experiment. After adjusting for shear in the flow and confirming the steadiness of the flow, start taking images of it.
10) Save data immediately. As saving the data to the computer takes about 3-4 minutes, change the settings of the servo motor for the next experiment.

APPENDIX E. IMAGE ANALYSIS

This appendix details the procedures for image analysis of the obtained water channel experimental data. Two different types of analysis was performed; Ensemble averaging and velocity analysis.

E.1 Ensemble averaging image analysis

The MATLAB code that was used for Image analysis has been modified over time by researchers previously working on this project. The present code was last modified by Dr. Duggleby in May, 2009 for parallel processing, uncertainty analysis and corrections in background analysis. The significant steps involved in analysis are depicted in the flowchart shown below in Figure 66.

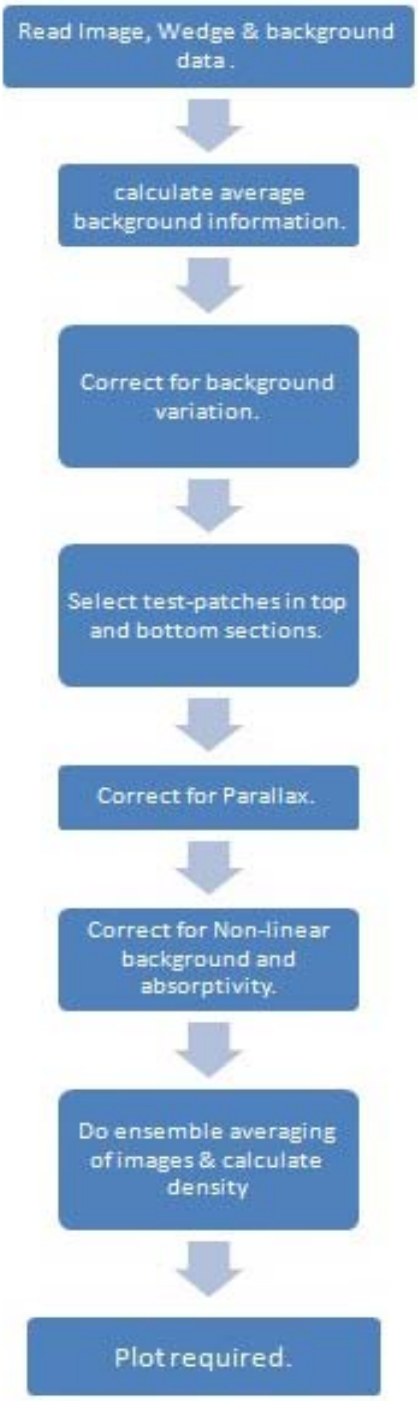

Figure 66: Flow chart of the ensemble averaging analysis process.

A few notes about the code:

1) Images can be saved in .jpg or .raw format. Although the code can be modified to analyze for either format, RAW format is preferred because more data is saved in this format, where JPG uses an algorithm to compress the files, and therefore, loss of data is observed.
2) About a minimum of 30 background images are required for accurately calculating background data. As it was observed that the analysis is very sensitive to background intensity, it must be carefully specified in the code and subtracted.
3) The test-patch sections in the top and bottom sections of the channel must be carefully selected (usually at 3 inches above and below the splitter plate after the flapper) and set to 1 and 0 respectively. The larger the patch, the better the averaging, but the patches must strictly correspond to the darkest and lightest sections of the channel.
4) Sufficient number of images must be taken for ensemble averaging. A Nikon D90 camera is used for capturing images at a regular rate of 1 frame per second for all the present experiments. About 160 images were taken on average for each experimental case.
5) Wedge calibration images are taken for each set of experiments. The code requires the locations and the amount of dye dissolved into the cold water for accurate absorptivity/intensity calculation.

6) The number of background, mix and wedge images must all be divisible by the number of processors used for parallel processing. It is advisable to use a single processor during debugging.
7) Operating parameters of the flow like densities, temperatures, refractive index of glass, free-stream velocity etc. must be provided to the code for calculations and plotting.
8) Other details of the code are described in the comments within the code.

E.2 Velocity calculation analysis

The second type of analysis is the velocity analysis of the high-speed images taken using the high-speed camera. The images are analyzed for spike and bubble tip locations for computing velocities. Listed below are the steps involved in the procedure, which was implemented using MATLAB:

1) Select the range of images corresponding to a single bubble or spike, as long as it retains its shape. The bubble or spike will pass through the linear, non-linear and saturation regimes in this period of time.
2) As with the Ensemble averaging, it is preferred to use RAW format for the images over JPG format.
3) Given the initial position of a bubble or spike and the frame-rate of imaging, the code interrogates a zone of pixels surrounding the specified tip and finds the relative motion of the tip with each frame. Thus, positions and velocities can be obtained.

4) Selecting the appropriate zone of interrogation involves some understanding of the behavior of the flow for a given experiment, depending on the Atwood number, free-stream velocity and nature of the initial perturbation. Too large a zone results in interference of the surrounding bubbles or spikes, and may result in the wrong tip location. On the other hand, too small a zone might not be able to capture the complete curvature of the mushroom shape that is trademark characteristic of Rayleigh-Taylor Instabilities.
5) Unlike the ensemble averaging method, the background intensity of each image varies significantly because at high-speeds, the camera is able to capture the fluctuating intensity of the backlight. Therefore, images intensities are to be observed for a large number of images corresponding to varying time, and normalized with background intensity to nullify the effects of background variation.
6) The above process has to be performed for bubble and spike tip locations separately.
7) Other parameters required for the code must be provided when required. Further details can be found within the code itself. The flow chart of velocity analysis is shown below in Figure 67:

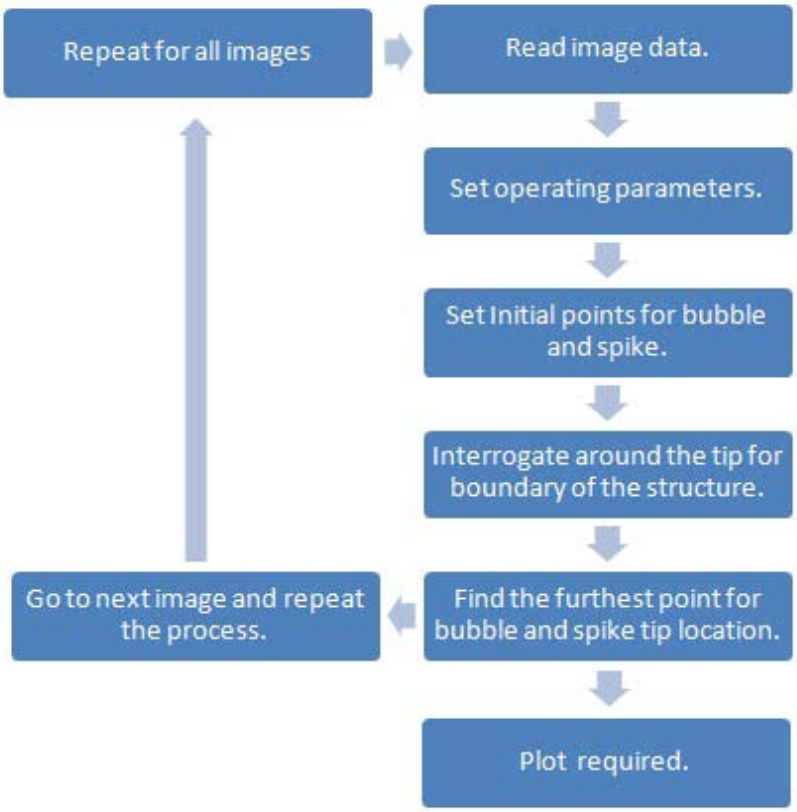

Figure 67: Flow chart of the velocity analysis procedure.

VITA

Name: Sarat chandra Kuchibhatla

Address: Advanced Mixing and Shocktube Laboratory
Texas A&M University
College Station, Texas
77843 -3123

Email Address: sarat2d@tamu.edu

Education: B.Tech., Mechanical Engineering
Indian Institute of Technology Guwahati
Guwahati, India, 2006